INTERFACES IN NANOSCALE PHOTOVOLTAICS

INTERFACES IN NANOSCALE PHOTOVOLTAICS

Grensvlakken in zonnecellen op nanoschaal

ACADEMISCH PROEFSCHRIFT

ter verkrijging van de graad van doctor
aan de Universiteit van Amsterdam
op gezag van de Rector Magnificus
prof. dr. ir. K.I.J. Maex
ten overstaan van een door het college voor promoties
ingestelde commissie,
in het openbaar te verdedigen in de Agnietenkapel
op donderdag 8 december 2016, te 10:00 uur

door

Sebastian Zeki Öner

geboren te Berlijn, Duitsland

Contents

1

Introduction

1.1 Photovoltaics

Photovoltaics provide electricity in a clean, sustainable and often decentralized way by utilizing an abundant and virtually unlimited source of energy: the sun.

177 years after Alexandre Edmond Becquerel created the first photovoltaic device, the technology is on its way to become a major source for primary electrical energy production on earth.[1] In June 2014, solar energy was able to provide 23 GW power, more than half of the electricity demand in Germany at that time, rendering arguments about production capabilities limited to southern countries meaningless.[2] At the end of 2015, after growing for 20% three years in a row, the US solar energy industry alone employed more people than the upstream oil and gas sectors combined (exploration, drilling, extraction), continuing to pave the way for societal and political support from a wide spectrum.[3] Due to the continuing decrease in solar panel costs, financing costs and balance of system costs, by 2017 80% of countries in the world are expected to have reached grid parity according to a recent forecast by the Deutsche Bank.[4]. Currently, solar energy installations account for over 50% of newly installed electricity capacity, therefore outperforming not only gas, and oil but even coal as a primary source of electricity.[5] Alone in 2016, 65 GW solar power are expected to be installed, which would result in a total of roughly 300 GW cumulative installed solar power by the end of the year, an equivalent of 600 typical coal power plants (~ 500 MW). Per year, two billion tons of CO_2 emissions alone will be saved, not to mention the emission of hundreds of thousands of tons of other dangerous toxins.[6]

As a result, in 2050 renewable energies are predicted to provide between 50-90 % of the total energy demand, with wind and solar energy as the major contributors.[7] And these estimates don't even take into consideration the looming invalidation of the free ticket of many technologies to unaccountably

dispose their waste into the environment. Such "externalities" have to be taken into account when calculating the true costs of energy conversion technologies.

To summarize, solar energy not only proved its technical feasibility and its potential for tackling climate change but also its capability as a major economic player by competing against fossil fuel-based technologies. As a result, even traditional economic fossil fuel strongholds such as the World Economic Forum in Davos have put renewable energy and climate change on their agenda.[8]

On the technological side, wafer-based silicon solar cells are the major driver (over 90%) of increased installations. Based on the maturity of the wafer-based silicon technology (over 62 years), the power conversion efficiency has entered a phase of logarithmic increase over time. Currently, the Kaneka IBC HIT cell is the record holder with an efficiency of 26.3%. In other words, 89.5 % of the theoretical maximum efficiency of 29.4% has already been reached.[9, 10] Forecasts predict an ongoing market domination of this technology with improved module efficiencies, decreased production and decreased balance of system (BOS) costs (wiring, converter, mounts,...) as the major drivers for future cost reductions.

In general, attempts to lower the overall solar energy production costs ($/W$) further can broadly be divided into two classes. Either the fabrication costs are reduced while the efficiency is maintained or the efficiency is increased while the production costs are maintained (or slightly increased).

Besides economies of scale, reducing the fabrication costs while maintaining the conversion efficiency can be achieved by optimizing processes, replacing materials or device designs with more energy, work or material efficient options. These approaches are usually pursued in industrial research laboratories or in close collaborations between industrial and academic research centers. In those cases, the requirements and knowledge about the state of the art in the industrial production is clearly communicated to the researchers.[*]

The pursuit for higher power conversion efficiencies, on the other hand, falls directly into the field of expertise of fundamental researchers. More efficient solar cells generally require higher production costs, especially at initial stages before improved processes and economies of scale take place. However, since less solar module area is required to produce the same amount of energy as the existing technology, the effect on the other costs, such as installation, operational and legal (BOS) costs can be profound. Given that the costs of the solar module make up less than ~ 30 % of the total costs, increasing the power conversion efficiency must be regarded as the more powerful and long-term strategy towards overall decreased solar energy production costs.[11, 12]

The tremendous impact of the power conversion efficiency on the overall energy production costs creates a great economic obstacle. Technologies that can

---

[*]Without this close knowledge transfer between the two partners, fundamental researchers are generally badly positioned to tackle those applied and industrially relevant questions. Very often, they lack the knowledge of technical details and requirements about industrial large-scale and high through-put processes. Furthermore, current and forcasted costs of specific process steps are generally undisclosed due to industrial competition.

only provide low conversion efficiencies, even if at a low cost, are unlikely to succeed. Furthermore, looking back at many successful innovative technologies, it becomes apparent that market entry and adaptation are more likely to be successful when new substantial capabilities are being provided. The typewriter has not been replaced by the PC, the propeller by the turbine engine, or the horse carriage by the car because the later was produced cheaper.

Figure 1.1 shows a summary of the increase of certified power conversion efficiencies of different solar cell technologies over time, starting from the year 1975. Many of the more established technologies, such as single crystalline, multicrystalline and amorphous silicon show a clear logarithmic trend of conversion efficiency increases over time. This "learning curve" is very typical for many technologies. Initially, a new technology offers much room for improvements that can be achieved rather easily, while continuous developments narrow the phase space of opportunities progressively. Eventually, only a few increasingly challenging paths are left to explore. To prevent a standstill in performance improvements, new technologies have to be pursued that allow for steeper efficiency increases, because they exhibit relatively more unexplored opportunities. Among the new emerging technologies are those that aim at utilizing electric and optical effects that emerge by nanoscale patterning and fabrication. Among them are quantum dot and nanowire solar cells, the latter being a focus of this work. For nanowire array solar cells, the
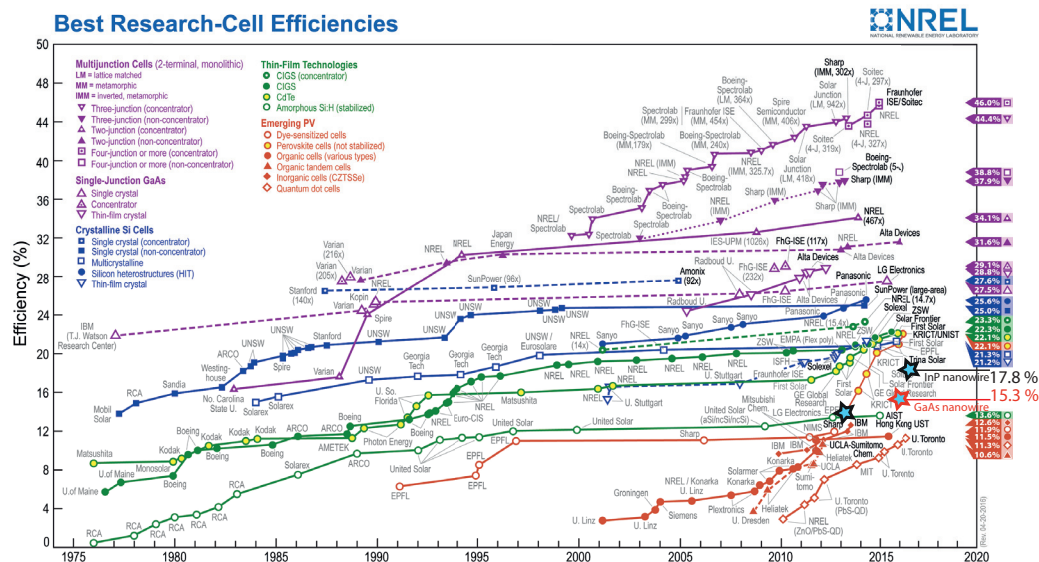
Figure 1.1: Best research-cell efficiencies over time. Nanowire array solar cell efficiencies are shown as blue stars with black (InP) and red (GaAs) outlines.
The original plot is courtesy of the National Renewable Energy Laboratory, Golden, CO.

efficiency records are 17.8 % for InP and 15.3 % for GaAs and are shown in Figure 1.1 as blue stars with black and red outlines, respectively.[13, 14]

It has to be noted, that Fig. 1.1 does not discriminate between technologies that are pursued industrially or purely in research laboratories; the only requirement is the existence of a certified efficiency measurement by one of the leading research laboratories. Many of the new emerging technologies hold great promise to allow an overall cheaper generation of solar power in the future. Due to their novelty, they often lack any proof of industrial applicability, especially in terms of large scale and high throughput fabrication. Additionally, the stable performance in ambient conditions is a major challenge for many of the emerging technologies. However, to realistically evaluate the potential of those technologies one has to see the current developments in a historic context. In 1941, R. S. Ohl reported the first silicon solar cell (a "Light-Sensitive Electrical Device"), which was below 1% and far from any industrial production.[15] "There were a great many enemies to this work with semiconductors; you have no idea how many people opposed that. Vacuum tube people said that there is nothing to it and it is all a lot of tommyrot, and that sort of thing." - Russell Ohl, January 6th 1975. Today, silicon solar cells are being industrially produced with an efficiency of up to 25.6% and are contributing to over 90% of the ever increasing installed solar power. The record efficiencies are approaching 50% for multi-junction concentrator solar cells, a technology that makes use of efficiency gains by concentrating sunlight onto a multi-layered absorber. Each one of those layers converts a certain part of the solar spectrum highly efficiently. Given the vastly increased knowledge and the far larger man-power involved into the topic, also tangential in other research fields, a higher efficiency growth rate over time can be expected. These emerging technologies hold enormous potential to realize industrially produced, high-performance solar cells with power conversion efficiencies far above current values. In fact, they are indispensable to reach the ambitious targets for a clean energy economy in the near future.[16]

1.2 The basics of a solar cell

Figure 1.2 schematically depicts the fundamental mechanisms taking place in a solar cell during the energy conversion process from photons into electrons.

Sunlight, with its broad spectrum (blue, green and red arrowheads), is incident on the solar cell with a solid angle (Ω_{in}) subtended by the sun (1).

For a single band gap semiconductor, high energy photons (blue arrowheads) excite charge carriers (e^-, h^+) over the band gap deep into high energy levels in the conduction and valence band (2a). Once excited, those high energy carriers loose a large part of their energy very rapidly ($\approx$ 100 fs) by phonon scattering until they reach the conduction (E_C) and valence band (E_V) edges. They now have the same energy as carriers that have been excited by photons with an energy just above the band gap (2b). Photons with an energy below the band gap (red), cannot be absorbed and hence are lost altogether (2c). The same holds for photons of higher energy (blue and green) that are reflected from the surface or cannot be absorbed, because the semiconductor is too thin.

Once the electrons and holes are excited to the conduction and valence band, they have to be extracted at the electron and hole contact, respectively. However, on their path they can recombine radiatively from the conduction and valence band edges (3). This radiative recombination leads to light emission with a solid angle Ω_{out} which is larger than or equal to the angle of the incident beam Ω_{in} (1 vs. 3). In most solar cells, a substantial solid angle expansion can be observed. In other words, much more radiative recombination is taking place than is dictated by thermodynamic limits: in the ideal case, the solar cell would only emit light into the angle subtended by the sun ($\Omega_{out} = \Omega_{in} \approx 6.85 * 10^{-5} sr$).

Another important loss mechanism for the charge carriers on their way to the contacts is non-radiative Shockley-Read-Hall (SRH) recombination at bulk, interface and surface defects (4). Continuous work on defect passivation is necessary to reduce those detrimental processes. Due to the large surface-to-volume ratio of nanoscale structures, surface recombination and the mitigation thereof are among the main topics of this thesis. Besides SRH, non-radiative Auger recombination can take place (not shown in Fig 1.2). For this process, excited charge carriers recombine, but instead of emitting a photon they excite charge carriers in the conduction or valence band to higher laying energy levels. From there, the carriers relax again rapidly by phonon scattering, as in (2a).

Carrier selective contacts are another focus of this thesis. An electron selective contact must hinder the passage of holes, otherwise the carrier concentration will be reduced substantially by additional recombination (5).

Eventually, if the charge carriers do not recombine radiatively (3) or non-radiatively in the bulk (4) or at non-selective contacts (5), they can be extracted efficiently (6). Finally, a solar cell delivers voltage and current to an external load (7). For most solar cells, the current is mainly reduced by the processes (2c) and (4), while the voltage is mainly affected by (2c), (3), (4) and (5).

Figure 1.2: The basic solar cell processes. (1) Light with the sun's spectrum (depicted with blue, green and red arrowheads) is incident on the solar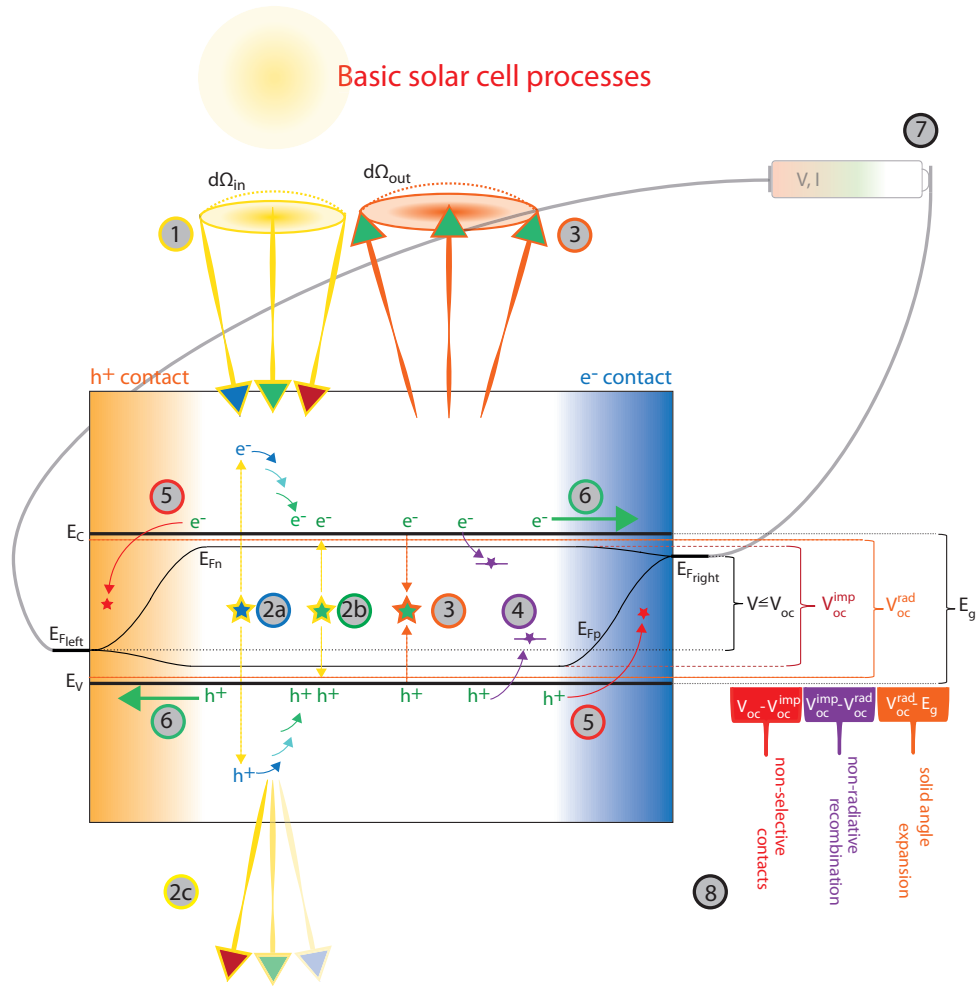 cell with a solid angle ($d\Omega$) subtended by the sun. (2a) Photon absorption and fast thermalization of high energy charge carriers to the conduction (E_C) and valence band (E_V) edges. (2b) Efficient photon absorption and charge carrier excitation directly at the band gap. (2c) Optical losses due to imperfect absorption and reflection. (3) Radiative recombination of charge carriers at the band gap, leading to solid angle expansion due to imperfect optical properties. (4) Non-radiative recombination at defect traps deep inside the band gap. (5) Limited contact selectivity leads to movement of charge carriers into the wrong direction that are eventually lost due to non-radiative (Auger) or additional radiative recombination. (6) Efficient charge carrier extraction. (7) A solar cell delivers voltage and current to an external load. The current is mainly reduced by (2c) and (4), while the voltage is strongly affected by the processes (2c), (3), (4) and (5), as schematically shown on the right side (8).

On the right side of Fig. 1.2 the effect of recombination on the solar cell voltage is depicted (8). The photon excitation of charge carriers over the band gap (2a,b) changes the carrier concentrations vastly compared to thermal equilibrium (in the dark). The additional light-induced carrier concentrations in the conduction and in the valence band give rise to a difference in the free energies, the quasi-Fermi levels, for electrons (E_{Fn}) and holes (E_{Fh}). This quasi-Fermi level splitting is essentially a potential that can be used to perform work in a connected circuit. Consequently, every means to increase the light induced carrier concentration and to prevent recombination will result in a solar cell that delivers a higher voltage.

Different recombination processes take place after the excitation of charge carriers to the band edges ((2c), (3), (4) and (5)). The only recombination that is strictly dictated by thermodynamics is the small amount that is emitted into the solid angle of the sun ($\Omega_{out} = \Omega_{in}$). This solid angle is closely related to the entropy of the light, which according to the second law of thermodynamics can never decrease, only increase or stay constant. If the solid angle stays constant, that is in the absence of other radiative recombination channels, this small amount leads to a potential that is very close to the band gap (E_G). However, in general, enhanced radiative recombination leads to light that is emitted into directions other than the direct incident light ($\Omega_{out} > \Omega_{in}$), which substantially lowers the internal carrier concentration. The effect of those radiative processes is captured in the radiative open-circuit voltage V_{oc}^{rad}. Unless those processes are controlled, e.g. via dielectric thin-layer coatings that limit Ω_{out}, this value sets a practical upper limit; V_{oc}^{rad} is the maximum open-circuit voltage that can be extracted in the absence of non-radiative recombination.

In the presence of non-radiative recombination (4), the voltage is reduced to the implied open-circuit voltage, V_{oc}^{imp}. With an increasing defect density that increases non-radiative channels, the gap between V_{oc}^{imp} and the upper limit, V_{oc}^{rad}, widens. In general, V_{oc}^{imp} refers to the spatially averaged carrier concentration.

Non-radiative (Auger) and radiative recombination close to the contacts (5) are particularly detrimental. If an electron contact is not selective enough, holes enter the region of high intrinsic electron concentration and recombine with electrons. Thereby, not only the hole but also the electron concentration, and hence their free energy, is reduced. However, because the recombination takes place just before the electron extraction, the extracted free energy of the electron will be strongly limited to its locally reduced value. This is in strong contrast to recombination far away from the contacts. For such a spatially separated recombination the free energy can still be higher in the region where the carrier extraction eventually takes place. This localized recombination due to non-ideal contacts results in a V_{oc} which deviates from the spatially averaged V_{oc}^{imp}.

To summarize, the extracted V_{oc} strongly deviates from the E_g and for the vast majority of absorbers even from V_{oc}^{rad}.[17] Because non-radiative recombination and non-ideal contacts cause such widely encountered practical limitations, especially for nanowire solar cells, they stand in the focus of this thesis.

1.3 Nanowire photovoltaics

Semiconductor nanowires are among the most promising candidates for next generation photovoltaics. This is due to their outstanding optical and electrical properties which profoundly impact the energy conversion process.

An efficient solar cell needs to absorb all of the incident light. The inefficient absorption of photons with energies far above and below the band gap is a large loss in the overall energy conversion process. One way to overcome this loss, is the utilization of multiple materials with different band gaps, so called tandem solar cells, which absorb several parts of the solar spectrum highly efficiently.[18]

However, photon absorption is inherently a stochastic process, therefore it does not occur instantaneously upon entrance into the semiconductor. The photons encounter a certain absorption probability for each incremental distance they pass through the material. This probability increases with increasing photon energy but depends on the exact material properties. For example, direct band gap semiconductors have a higher absorption probability than semiconductors with an indirect band gap, because the latter require the additional interaction with a phonon.[19] Therefore, to ensure that close to all of the light is absorbed, a certain absorption length is required. If the semiconductor is for example too thin, not only low energy photons but even photons with high energies cannot be absorbed completely, together with photons that have been reflected off the surface (Fig.1.2(2c)). As a result, for an indirect band gap semiconductor with a relatively low absorption coefficient, such as silicon, a hundreds of micrometer thick wafer-based geometry has to be chosen for complete absorption. If a direct band gap semiconductor, such as GaAs, is employed, the high absorption coefficient translates into a vastly reduced absorber thickness, down to a few micrometers (Fig.1.3(a)). To ensure that the incident light enters the absorber, an anti-reflection texture and coating have to be employed (Fig.1.3(b)).
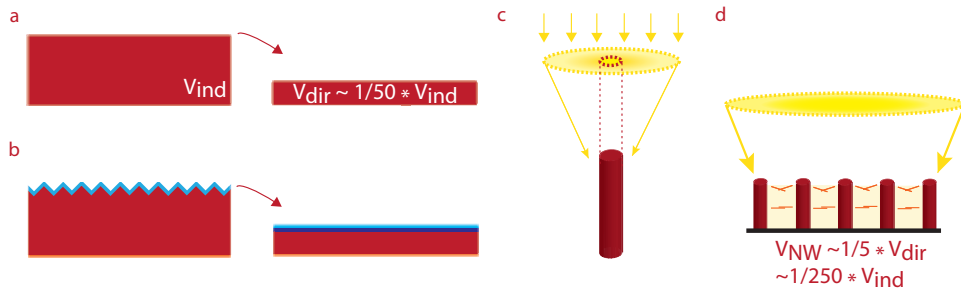
Figure 1.3: Benefits of the nanowire geometry for photovoltaics. (a) Volume requirements for indirect and direct band gap semiconductors to reach full absorption. (b) Anti-reflection coatings and textures for indirect and direct band gap semiconductors. (c) A larger optical than geometrical cross section increases the short-circuit current density of a nanowire. (d) The optical properties lead to a substantial volume reduction for full absorption in nanowire array solar cells.

If the absorber is structured on the nanoscale, such as in the nanowire geometry, resonances can occur that result in optical cross sections that can exceed the physical material boundaries (Fig.1.3(c)). As a result, the nanostructured semiconductor is able to absorb not only directly incident but also adjacent light. If arranged in a nanowire array geometry, additional beneficial effects, such as in-plane diffraction and scattering to nearby nanowires can occur. The large optical cross sections together with the array effects are a great benefit of nanowires compared to both thin-film and wafer-based solar cells; they lead to full light absorption and hence maximum short-circuit current densities even though much less material and no additional anti-reflection coatings are employed (Fig. 1.3(d)).

Besides the outstanding absorption properties, high short-circuit current densities are supported via the so called core-shell geometry (Fig.1.4). For wafer or thin-film geometries, the carrier extraction happens over the same length scale as the light absorption. The carriers need to be extracted up to hundreds of micrometers through the bulk of a potentially defect-rich material. In contrast, the nanowire geometry allows for radial charge carrier extraction, that is perpendicular to the incident light. The nanowire core consists of one carrier selective contact (e.g. for electrons), while the shell provides the second for the opposite carrier type (e.g. holes). Usually those two regions are composed of semiconductors with a different doping type, that is an n-doped region for the electron contact and a p-doped region for the hole contact. In this configuration, the separated charge carriers need to pass through the several μm-long core which increases the series resistance. In this thesis we show that the semiconductor core can be replaced by a metal; we realize the first metal-semiconductor core-shell nanowire solar cell. Such a structure potentially strongly reduces the series resistance due to the superior conductivity of the metal. In both core-shell geometries the carriers only need to be extracted over a short distance (≤ 100 nm) which greatly reduces the probability of radiative and non-radiative recombination events ((2,3) in Fig.1.2); that is a lower carrier diffusion length is required (Fig. 1.4).
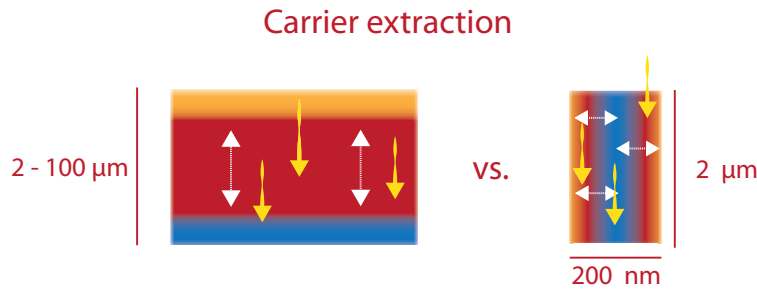
Figure 1.4: Radial charge carrier extraction. Another potential benefit is the charge carrier extraction perpendicular to the incident light, which leads to a reduction of the required minority carrier diffusion lengths. Yellow and white arrows represent the incident light and charge carrier extraction, respectively. The blue and orange regions represent the carrier selective contacts.
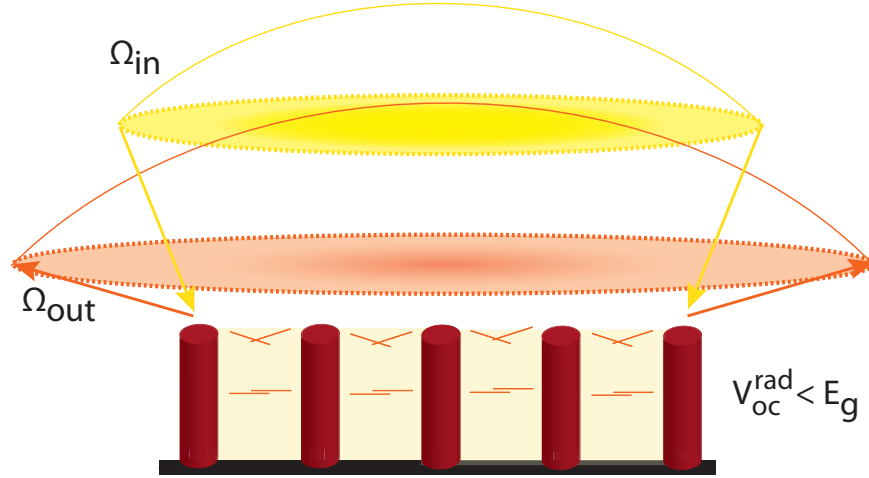
Figure 1.5: Solid angle expansion. Nanowire solar cells lead to an expansion of the solid angle between the incident Ω_{in} and outgoing light Ω_{out} as do macroscopic solar cells. Therefore, the internal carrier concentration and hence radiative open-circuit voltage V_{oc}^{rad} is substantially lower than the band gap energy.

However, to accurately evaluate the overall potential of nanowire solar cells, the effect on the open-circuit voltage has to be considered (right side of Fig.1.2). The nanowire geometry will not only affect the light absorption, but also the light emission. As is the case for macroscopic solar cells, nanowire (array) solar cells can emit light into a larger solid angle than the incident light, i.e. $\Omega_{out} > \Omega_{in}$ (Fig.1.5). As a result, the sustained carrier concentration inside the semiconductor is reduced, compared to the case for which the emission is limited into the direction of absorption ($\Omega_{out} = \Omega_{in}$). To determine the radiative open-circuit voltage limit of nanowire array solar cells accurately, the optical properties have to be studied closely, depending on the exact material parameters.[20, 21]

However, as for most macroscopic solar cells, a large gap exists between the practical V_{oc} and the radiative limit V_{oc}^{rad}. Non-radiative recombination sets currently all practical limits for nanowire solar cells and the mitigation thereof is hence the focus of this thesis. This kind of recombination can happen at bulk or surface defects that are intrinsically linked to the material, such as interstitials, vacancies, dangling bonds, grain boundaries or dislocations. Additionally, unintended impurity incorporation during manufacturing, e.g. via incorporation of metal ions from a growth catalyst, can increase the defect density further.[22] Those impurity and crystal defects can lead to deep energy levels inside the band gap of the semiconductor, where the charge carriers rapidly recombine and transfer their energy into phonons or low-energy photons (Fig. 1.2). For nanowires, due to their high surface-to-volume ratio compared to macroscopic cells, surface recombination dominates. The discontinuous crystal lattice at the surface (dangling bonds) offers a high density of defects (Fig. 1.6).

$$\frac{\text{surface}_{\text{NW array}}}{\text{volume}_{\text{NW array}}} \sim 15 \text{ x } \frac{\text{surface}_{\text{wafer}}}{\text{volume}_{\text{wafer}}}$$

Fermi level pinning

metal/ TCO

p-doped absorber

h$^+$ - contact

inverted absorber
(Schottky/MIS)

bulk recombination

h$^+$ transport layer/
high WF metal oxide

absorber

surface recombination

n-doped absorber

inverted absorber
(Schottky/MIS)

e$^-$ - contact

metal/ TCO

e$^-$ transport layer/
low WF metal oxide

Fermi level pinning

Figure 1.6: Challenging interfaces. Due to the high surface-to-volume ratio of nanowires, surface recombination and Fermi level pinning can have a pronounced impact on the final device performance. Another important property is contact selectivity (right side). Traditionally, a solar cell employs n- or p-doped regions. However, other schemes hold great potential, especially for the nanowire geometry, with its particular challenges such as inhomogeneities in the radial and axial dopant profile.

Consequently the most efficient nanowire solar cells to date employ either materials with a relatively low intrinsic surface recombination, such as wurtzite InP nanowires, or use additional high quality surface passivation layers, such as GaAs nanowire solar cells.[13, 14, 23] Without proper surface passivation many materials, such as GaAs or Si, lead to highly depleted nanowires, i.e. almost all of the photogenerated charge carriers recombine at surface defects.

Furthermore, unpassivated interface defects can fix the free energy of the carriers at a defect level, irrespective of the doping type and density of the bulk material. This Fermi level pinning, which is often induced by the adjacent metal, inhibits the efficient extraction of charge carriers with a photo-induced potential (quasi-Fermi level splitting). Besides creating extraction barriers at contact interfaces, Fermi level pinning at surface defects can cause additional non-radiative recombination. If the Fermi level position at the defect inverts the conduction type of the bulk material in a region close to the surface, minority carriers can move freely from the bulk towards the surface (towards a lower free energy). The bulk minority carriers

encounter a newly increased conductivity, which provides new pathways towards surface defects and eventual non-radiative decay.

Besides non-radiative surface recombination and Fermi level pinning, carrier selective contacts deserve special consideration for the nanowire geometry (right side of Fig. 1.6). Nanowire solar cells, like most traditional solar cells, mainly rely on impurity doping to create the desired selectivity.[22] While impurity doping is widely established in the wafer-based semiconductor industry, it becomes increasingly difficult with decreasing dimensions. The precise doping control for nanowires in the sub-μm range is very challenging and generally strongly affected by the exact nanowire geometry and growth conditions. The doping profile of a nanowire can change unintentionally along the diameter, due to strain-effects of the crystal lattice and different dopant incorporation rates during the growth.[22, 24, 25] Furthermore, the highly doped contact regions are strongly affected by radiative and Auger recombination which only represent a small fraction in a wafer-based solar cell. For a nanowire device, this region can amount to a substantial fraction of the whole material and can strongly affect the overall performance (Fig.1.6). If the highly recombination active region directly points towards the incoming light, parasitic absorption strongly limits the overall efficiency.

For macroscopic solar cells, new generations of selective contacts have been developed that solely rely on carefully chosen surface layers.[26–28] In this thesis, we propose to extend their application to nanowires, because of the particular issues encountered for nanowire doping. We show that by applying the interfacial layer MoO_x, together with an HF treatment, we are able to mitigate negative effects due to inhomogeneous and insufficient dopant incorporation during the growth. Using our insights from those selective contacts for single nanowire devices, we are able to propose a highly promising application. In the last chapter of this thesis, we propose a nanowire array solar cell manufacturing process centered around a reusable substrate and mechanical peel-off step. This fabrication process exploits the intrinsic advantages that emerge from the nanowire geometry compared to thin-films; fast and flexible growth, reduced material consumption, fast mechanical peel-off and intrinsic anti-reflection properties.

So far nanowire solar cells are limited to efficiencies < 20%. Improvements in the past have mainly been achieved by improving the optics, that is the absorption has been enhanced due to an optimized array design (width, length, tapering and array pitch), and because of improved nanowire fabrication methods (crystal growth, etching). By turning the attention towards the electronics, in particular novel selective contacts and passivation layers, nanowire solar cells have the chance to finally close the gap between their practical and thermodynamic efficiency limits.

1.4   Outline of this thesis

Surface passivation and highly-selective contacts are of prime importance for an efficient solar cell. Nanoscale photovoltaics have a very high surface-to-volume ratio, therefore the interface properties are of utmost importance. Furthermore, the high crystal quality (often monocrystallinity) of single nanowire devices reduces the density of crystal defects, such as grain boundaries and dislocations. In this thesis, nanowires are therefore chosen as a highly sensitive platform to study the impact of surface and contact interface properties on the overall photovoltaic performance and to propose device designs for more efficient nanowire array solar cells.

In **Chapter 2**, we study the photovoltaic performance of a new promising nanowire geometry; a metal-semiconductor core-shell nanowire. This type of nanowire has theoretically been predicted to provide outstanding optical absorption in the semiconductor shell and a short required minority carrier diffusion length. Furthermore, it benefits from direct carrier extraction via the metal core, potentially reducing the series resistance of the device as compared to core-shell geometries that consist solely of semiconductors. However, it is well known that the direct contact between a metal and a semiconductor can cause increased recombination, Fermi level pinning and charge carrier extraction barriers. Those issues are usually encountered for metal-semiconductor interfaces that are highly disordered on an atomic scale. We show, that even though the semiconductor shell grows epitaxially off of the metal core, that is the interface is highly ordered, charge carrier extraction barriers and enhanced interfacial recombination can still be observed.

In **Chapter 3**, we study a metal-insulator-semiconductor solar cell, that mitigates the direct and detrimental contact between a metal and a semiconductor by utilizing a thin passivating and insulating interlayer. We employ a metal nanowire network as front electrode on a silicon wafer-based solar cell, because of the potential for highly homogenous charge carrier extraction. We are able to fabricate devices with a power conversion efficiency of 11% (after correction, V_{oc} = 560 mV, J_{sc} = 33 mA/cm^2). For a metal-insulator-semiconductor solar cell, the V_{oc} depends strongly on the work function difference between the metal and the semiconductor. Based on the employed materials (Au/Pd/Al$_2$O$_3$/ Si) we conclude that a charge-neutrality-level at the metal-dielectric interface is likely to lower the metal work function from its vacuum value and hence negatively impacts the measured V_{oc}. A future change towards SiO$_2$ has the potential to increase the open-circuit voltage substantially. The short-circuit current density is strongly affected by reflection and parasitic absorption. Therefore, we introduce nanopyramids integrated in between the metal nanowire network, that substantially reduce reflection and hence increase the short-circuit current density.

In **Chapter 4** we turn our focus back to semiconductor nanowires. Those nanoscale structures have a higher optical than geometrical cross section; they absorb not only light that is directly incident on the physical material boundaries but also adjacent light. While this property can be of great use, especially in

terms of reduced material volume, it complicates the characterization of isolated nanoscale devices. *A priori* the absorption cross section is unknown and changing with wavelength. Hence, it is unclear how much of the incident light directly interacts with the single nanoscale device. This prevents quantification of the different conversion steps and loss mechanisms, but also the quantification of the absolute radiative limit V_{oc}^{rad}. For this thesis it is of great importance to quantify non-radiative recombination and non-ideal contacts. To that end, we focus on InP nanowires that have been used to reach the highest nanowire array solar cell efficiencies to date. We introduce a new measurement technique, integrating sphere microscopy, to accurately quantify the remaining loss mechanisms. We measure the internal quantum efficiency (IQE), the photoluminescence quantum yield (PLQY) and the nanoscale equivalent of the EQE (external quantum efficiency) of a single nanowire device for the first time. Using integrating sphere microscopy, we are able to quantify the impact of non-ideal contacts and non-radiative recombination in order to understand how much can be gained by reducing those loss mechanisms.

In **Chapter 5** we focus on the surface properties of InP nanowires. We study the device performance of contacted and masked single nanowire devices before and after HF, MoO_x and sulfur treatments. We show improved surface passivation and increased carrier selectivity with HF treatment. The limited contact selectivity we encountered in Chapter 4 is likely to be related to Fermi level pinning close to the conduction band due to the native oxide and the high diffusivity of the p-type dopant Zn. Therefore, we introduce the interfacial layer MoO_x for nanowire solar cells, which allows us to increase the open-circuit voltage by up to 335 mV, from 500 mV to 835 mV. To electrically passivate the InP surface and protect it against oxidation, we study the influence of sulfurization. We show preliminary results that prove sulfurization can indeed increase the V_{oc} by removing the native oxide and potentially even passivate the surface against reoxidation.

In **Chapter 6**, we explore valorization opportunities that emerge out of our insights from the preceding chapters. In the previous chapters we have shown how to contact single p-type InP nanowires for high performance devices, which has been an unsolved issue in the past. Translating those insights to array solar cells allows us to propose a process line which exploits the intrinsic advantages that emerge from the nanowire geometry compared to thin-films; faster growth speeds, reduced material consumption, fast mechanical peel-off and intrinsic anti-reflection properties. We perform a techno-economic analysis on our proposed fabrication process by comparing the technology to already existing and very similar manufacturing lines for thin-film GaAs solar cells. We include different nanowire growth methods that are promising approaches towards reducing the costs further. The ability to consider various growth methods points towards another characteristic: the process line is highly flexible and not limited to one growth method or semiconductor. We argue that this can have great impact on the rate of innovation in a hypothetical company invested in this process. Finally, we propose a roadmap for future developments and commercialization.

2

Au-Cu$_2$O core-shell nanowire photovoltaics

The electrical properties of semiconductor nanowires strongly depend on the realized junction and electrode geometry (axial vs. radial). For radial charge carrier extraction the required minority carrier diffusion length is on the order of 10-100 nm and therefore strongly relaxed compared to bulk solar cells. To this end, we study metal-semiconductor core-shell nanowires, which have been predicted to show even better optical absorption than solid semiconductor nanowires, with the additional advantage of a local metal core contact for radial charge carrier extraction. We fabricate and analyze such a geometry using a single Au-Cu$_2$O core-shell nanowire photovoltaic cell as a model system. Spatially-resolved photocurrent maps reveal that although the minority carrier diffusion length in the Cu$_2$O shell is less than 1 μm, the radial contact geometry with the incorporated metal electrode still allows for photogenerated carrier collection along an entire nanowire. Current-voltage measurements yield an open-circuit voltage of 600 mV under laser illumination and a dark diode turn-on voltage of around 1V. This study suggests the metal-semiconductor core-shell nanowire concept could be extended to low-cost, large-scale photovoltaic devices, but stresses the importance of careful interface engineering.
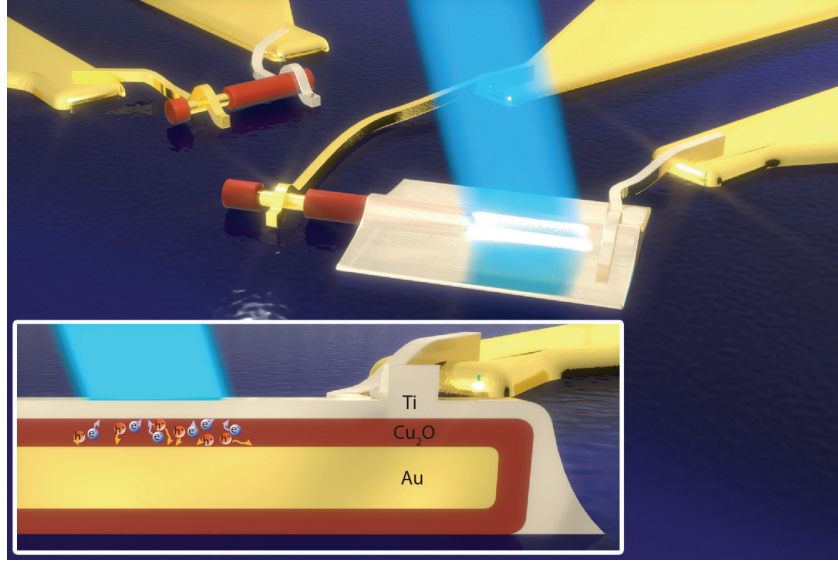
Figure 2.1: Schematic drawing of the metal-semiconductor core-shell geometry. Two devices are electrically connected to electrodes and a laser beam (bright blue) is incident on one of them. The Au electrode contacts the Au core while a Ti electrode contacts the Cu$_2$O shell (red) only at the end (top left) or along most of the length via an additional thin Ti pad (center). The inset shows a cross section of the device geometry. The incident light creates electron-hole pairs (e-, h+), which are extracted via the shell and the core, respectively.

2.1 Introduction

2.1.1 Cu$_2$O as photovoltaic material

Cuprous oxide (Cu$_2$O) is an earth abundant and non-toxic semiconductor that can be grown using many different fabrication methods including evaporation and sputtering. Its direct band gap of ~2.0 eV provides the potential to reach power conversion efficiencies of up to 20%. This combination of abundance, simple fabrication and efficiency potential has therefore made Cu$_2$O a popular choice for thin-film solar cell research since the early days of photovoltaics.[29][30] Assuming that excellent surface passivation can be achieved, thin-film solar cells can in general even reach higher open-circuit voltage (V_{oc}) values than their bulk counter parts due to shorter charge carrier extraction paths and hence reduced bulk recombination.[31] Cu$_2$O has a band gap that is close to the ideal value for a silicon-based tandem solar (1.7-2.0 eV), making it a candidate for high efficiency photovoltaics.[32–34] Recently, several groups have focused on the interface properties of Cu$_2$O and were able to increase the V_{oc} up to 1.2 V by using interfacial layers, such as Ga$_2$O$_3$ and ZnO, combined with transparent conductive oxides (TCOs) as top contacts.[35–43]

### 2.1.2 Metal-semiconductor core-shell nanowire

Here we utilize a metal-semiconductor core-shell geometry to fabricate a single horizontally aligned Au-Cu_2O nanowire photovoltaic cell. Such a structure has several potential advantages. The thin semiconductor shell in direct vicinity of the metal core electrode allows for facile extraction of photogenerated carriers, even in materials with short minority carrier diffusion lengths. The radial core-shell geometry has already proven useful in semiconductor nanowire photovoltaics and we expect even better charge carrier extraction in our geometry where photocarriers are injected into the metal immediately.[44–47] Another previously demonstrated advantage of semiconductor nanowires is their high absorption cross section, which can exceed the geometrical one.[23, 48, 49] The metal-semiconductor core-shell structure can lead to even higher absorption, while further reducing the amount of semiconductor.[50] Several research groups have already utilized metal-semiconductor core-shell nanospheres or rods for plasmon mediated charge carrier dynamics for photovoltaics and photocatalysis. In these examples however, semiconductor materials were not used for the visible light absorption or materials were suspended completely in solution.[51–57] Here we fabricate and test a single metal-semiconductor core-shell nanowire photovoltaic cell, utilizing Au for the core and Cu_2O for the shell.

2.2 Results

To fabricate the core-shell nanowires, we followed a procedure developed by Sciacca *et al.* for solution-based synthesis of metal (Ag, Au or Cu) core Cu_2O shell nanowires.[58] The metal nanowires were synthesized using the polyol process and subsequently coated with a Cu_2O shell at room temperature in aqueous solution, adapting a protocol originally developed for core-shell nanoparticles.[59, 60] This specific Cu_2O synthesis route was chosen over other methods to produce Cu_2O nanowires because it allowed for epitaxial growth on metal nanowires suspended in solution.[61, 62] Photoluminescence (PL) measurements showed a peak near 1.9 eV, similar to what has been observed in pure-phase, bulk Cu_2O.[58, 63]

Figure 2.1 shows a schematic of a single nanowire photovoltaic cell illuminated by a laser beam. As can be seen in the drawing, the Cu_2O shell has two contacts: one that collects photogenerated holes and one that is selective for photogenerated electrons. One simple and effective method for inducing this carrier selectivity is to use metal contacts with different work functions such that one metal makes an Ohmic contact to the Cu_2O and the other a Schottky junction.[19]

Here we have chosen Au as the metal nanowire core because it has a large work function (~ 5.4 eV; similar to that of Cu_2O) and makes an Ohmic contact to Cu_2O. Furthermore Au has a high chemical stability, low lattice mismatch with Cu_2O (~ 4%) and a simple nanowire synthesis route.[58, 64–67] As the Schottky contact we have chosen Ti, which has a low work function (~ 4.3 eV), excellent adhesion to many materials and a stable surface oxide.[68]
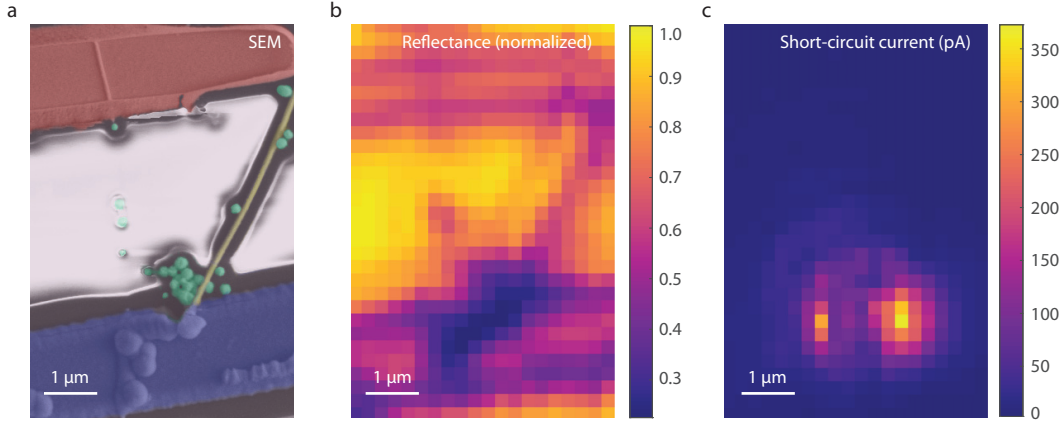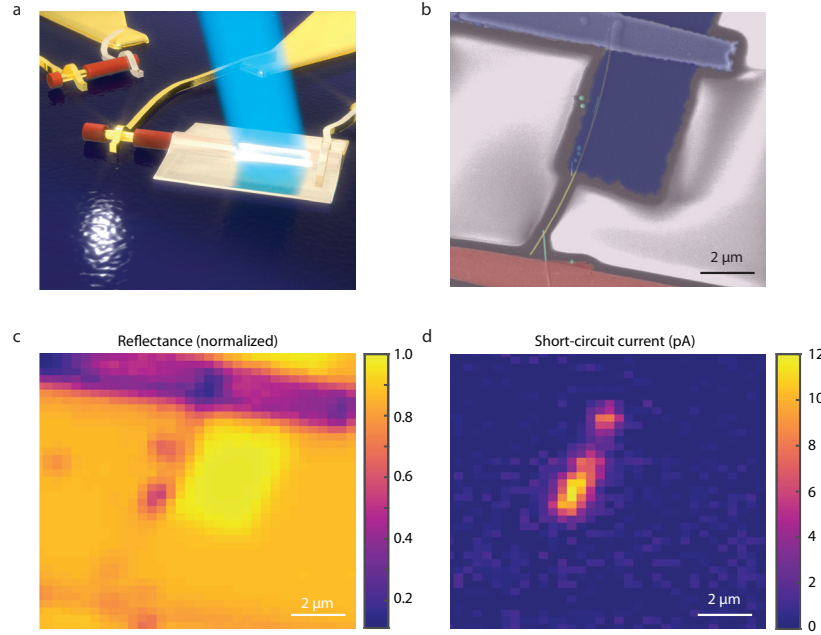
Figure 2.2: Single nanowire photovoltaic with radial charge carrier collection.
(a) False-colored SEM image of a nanowire (yellow) connected between Ti (blue) and Au (red) contacts. (b) Optical reflection image. (c) Photocurrent map with an incident laser power of 42 μW, polarization perpendicular to the nanowire axis, a spot size of ~1 μm, and illumination wavelength of 405 nm. The local photocurrent collection next to the Ti contact is clearly visible.

To fabricate such samples, we started with Si$_3$N$_4$ covered Si substrates with evaporated Au electrodes. The core-shell nanowires were contacted using electron beam lithography and metal evaporation. The optical characterization was conducted with a tunable laser source in the range of 405 nm - 750 nm. The light was focused through an objective lens to a spot size of ~ 1 μm onto the electrically connected single nanowire photovoltaic cells. The details of the device fabrication and characterization can be found in the supporting information.

Figure 2.2(a) shows a colored scanning electron microscope (SEM) image of a typical single nanowire photovoltaic cell (yellow). The reflection map in Figure 2.2(b) shows the diagonal orientation relative to the parallel contact pads. Figure 2.2(c) shows photocurrent generation of up to 350 pA under 42 μW laser illumination at λ = 405 nm. The localized charge carrier collection only occurs near the Ti contact finger, where the Schottky junction induces a built-in electric field, such that the minority charge carriers do not have to travel long distances to get extracted. Due to the optically thick Ti contact we do not expect any substantial contribution to the photocurrent from the Cu$_2$O regions under the contact. This photocurrent collection localized only close to the Ti contact suggests that the minority carrier diffusion length is less than or equal to the beam spot size of ~1 μm, consistent with reported values for Cu$_2$O synthesized by different methods.[69, 70]

Despite the excellent crystallinity and epitaxial shell growth in these core-shell nanowires, the high surface and contact areas could lead to even shorter minority carrier diffusion lengths, as these are known to be sources of increased non-radiative recombination in bulk solar cells.[19] Future studies involving thin interfacial spacing layers and surface passivation are needed to quantify the importance

Figure 2.3: Extended radial charge carrier collection. (a) Schematic of singe nanowire with employed Ti pad. (b) Colored SEM image of a nanowire connected between Ti (blue) and Au (red) contacts and partially covered by a 10 nm thin Ti pad (blue). (b) Reflectance map. (c) Photocurrent map with an incident laser power of 7 μW, polarization perpendicular to the nanowire axis, a spot size of 1 μm, and illumination wavelength of 405 nm. The photocurrent collection is extended by the presence of the Ti pad.

of these effects and our single core-shell nanowire geometry provides a perfect platform for such studies.

To directly probe the importance of the radial built-in field and carrier collection mechanism, we have compared the above results to the case where a 10 nm thin Ti pad covers approximately 2/3 of the nanowire (Figure 2.3(a)). This arrangement is closer to a realistic large-scale device, where the whole nanowire would be covered with an additional contact (either a transparent conductive oxide or a continuous thick metal layer with illumination through a transparent substrate). Figure 2.3(b) shows a false-colored SEM image of the device, with a Ti pad (blue) on top of the nanowire (yellow), which is connected between a Ti (blue) and an Au (red) contact. Figure 2.3(c) shows the reflection image and Figure 2.3(d) the respective photocurrent map under 7 μW laser illumination at $\lambda = 405$ nm, which reveals photocurrent collection from an extended elongated area. This photocurrent profile demonstrates charge carrier collection from the nanowire along the entire length covered by the Ti pad. This supports the idea that charge carriers generated by light passing through the 10 nm Ti pad can be separated and collected at the metal core and the Ti top contact. The maximum photocurrent is around 25
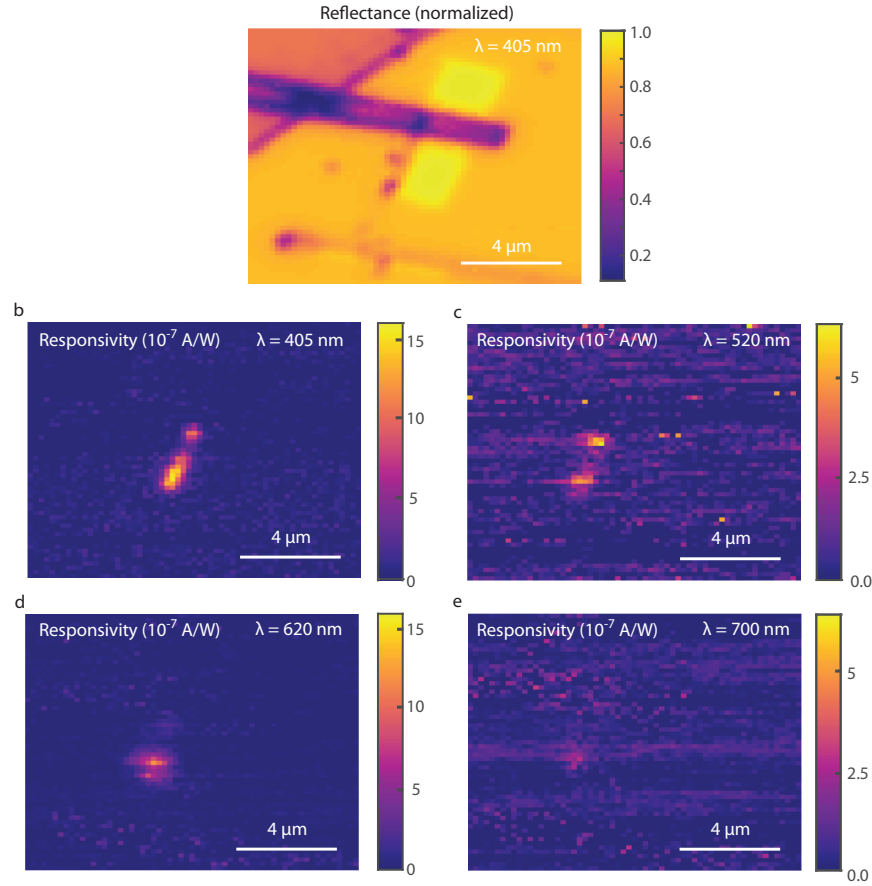
Figure 2.4: Spectral response of single nanowire. (a) Reflectance map of the nanowire at 405 nm. (b-e) Responsivity maps at laser wavelengths of (b) 405 nm, (c) 520 nm, (d) 620 nm and (e) 700 nm. The responsivity was obtained by first subtracting the background values and subsequently dividing by the incident laser power, to facilitate comparison. In all cases the laser polarization was perpendicular to the nanowire axis. The spatial shift of the photocurrent with increasing wavelengths is due to chromatic aberration of the objective lens and drift in the mechanical stage.

times smaller than in the axial collection case shown in Figure 2.2, which can be attributed to the reduction in incident power from 42 to 7 μW and the substantially reduced absorption in the wire due to the Ti pad. The responsivity (photocurrent after background subtraction divided by the incident laser power) is only lowered by a factor of four by the Ti pad. These results prove the utility of this concept: photocurrent collection can take place along the whole length of the nanowire, even with materials that have very short minority carrier diffusion lengths.

To investigate the core-shell nanowire spectral response, we map the responsivity under 405 nm, 520 nm, 620 nm and 700 nm laser illumination (Figure 2.4(b)-2.4(e), respectively). The polarization was perpendicular to the nanowire axis for all

measurements, which is the polarization that supports plasmon resonances. In the other polarization we observed weaker currents. Currently, we can not distinguish between charge carrier generation due to band-to-band absorption in the Cu_2O and plasmon-mediated transfer mechanisms, such as resonance energy transfer, direct energy transfer and hot carrier injection.[51, 71–75]

The strong reduction in photocurrent for λ = 700 nm is consistent with the literature value of the optical band gap (1.95 eV or 635 nm) and our own single nanowire PL measurements.[58, 76] However, absorption in the Ti pad as well as variations in the optical resonances must be taken into account to quantitatively explain the observed results. Finally, we show single nanowire current-voltage (I-V) measurements in the dark and under laser illumination (Figure 2.5). This nanowire device, which did not contain an extended Ti pad showed clear rectification behavior with a turn on voltage of 1 V in the dark. Under laser illumination with 42 μW power at 405 nm, an I_{sc} of -300 pA and a V_{oc} of 600 mV were observed.

These results clearly demonstrate that single metal-semiconductor core-shell nanowires function as photovoltaic cells. The photocurrent increases at higher reverse voltages and reaches reverse break down before saturating. We attribute this slope to a higher photogenerated carrier collection efficiency at larger reverse bias voltages due to an increased depletion region. Furthermore, we observe a substantial charge carrier extraction barrier and hence s-shaped I-V curve, which is a well-known phenomenon that can be attributed to accumulated space charges at the material interfaces or a non-ideal Ohmic contact.[77–80] This observation
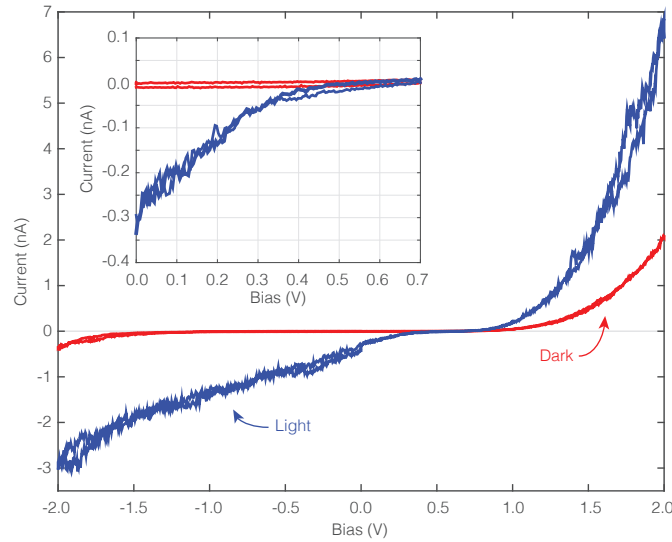
Figure 2.5: I-V curves of single Au-Cu$_2$O nanowire photovoltaic. (a) Current-voltage behavior of a single Au-Cu2O core-shell nanowire photovoltaic cell in the dark (red line) and under laser illumination at 405 nm with a power of 42 μW and polarization perpendicular to the nanowire axis (blue). The inset is a magnified view of the region 0 V - 0.6 V of the I-V curves.

can be explained by the non-optimized metal-semiconductor interfaces, which are likely to induce recombination-active trap states and accumulated space charges. We note that the photocurrent under the AM 1.5G spectrum was below the detection limit (~5 pA) of the source measure unit used and therefore did not allow the measurement of our devices under the full solar spectrum. The low photocurrent can partially be explained by the localized Schottky region close to the optically thick Ti contact which is mostly inaccessible for the incident light. Only a small fraction at the edge of the contact can contribute to the photocurrent.

2.3 Conclusions

We have realized for the first time a single metal-semiconductor core-shell nanowire photovoltaic cell. We measured photocurrent maps on individual Au-Cu$_2$O core-shell nanowires, showing charge carrier collection via a Schottky Ti contact on the surface, with the Au core being utilized as an Ohmic contact. The spectral response is consistent with a band gap of ~2 eV. We show that a V_{oc} of 0.6 V and I_{sc} of 300 pA can be achieved without any detailed contact optimization, however only at a very high illumination intensity. By depositing a thin (10 nm) Ti layer over the wire, we clearly demonstrate that two conductive radial metal contacts allow for radial photogenerated carrier collection in semiconductors with short minority carrier diffusion lengths <1 μm.

We observe a strongly s-shaped I-V curve, which is indicative of a charge carrier extraction barrier at one of the two metal interfaces. As also reported in previous literature, it is possible that a redox reaction under the Ti contact converts the Cu$_2$O to TiO$_2$ and Cu at the interface.[81] Furthermore, the direct vicinity of a metal and a semiconductor is well known to cause metal-induced band gap states in the semiconductor which can lead to mid-bandgap Fermi level pinning and hence extraction barriers.[19]

Therefore, we would expect better performance if appropriate interfacial passivation layers could be incorporated, as already demonstrated not only with Cu$_2$O but also other material systems, such as silicon in Chapter 3 of this thesis.[38, 82, 83]

Furthermore, we would expect a further improvement in the device performance for a reversed contact geometry, allowing for a Schottky/metal-insulator-semiconductor junction along the whole length of the metal core. However, the solution growth of a passivating insulator between the metal and the semiconductor and a core-shell structure with a low work function core metal have not been realized so far.[58]

While the limitations discussed above explain the overall low photovoltaic performance of our device, they do not present insurmountable obstacles on the way to high efficiency metal-semiconductor core-shell nanowire solar cells. We note that the metal-semiconductor core-shell nanowire geometry is not limited to the materials used for this proof-of-concept study. An ideal structure would employ low cost metals with appropriate interfacial layers, replacing Au and Ti.

2.4 Supplemental information

2.4.1 Fabrication

Au-Cu$_2$O core-shell nanowires were prepared in solution as described in detail by Sciacca et al.[58] The nanowires had a Au core diameter of ~ 50 nm and a Cu$_2$O shell thickness of ~ 30 nm and were then dropcast onto 3 x 3 mm^2 low-stress LPCVD-Si$_3$N$_4$ (~ 300 nm) covered Si chips with evaporated Au electrodes (~ 150 nm). The core-shell nanowires were contacted using a 2 or 3 - step electron beam lithography and metal evaporation scheme. The Cu$_2$O shell was locally etched for 1-2 min with 0.1 mM sulfuric acid prior to Au evaporation (~ 200 nm) for the core contact, while the Ti contact (~ 200 nm) was directly evaporated on the Cu$_2$O shell. For the experiments with the 10 nm thin Ti pad, an additional resist exposure and evaporation step was conducted prior to the thick Ti shell contact finger formation. For the multi-step electron beam lithography process, pre-patterned alignment markers on the substrates were used to align subsequent exposure patterns to the correct nanowire and electrode locations.

2.4.2 Characterization

The optical characterization was conducted with a home-built laser setup. A super-continuum laser (Fianium WL-SC390-3) was sent through an acousto-optic tunable filter (Fianium AOTF-V1-N1) to select wavelengths in the range of 410 nm - 750 nm. The polarization was controlled with a $\lambda/2$ plate (Thorlabs) before the light was focused through an objective lens (Mitutoyo M PLAN APO NUV 50X) to a spot with waist w_0 ~ 600 nm on the electrically connected single nanowire photovoltaic cells. The substrate was mounted on and wire bonded to a custom designed printed circuit board to facilitate the electrical connections. Then the substrate was scanned relative to the focused beam position with a 3-axis piezoelectric stage (Piezosystem Jena Tritor 400 CAP). The photocurrent was measured with an Agilent B2902A source-measure unit, while simultaneously recording the reflected and incident beam power (both measured with Thorlabs amplified photodiodes model PDA100A) to correlate the current with the position of the laser spot and to normalize to variations in the laser power during a single measurement. The absolute beam power was measured using a calibrated silicon photodetector (Newport model 818-UV-L). The I-V curves were also measured with the source-measure unit (Agilent B2902A).

3

Metal-insulator-semiconductor nanowire network solar cells

Metal-insulator-semiconductor (MIS) junctions provide the charge separating properties of Schottky junctions while circumventing the direct and detrimental contact of the metal with the semiconductor. A passivating and tunnel dielectric is used as a separation layer to reduce carrier recombination and remove Fermi level pinning. When applied to solar cells, these junctions result in two main advantages over traditional p-n-junction solar cells: a highly simplified fabrication process and excellent passivation properties and hence high open-circuit voltages. However, one major drawback of MIS solar cells is that a continuous metal layer is needed to form a homogeneous junction at the surface of the silicon, which decreases the optical transmittance and hence short-circuit current density. The decrease of transmittance with increasing metal coverage can, however, be overcome by nanoscale structures. Nanowire networks exhibit precisely the properties that are required for MIS solar cells: closely spaced and conductive metal wires, to induce an inversion layer for homogeneous charge carrier extraction, and simultaneously a high optical transparency. We experimentally demonstrate the nanowire MIS concept by using it to make silicon solar cells with a measured energy conversion efficiency of 7 % (~ 11% after correction). Furthermore, we introduce inverted nanopyramids integrated between the metal nanowire network, decreasing the reflectivity substantially from 36% to ~ 4%.

3.1 Introduction

When a metal contacts a semiconductor, a carrier selective Schottky junction can be formed. The resulting conduction type inversion in the semiconductor depends on the metal and semiconductor work function difference. For example, when n-type silicon directly contacts a high work function metal (Au), the conductivity for electrons falls below the conductivity for holes close to the surface. This inversion of the majority carrier conduction type causes the carrier selective properties of Schottky junctions. However, as also shown in Chapter 2 the direct contact between metal and semiconductor can increase surface recombination due to metal-induced band gap states and dangling bonds and can even lead to Fermi level pinning at the semiconductor surface.[84] Metal-insulator-semiconductor (MIS) junctions circumvent those problems by separating the metal and semiconductor with a thin tunnel and passivating dielectric.[85] Furthermore, interface charges at the dielectric semiconductor interface can increase the magnitude of the conduction type inversion in the semiconductor.[86]

Because of their charge selective and passivating properties, MIS junctions were successfully used to make silicon solar cells starting in the 1970s.[87, 88] The MIS solar cell device architecture has two main advantages over traditional p-n junction cells: (1) highly simplified fabrication and (2) excellent passivation of the semiconductor even under the contact.[87, 89] For traditional solar cells, highly doped regions are required to induce the charge selectivity, with the disadvantage of increased Auger recombination. The reduced carrier recombination of MIS solar cells led to open-circuit voltage (V_{oc}) values of up to 655 mV, surpassing those of traditional p-n junction solar cells in early development stages.[85] More recently, the extraordinary potential of the MIS concept has emerged again, with recent record silicon solar cells employing a carrier selective, tunnel oxide passivated contact at the back side, which is conceptually identical to the MIS structure.[89–91] Furthermore, the MIS junction has emerged as one of the most successful interfaces in photocatalysis in recent years, where the metal induces charge separation, catalyzes the chemical reaction and protects the underlying semiconductor.[92–95]

One major difficulty in applying MIS contacts to the front of a solar cell is the increased reflection due to the required metal coverage for homogenous junction formation. Early generations of MIS solar cells utilized thin metal layers and hence exhibited low short-circuit current densities (J_{sc}), while advanced generations introduced widely spaced macroscopic contact fingers which reduced the reflection substantially and led to substantial performance improvements.[96] To form a homogenous junction under the whole surface, additional dielectric layers with a high fixed charge density were employed, which however were insufficient to induce junction properties similar to diffused junctions or continuous metal layers.[96] Therefore, a low reflectivity combined with a high quality homogenous MIS junction over the entire surface, which is especially needed for materials with short carrier diffusion lengths, remains to be a challenge for the MIS device architecture. The decrease of transmittance with increasing metal coverage of homogenous

MIS junctions can be overcome by nanoscale structures. Even though their electrical performance approaches those of continuous thin-films, engineered metal nanowire networks have been demonstrated to exhibit extraordinary transmission, where the transmission is larger than expected from geometric considerations.[97–102] Furthermore, nanowire networks can be fabricated on a large scale with roll-to-roll compatible processes, like nanoimprint lithography, or even using solution-synthesized metal nanowires.[103–106] Therefore, nanowire networks exhibit precisely the properties that are required for MIS solar cells: closely spaced and conductive metal wires, to induce a junction for homogenous carrier extraction, and simultaneously a high optical transparency.

Here, we demonstrate nanowire network based MIS silicon solar cells, by fabricating the nanowire networks on top of passivated silicon half cells using electron beam lithography. By choosing well passivated silicon as a base material, we are able to exclude any effects of short minority carrier diffusion lengths on our results. Our solar cells exhibit a measured conversion efficiency of 7%. After correcting for the influence of the small size of the active area on the V_{oc} and the missing anti-reflection coating on the J_{sc}, we estimate that our MIS solar cells exhibit a corrected power conversion efficiency of $\sim 11\,\%$ with an effective V_{oc} of 560 mV and estimated J_{sc} of 33 mA/cm^2. We perform electron beam-induced current (EBIC) measurements to prove that nanowire networks can be used to form an MIS junction, which leads to homogenous charge carrier extraction. Band diagram simulations allow us to investigate the dependence of the conduction type inversion on the work function difference between the metal and the semiconductor and hence to explain the relatively low V_{oc}. Reflection measurements show that a high metal coverage of the surface with metal nanowire networks only slightly increases reflection compared to a flat silicon surface. Finally, we demonstrate a first step towards improved device performance by using the metal nanowire network not only as a transparent electrode and for the inversion layer formation, but also as an etch mask for surface texturing. We fabricate inverted nanopyramids integrated into the metal nanowire network. As a result, we are able to decrease the reflectivity substantially from 36% to $\sim 4\%$. We use external quantum efficiency (EQE) measurements to estimate the influence of the reduced reflection on the overall device performance and thereby point out a path towards MIS solar cells that exhibit both high V_{oc} and J_{sc} values.

3.2 Experiment

3.2.1 Fabrication

To isolate the effect of the metal nanowire network on the MIS solar cell performance, we use a state-of-the-art contact scheme for the back of the solar cell, which is employed in industrial silicon heterojunction (SHJ) solar cells (Figure 3.1(a)). It consists of 5 nm of intrinsic a-Si:H followed by 8 nm of n-type a-Si:H, 80 nm ITO and 300 nm Ag. Due to the importance of the tunnel and passivation layer, we rely
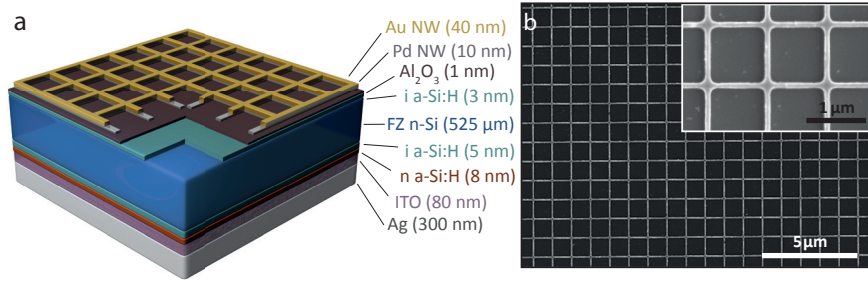
Figure 3.1: Device schematic and SEM of nanowire network. (a) Device schematic, showing the different layers employed for the nanowire network MIS solar cell. Not to scale. (b) SEM images of the nanowire network with 100 nm nanowire width, 50 nm height and 1 μm pitch on top of the silicon half-cell, showing the high uniformity of the nanoscale pattern. A high-resolution SEM is shown as an inset.

on a high quality double layer for the front surface, consisting of 3 nm intrinsic hydrogenated amorphous silicon (a-Si:H), followed by 1 nm of Al_2O_3.[107] The intrinsic a-Si:H is grown by inductively coupled plasma chemical vapor deposition (ICP-CVD) and is used due to the excellent chemical passivation properties on the silicon surface. The Al_2O_3 layer is grown by atomic layer deposition (ALD) and is known for its high stability and insulating properties.[108] When used directly on silicon, ALD Al_2O_3 has been shown to exhibit a high fixed charge density, which can lead to a field effect passivation of the underlying surface.[109–111] Besides the additional passivation effect, the Al_2O_3 also serves as a capping layer to prevent the out diffusion of hydrogen from the intrinsic a-Si:H layer. The metal nanowire network is fabricated by electron beam lithography on small areas (2.4 - 4.5 mm^2) and subsequent metal evaporation of Pd and Au. Pd was chosen due to the high work function to create a strong inversion layer, while Au was used because of lower optical losses than Pd. The low stability of Ag during subsequent processing precluded a possible usage of that metal. To integrate the inverted nanopyramid texturing in between the metal nanowire networks, the networks are fabricated on a silicon wafer, which is subsequently immersed in a KOH solution (further details in Supplemental Information).

3.3 Results

Figure 3.1(b) shows the fabricated Au-Pd nanowire network on top of the passivated substrate. The wires are 100 nm wide, 50 nm high (10 nm Pd/ 40 nm Au) and the pitch is 1 μm. The network is highly uniform and spans an area of 2.4 mm^2. Figure 3.2(a) shows the current density-voltage (J-V) traces of a masked nanowire network MIS solar cell under 1 sun illumination (green) and in the dark (red). The inset shows a schematic of the 2.4 mm^2 solar cell, which is created by fabricating a nanowire network (red) on top of a 2 cm^2 large substrate (blue). The silver back con-

tact (grey), the contact probes (black) and the shadow mask (green) are indicated. The J-V curve in the dark shows a clear rectification. Under 1 sun illumination intensity, an open-circuit voltage (V_{oc}) of 423 mV, a short-circuit current density (J_{sc}) of 23 mA/cm^2 and a fill factor (FF) of 58% are obtained.

To account for the smaller size of the masked collection area (2.4 mm^2) compared to the substrate area (2 cm^2) we calculate the impact on the V_{oc}, with the main effect being the high contribution of the recombination current (I_0) originating from a larger area than the I_{sc}. As explained in detail in the SI, we use two different approaches to estimate the effective V_{oc}, both resulting in the same value of about 560 mV (see Figure 3.5-3.8). Finally, we estimate the current density with an antireflection (AR) (n = 2) coating with 10% residual reflectivity (simulated value), compared to the uncoated solar cell (36% measured reflectivity). Figure 3.2(b) shows a table with the measured and rescaled/estimated solar cell parameters, taking into account the aforementioned effects. As a result, the nanowire network MIS solar cell has an effective V_{oc} of 560 mV, an estimated J_{sc} of 33 mA/cm^2 and a FF of 58%, resulting in an 11% energy conversion efficiency (after correction).

The results show that the metal nanowire network not only gives rise to charge carrier extraction, but also charge carrier separation inside the semiconductor, i.e. the metal nanowire network can potentially be used to replace the traditional contacts of an MIS solar cell. The small spacing of the metal networks makes our MIS concept applicable to materials with minority carrier diffusion lengths ~1 μm, as is the case for many thin-film materials such as CIGS, CdTe, halide perovskites and GaAs (see also Figure 3.3).[112] However, our results also show that our obtained solar cell parameters, i.e. the V_{oc}, J_{sc} and FF, are well below those of state of the

	measured	rescaled/estimated
V_{oc} [mV]	425	560
J_{sc} [$\frac{mA}{cm^2}$]	23	33
FF [%]	58	58
η [%]	7	11
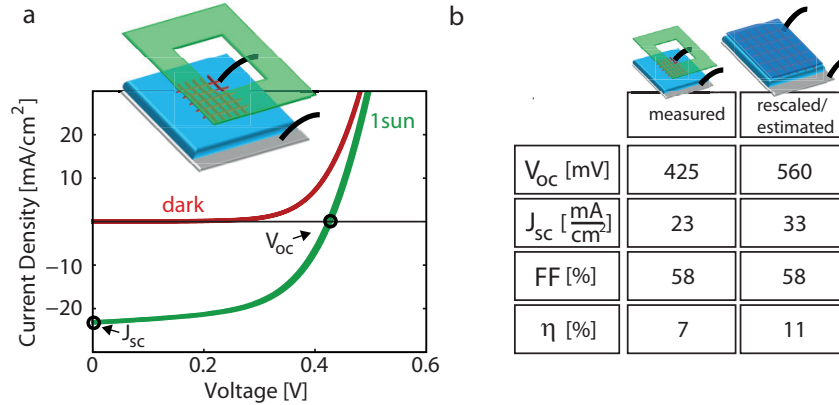
Figure 3.2: Device performance. (a) J-V trace of nanowire network MIS solar cells in the dark (red) and under 1 sun (AM1.5G) illumination intensity (green). The active area shown here has a size of 2.4 mm^2 on a 2 cm^2 substrate. The measurements are performed under masked conditions. The inset shows the experimental geometry, where the nanowire network (red) and the shadow mask (green) are used to define the cell area. (b) Table with the measured and rescaled/estimated solar cell parameters.

art silicon solar cells. Therefore, we conduct the following electrical and optical analyses to get insight into the device performance and to point out crucial steps towards improvements.

Figure 3.9 and 3.10 show band diagram simulations which have been performed to study the dependence of the conduction type inversion, and hence selectivity of the MIS contact, on the work function (WF) difference between the n-type silicon and the adjacent metal. The simulations show that high metal work functions (> 5 eV) can lead to strong conduction type inversion in the underlying silicon, the prerequisite for a high V_{oc}. Conversely, any decrease of the effective metal WF will lead to a decrease in the V_{oc}. After considering other possibilities, we conclude that the cause for the relatively low V_{oc}, when compared to state-of-the-art silicon solar cells (>700 mV), can be the lowering of the Pd vacuum work function due to the presence of the dielectric Al_2O_3. From developments in the field of complementary-metal-oxide-semiconductor (CMOS) transistors, it is known that Fermi level pinning to a charge neutrality level (CNL) in the dielectric can lower the effective work function of the metal.[113–115] Therefore, other dielectrics, e.g. SiO_2, that cause much weaker Fermi level pinning to the CNL should be employed in future devices. However, when searching for alternatives the stability and passivation properties for ultrathin layers have to be kept in mind. For a detailed discussion see SI.

Besides the aforementioned reasons, the typically high costs associated with high WF metals (Ag, Au, Pd, Pt) and their potentially detrimental influence on the material quality (e.g. lifetime) have to be considered. Therefore, high WF oxides (e.g. MoO_x) are a promising alternative as an interfacial layer[28, 116, 117]. The same holds for layers of doped semiconductors, like n-type (and p-type) a-Si:H in high-efficiency silicon heterojunction (SHJ) solar cells.[10, 89, 118] However, as also
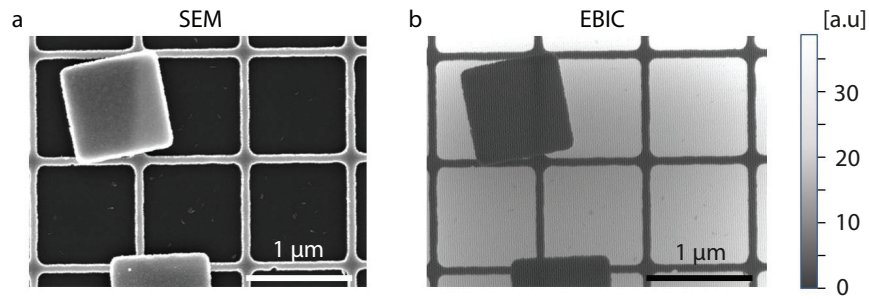
Figure 3.3: Electron-beam-induced-current (EBIC) measurement. (a) SEM image of a region of interest (ROI) of a similar sample to the one shown in Figure 3.2. Two residual metal flakes from the fabrication can be seen. (b) EBIC measurements, showing a uniform charge carrier separation and collection in the ROI due to the closely spaced metal nanowire network and the large carrier diffusion lengths in silicon. We note that the shadowed regions due to the metal nanowires are smaller for a sample under light illumination, because of efficient directional scattering by optical (plasmon) resonances.

our results show (see Figure 3.13) the stability and process compatibility, especially with nanostructuring have to be considered when employing such layers.[119]

Besides the degree of conduction type inversion, the simulations also show that the depth of the inversion layer extends to about 200 nm into the silicon, depending on the metal work function. Given the nanowire network pitch of 1 μm and assuming a constant radial extent of the inversion around the metal as an upper bound, a large fraction of the silicon square between the metal wires is inverted close to the surface. Electron-beam-induced-current (EBIC) measurements (Figure 3.3) show that this conduction type inversion, together with the large diffusion lengths in silicon lead to homogenous carrier collection.

As can be seen in Figure 3.2, the J_{sc} of our solar cell reaches a value of 23 mA/cm^2. We ascribe the primary deviation from state-of-the-art silicon solar cells (~42 mA/cm^2) to the high reflectivity of the uncoated and flat silicon substrate. Therefore, we measure the total reflectance of the completed devices using an integrating sphere setup. Then, we introduce a low reflectivity structure, consisting of nanopyramids integrated in between the nanowire network. We use EQE measurements to estimate the effect on the final device performance, as a first step towards improved J_{sc} values for nanostructured MIS solar cells.

Figure 3.4(a) shows the measured reflection values of the nanowire network solar cell (blue), the network with integrated inverted nanopyramids (orange) and a bare polished silicon surface as reference (green). FDTD Simulations were used to obtain an estimate of the residual reflection when a standard anti-reflection coating (n=2) of 80 nm would be included on top of the flat nanowire network solar cell (violet). The average reflectivity ($\bar{R}$) in the wavelength range from 420 - 900 nm is also shown for the different structures. Figure 3.4(c) shows the measured external quantum efficiency (EQE, extracted charge carriers per incident photon) of the flat nanowire network solar cell (blue line). The curve shows relatively uniform quantum efficiency over the visible range. Taking into account the measured reflection and the simulated absorption in the metal, the internal quantum efficiency (IQE, extracted charge carriers per absorbed photon in the semiconductor) was determined (black line). For wavelengths below the band gap of silicon (1.1 eV) the IQE increases until it reaches unity in the range between 600 - 800 nm. For short wavelengths, the IQE drops to a value of ~ 0.8, indicating charge carrier recombination near the front surface. The effect of detrimental absorption in the metal can be seen for the IQE with the metal absorption (grey line). To estimate the effect of a standard SiN AR coating on the optical response of the solar cell, the EQE was calculated taking into account the simulated reflection of Figure 3.4(a) (violet dashed line).

The measurements and simulations in Figure 3.4(a) show that the nanowire network only adds a small amount of additional reflection, the value increases from 33% for a bare silicon surface to 36%. For this sample we measured a J_{sc} of 23 mA/cm^2 (see Figure 3.4(a) and 3.4(c)). A standard 80 nm AR coating (n = 2) can reduce the reflection of the flat nanowire network silicon surface to ~ 9 %, which would result in a short-circuit current density of ~ 33 mA/cm^2 (see Figure 3.4(c)).
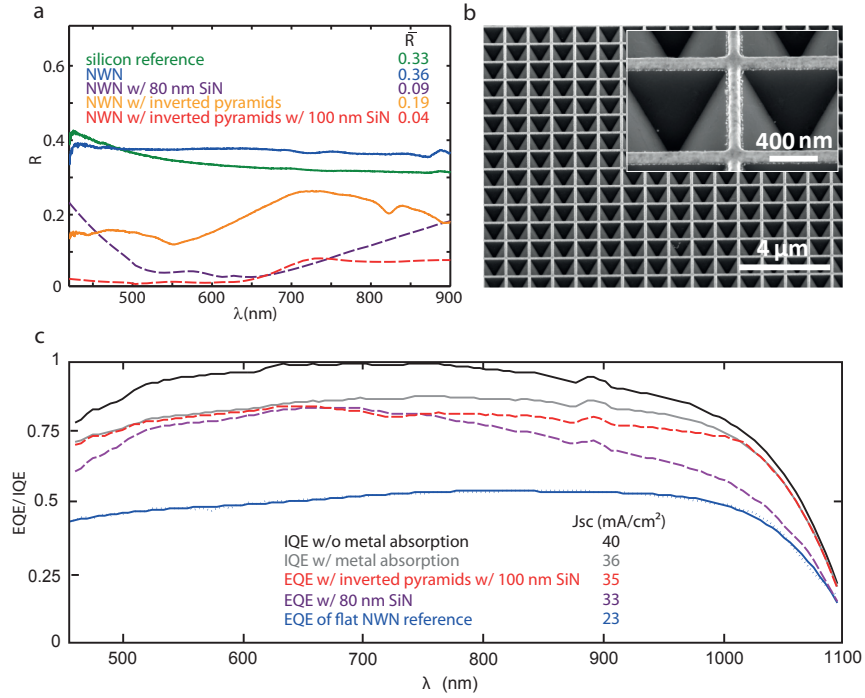
Figure 3.4: Reflection, EQE, IQE and inverted nanopyramids. (a) Reflection measurements (solid lines) of silicon reference wafer (green), a solar cell with a metal nanowire network (NWN) with a pitch of 1 μm and a nanowire width of 100 nm (blue) and a sample with integrated inverted nanopyramids between the metal nanowires (orange). Also shown are the simulated reflection values (dashed lines) of the flat metal network with 80 nm SiN coating for a wire width of 100 nm (violet) and the integrated inverted nanopyramid metal nanowire structure with 100 nm SiN coating on top of 50 nm wide wires (red). The average reflection values between 420 - 900 nm are listed next to the legend. (b) Scanning electron microscopy image of a metal nanowire network with integrated inverted nanopyramids. A high-resolution SEM is shown as an inset. (c) External quantum efficiency (EQE) of solar cell with metal nanowire network (blue). The IQE was determined by accounting for the reflection (blue line in (a)) and the simulated absorption of the metal network. The simulated reflection curves in (a) for the SiN coating (violet) and the integrated nanopyramid nanowire structure (red) were used to estimate the effect on the EQE of the final device. The respective short-circuit current densities are depicted next to the legend.

The measured J_{sc} of 23 mA/cm^2 (see Figure 3.2(a) was obtained for a MIS solar cell with a bare nanowire network silicon surface with an average reflection of 36%. Therefore, the photocurrent density after subtracting the reflection losses amounts to 36 mA/cm^2 (grey curve in Figure 3.4(c), which shows that a large fraction of the photogenerated charges is collected. However, since it does not reach the maximum photocurrent density under 1 sun illumination for silicon ($\sim$ 44 mA/cm^2), we conclude that other loss mechanisms must be present, which are discussed below.

Figure 3.11 shows the simulated reflection, transmission and absorption values for a metal nanowire network with the dimensions mentioned above on a flat silicon wafer. As can be seen, the averaged absorption amounts to $\sim$ 10% in the 420 - 900 nm spectral range. Therefore, we conclude, that the short-circuit current density is partly lowered due to absorption in the metal by approximately 4 mA/cm^2 to the value of 36 mA/cm^2 (black curve in Figure 3.4(c)). A potentially detrimental influence of the tunnel junction, which could result in nonlinear current-voltage behavior, was ruled out by measurements of the J_{sc} under different illumination intensities, which prove that the 1 nm Al$_2$O$_3$ has a negligible tunnel resistance under normal operation conditions (see Figure 3.12).[120] Previous research has shown that the insulator thickness for MIS type solar cells should not exceed 2 nm to limit the tunnel resistance.[87, 88] Another origin of the photocurrent loss can be related to fabrication-induced defect formation. After the fabrication of the metal nanowire networks we encounter strongly s-shaped I-V curves, which can be attributed to charge carrier extraction barriers at the contact-silicon interfaces.[77] We anneal our samples until the s-shape is completely removed. We ascribe the damage mostly to the electron beam exposure of the a-Si:H.[119] With increasing annealing temperatures, the I_{sc} (and FF) of the solar cells is monotonically increasing. However, the V_{oc} reaches its maximum at around 220 - 230 °C, after which it starts to decrease. Therefore, we chose the annealing temperature not to exceed 220 °C, recovering the maximum V_{oc}, while being aware of the non-optimized I_{sc} (and FF) values, due to residual fabrication induced defects. For further explanation, see the Figure 3.13. The IQE (black curve) in Figure 3.4(c) shows a decrease in IQE for short wavelength until it reaches $\sim$ 0.8. This supports our assumption as light in the short wavelengths range is absorbed close to the surface, where the fabrication induced defects must be located. Therefore, the annealing behavior and the absorption in the metal nanowire network discussed above can explain the main difference between the J_{sc} of our solar cells (36 mA/cm^2, after reflection) and a J_{sc} of 42 mA/cm^2, which is reached by highly efficient silicon solar cells. We note that other losses, such as parasitic absorption in the thin a-Si:H layer, are likely to be present.[121]

As a first step towards improved J_{sc} values for nanostructured MIS solar cells, we fabricate inverted nanopyramids integrated in between the metal nanowire network. Bare inverted nanopyramids with optimized pitch and additional AR coating have shown outstanding optical performance.[122, 123] Furthermore, etch resistant metals, such as the ones employed for our metal nanowire network, are frequently used as masking layers in micro-and nanofabrication.[124, 125] Figure 3.4(b) shows a scanning electron microscopy (SEM) image (magnified in the inset) of the fabricated inverted nanopyramid nanowire network structure. The measured reflection of the network with inverted pyramids (Figure 3.4(a), solid yellow line) shows clear resonant features due to the diffraction modes created by the effective grating. The average reflectivity of 19% proves the strong decrease in reflection compared to the flat nanowire network surface. By simulating an additional AR coating of 100 nm on top of the nanopyramid structure and a nanowire width of

50 nm instead of 100 nm (Figure 3.4(a), dashed red line) we show that the residual reflection can be even further reduced to 4%, which is well below the optimized AR coating for a flat silicon nanowire network surface (9%) (solid violet line). Figure 3.4(c) shows the effect of the integrated nanopyramid texturing on the EQE (red dashed curve), which results in a J_{sc} of ~ 35 mA/cm^2. We stress that a further decrease in reflection with optimized dimensions, e.g. AR coating thickness and wire thickness, can be expected. However, the optimization of the non-trivial optical response, as well as the integration into the solar cell fabrication process of the metal nanowire network with integrated nanopyramids is beyond the scope of this report and focus of ongoing research.

3.4 Conclusions

We successfully apply metal nanowire networks to the MIS solar cell scheme. After correcting for the influence of the small size of the active area on the V_{oc} and the missing anti-reflection coating, our MIS solar cells exhibit a corrected power conversion efficiency of ~ 11 % with an effective V_{oc} of 560 mV and estimated J_{sc} of 33 mA/cm^2. We use EBIC measurements to show that the metal nanowire network homogenously extracts charge carriers via an inversion layer in the underlying silicon. Band diagram simulations allow us to investigate the dependence of the conduction type inversion on the work function difference between the metal and the semiconductor and indicate the occurrence of Fermi level pinning at a charge neutrality level at the metal dielectric interface. Reflection measurements show that a high metal coverage of the surface with metal nanowire networks only adds 3% of additional reflection compared to a flat silicon surface.

Finally, we demonstrate a first step towards improved device performance by using the metal nanowire network not only as a transparent electrode and for the inversion layer formation, but also as an etch mask for surface texturing. We fabricate inverted nanopyramids integrated into the metal nanowire network. This way we are able to decrease the reflectivity substantially from 36% to ~ 4%. We use external quantum efficiency (EQE) measurements to estimate the influence of the reduced reflection on the overall device performance and thereby point out a path towards MIS solar cells that exhibit both high V_{oc} and J_{sc} values. Furthermore, our work shows potential for the MIS concept to be used to directly contact well passivated, intrinsic semiconducting layers, which naturally show higher carrier lifetimes and mobilities and are therefore preferable for high efficiency solar cells. Finally, our results are not limited to silicon, but can be applied to many thin-film materials with small charge carrier diffusion lengths where the difficulty of doping makes carrier selective contact formation more challenging.

3.5 Supplemental information

3.5.1 Fabrication details

To isolate the effect of the metal nanowire network on the MIS solar cell performance, we are using a state-of-the-art contact scheme for the back of the solar cell, which is employed in industrial solar cells (see Figure 3.1). This half cell consists of a double side polished float zone silicon base wafer with low n-type doping (3 Ohmcm), followed by different layers which create the back contact; a thin-film of intrinsic hydrogenated amorphous silicon (a-Si:H) (5 nm) followed by a layer of highly doped n-type a-Si:H (8 nm) are grown on the silicon wafer by plasma enhanced chemical vapor deposition (PECVD, Roth & Rau). The n-type a-Si:H is contacted via a sputtered indium tin oxide (ITO) layer (80 nm), followed by a sputtered silver layer (300 nm) as metal contact (Roth & Rau AK tool system).

The passivating and insulating layer, which is grown on the front surface after a short HF treatment (45 s in 1%), consists of 3 nm intrinsic a-Si:H followed by 1 nm of Al_2O_3.[107] The a-Si:H is grown by inductively coupled plasma chemical vapor deposition (ICP-CVD, PlasmaLab System 100, Oxford Instruments) and is used due to the excellent chemical passivation properties on the silicon surface. An argon and silane flow of 20 sccm, a temperature of 50 °C and a power of 400 W at a pressure of 10 mTorr were used for 24 s (~ 3 nm thickness). The Al_2O_3 layer (9 cycles with a total nominal thickness of ~ 1 nm) is grown by atomic layer deposition (ALD) (OpAL, Oxford Instruments) at 190 °C with trimethylaluminum (TMA) and O_2 plasma. Al_2O_3 is known for its high stability and insulating properties. When used directly on silicon, ALD Al_2O_3 has been shown to exhibit a high fixed charge density, which can lead to a field effect passivation of the underlying surface.[108–111] Subsequently, the samples were exposed to N_2 atmosphere in a rapid thermal annealing oven at 190°C for 30 min.

The passivated and back contacted half cells were fabricated on 4 inch wafers, which were subsequently cut into about 2-3 cm^2 small pieces to allow the optimization of the following fabrication steps.

The square metal network (nanowire width ~ 100 nm, network pitch ~ 1-2 μm) is fabricated by electron beam lithography (EBL) on small areas (2.4 - 4.5 mm^2) on ~ 2 cm^2 substrates. EBL resist ZEP 520 A (Zeonrex Electronic Chemicals) is used in a 2:1 mixture with anisole and spun (1000 rpm for 40 s) to achieve a resist thickness of ~ 200 nm. Afterwards, the substrates are baked at 180 °C for 5 min. The resist is exposed with 30 kV beam acceleration at a dose of 400 μC/cm^2 (10 μm aperture) in a fixed beam-moving stage modus (FBMS), with a predefined square nanowire network structure with pitches of 1 μm and 2 μm. After developing in pentylacetate for 1 min the samples are rinsed for 15 s in a 9:1 mixture of methyl isobutyl ketone (MIBK) and isopropanol (IPA) and additionally for 15 s in pure IPA.

The samples are blow-dried with nitrogen and transferred to the vacuum chamber of an electron beam evaporator. At a pressure of ~ 5×10^{-7} mbar, first a 10 nm thin layer of palladium, followed by a 40 nm thin layer of gold are evaporated at a

rate of 0.2 - 0.5 Å/s from water-cooled copper and tungsten crucibles, respectively. The Pd and the Au pellets are of at least 99.95% purity. This double structure is used because of the higher work function (WF) of Pd (5.2 - 5.6 eV) than Au (5.1 - 5.5 eV), which allows a stronger inversion in the underlying silicon, and the lower optical losses of Au compared to Pd.

After the evaporation, the samples are immersed in warm acetone (50 °C) to dissolve the EBL resist and this way lift-off the redundant metal film, leaving behind the desired square metal nanowire network structure. Metal pads for later contacting purposes are placed on two sides of the square network with conventional UV lithography and subsequent metal evaporation, using a 100 nm, opaque Au layer.

Electron beam (e-beam) and intense UV light exposure is known to cause damage in a-Si:H. Therefore, the samples are subsequently transferred into a vacuum oven and annealed for 60 min at a pressure of $5x10^{-5}$ mbar and a temperature of 220 °C to reverse the majority of the damage (see Figure 3.13).

The integrated inverted nanopyramids in between the metal nanowire network were fabricated by first fabricating the metal nanowire network on a simple silicon wafer and subsequently immersing the sample into KOH etching solution (30%) for 2 min. at a temperature of 20 °C. The metal (Pd/Au) nanowire network acts as an etching mask for the KOH solution and allows therefore the crystal plane selective dissolution of silicon, with the (111) crystal plane having the slowest etch rate.

3.5.2 Electrical and optical characterization

The J-V traces of the fabricated solar cells are measured under a solar simulator (Oriel SOL2 94062A (6X6) Class ABA, Newport) with the AM1.5G spectrum at 1 sun (100 mW/cm^2) illumination intensity, under masked conditions and at a temperature of 50 °C. The lamp intensity of the solar simulator is adjusted with a silicon reference cell. The right masking conditions are a crucial step for our solar cells, as the network only covers a small part (2 - 4.5 mm^2) of the passivated silicon half cells (2-3 cm^2 small substrates) (see Figure 3.5). Electrical probes are used to contact the front pad of the nanowire network and the back contact of the whole substrate with a source measure unit (Agilent B2910). The voltage is scanned with a positive and negative scan rate between -1V and 1V in 2001 steps while the current is being measured. No pronounced hysteresis or instability could be detected during the course of the measurements.

A lifetime of 1 ms was measured on the back contacted (w/o ITO) and front passivated silicon wafers before the nanowire network fabrication with a Sinton WCT-120TS lifetime tester.

The reflection measurements are performed using an integrating sphere setup. A supercontinuum white light source (Fianium) is used to illuminate the solar cells. The unpolarized light is weakly focused on the back plane of the sphere (4 inch Labsphere) to ensure near to normal incidence. A 105 μm core fiber is used to collect the reflected light and send it to a spectrometer, consisting of a spectrograph (Spectrapro 2300i) and a Si CCD array (PIXIS 400 CCD, cooled to -70 °C). The

measurements cover the 420 - 970 nm spectral range, and a 400 ms integration time with 50 accumulations were used.

3.5.3   Simulations

The band diagram simulations are performed with the software package AFORS-HET.[126] The simulated structure consists of an n-type Si wafer with a base doping of 1.6×10^{15} cm^{-3}, a 3 nm intrinsic a-Si:H layer, a 1 nm Al$_2$O$_3$ layer and a metal contact which is simulated by having a fixed work function as boundary condition. Fixed charge is placed at the a-Si:H/Al$_2$O$_3$ interface. For the material properties, the default simulation values provided by AFORS-HET are used. Simulations are performed in the dark.

The finite difference time domain (FDTD) simulations are performed with the software package Lumerical to obtain the reflection values for the 80 nm silicon nitride coated (n = 2) network with and without integrated inverted nanopyramids. The network has a pitch of 1 μm, a nanowire width of 100 nm (50 nm for red data in Fig. 3.4) and a thickness of 50 nm, with 40 nm of Au (top) and 10 nm Pd (bottom). A plane wave (λ = 400 - 1100 nm) under normal incidence and a power monitor, positioned above the nanowire network, are used to determine the reflectance. A perfectly matched layer as boundary condition in vertical direction is used to prevent scattering artifacts from the edges of the simulation box, while periodic boundary conditions are used for the in-plane dimensions to simulate an infinite network. The mesh size was 2 nm and the optical constants for Au, Pd and Si are taken from Palik.

3.5.4   Influence of active area size

In the following, we investigate the effect of the small size (2.4 - 4.5 mm^2) of the illuminated area on the open-circuit voltage. The illuminated area equals the area
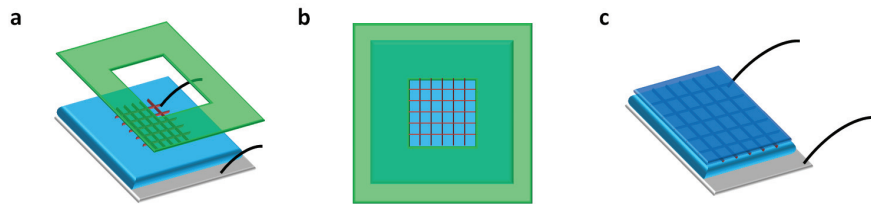
Figure 3.5: Infuence of masking condition.   (a), (b) The measurements under illumination are done with a mask (green), which covers the areas of the passivated and back contacted silicon substrate (blue). The mask has an opening in the middle, which allows illumination of the area with the fabricated metal nanowire network (red). (c) The measured V_{oc} is strongly affected by the relatively larger contribution of J_0 compared to J_L. Therefore, the effect is investigated and an effective V_{oc} derived, which allows the estimation of the solar cell performance, for which the substrate has the same size as the active area, as depicted here.

of the nanowire network, which has been limited in size due to the use of e-beam lithography. Taking into account that J_0 stems from a much larger region than the photocurrent, we are able to estimate the open-circuit voltage for a 1 cm^2 sample. This way we are able to evaluate and compare our results with regard to other solar cell device architectures.

We use two approaches, based on two separate sets of measurements, that both yield the same result for the estimated V_{oc}. The first approach investigates the scaling behavior of the recombination parameter J_0 with different sample sizes.

The second approach studies the variation of the V_{oc} for two different measurements; under masked and under unmasked conditions. This second approach makes use of the fact that the V_{oc} can be related to the carrier concentration inside the solar cell (implied V_{oc}).[19]

Because we employ high-purity monocrystalline FZ-silicon wafers we attribute the main contribution to J_0 to stem from recombination active surface sites. This surface recombination originates mostly from a larger area than the illuminated one. It is facilitated via diffusion of carriers to unilluminated regions and further to respective recombination sites. The diffusion is therefore taking place because of the difference in the carrier concentrations between the illuminated and the dark regions and between the recombination inactive bulk and recombination active surface.

Scaling behavior of J$_0$ with active area size

We compare three samples (S1-S3) that are fabricated in the exact same way but with different sizes of the metal nanowire network (2.4 - 4.5 mm^2) . The short-circuit current density for 1 sun illumination is approximately the same for all the fabricated samples which strongly supports the reproducibility of our fabrication scheme.

J_0 mainly originates from surface recombination. However, the exact size of the surface area which causes J_0 is unknown. Under illumination, the diffusion
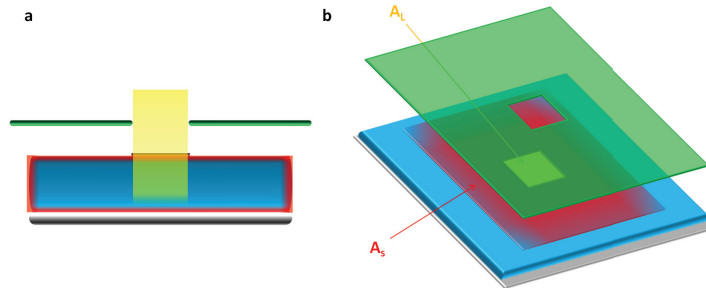
Figure 3.6: Origin of large recombination current. (a) The main contribution to J_0 is originating from surface recombination, as derived and described in the text. (b) The illuminated area A$_L$ is much smaller than the area A$_S$, which significantly contributes to the recombination current density J_0.

of photo-generated charge carriers to recombination active surface sites has to be taken into account and hence forbids any simple estimation of the contribution of any single dimension or region (e.g. the whole substrate area). Nonetheless, by using three samples, that have been fabricated under the exact same conditions, but are of different size, and investigating the scaling behavior of the recombination current density J_0, we are able to estimate the value of J_0 for a standardized sample size of 1 cm^2.

The ideal diode equation results in the well-known V_{oc} equation:

$$V_{oc} = \frac{n \times k_B T}{q} \times ln\left(\frac{J_L}{J_0} + 1\right) \sim \frac{n \times k_B T}{q} \times ln\left(\frac{J_L}{J_0}\right) \tag{3.1}$$

with the ideality factor n, the Boltzmann constant K, temperature T, the elementary charge q, the photocurrent density J_L and the recombination current density J_0.

In the following, we assume an ideality factor of n = 1, but this assumption has no influence of the scaling of J_0. Using the above equation, we calculate the recombination parameter J_0 for the three samples under illumination. The temperature during the measurements was ∼ 50 °C (323 K) and the respective measured V_{oc} and J_{sc} values are listed in Table 3.1:

$$J_0 = exp\left(-\frac{V_{oc}}{27.8\ mV} \times J_L\right) \tag{3.2}$$

$$J_0^{S1} = 6.60 \times 10^{-9} A/cm^2,\ J_0^{S2} = 2.90 \times 10^{-9} A/cm^2,\ J_0^{S3} = 1.68 \times 10^{-9} A/cm^2.$$

In general, J_0^{tot} can be expressed as the sum of the different recombination processes:[127]

$$J_0^{Tot} = J_0^{Surf} + J_0^{SRH} + J_0^{Aug} + J_0^{Rad}. \tag{3.3}$$

J_0^{Surf} stems from surface recombination, J_0^{SRH} from Shockley-Read-Hall (SRH) recombination, J_0^{Aug} from Auger recombination and J_0^{Rad} from radiative/ band-to-band recombination. Often, J_0^{Tot} is also separated according to the different regions in the solar cell from which the respective J_0 originates (e.g. for a n$^-$-emitter). As

Sample	Area [mm^2]	V_{oc} [mV]	J_{sc} [mA/cm^2]	J_0 [A/cm^2]
S1	2.4	419 (M)	23.2 (M)	$660x10^{-11}$ (C)
S2	3	439 (M)	21.0 (M)	$290x10^{-11}$ (C)
S3	4.5	457 (M)	23.3 (M)	$168x10^{-11}$ (C)
S_{a-1}	100	**562** (C)	23.2 (E)	$3.97x10^{-11}$ (F)

Table 3.1: Solar cell parameters for differently sized samples. Measured (M), calculated (C), estimated (E) and fitted (F) solar cell parameters of the small area samples S1-S3 and the estimated 1 cm^2 sample S_{a-1}

mentioned above, we expect the main contributor to be J_0^{Surf} due to the absence of highly doped regions and the high crystal quality of the FZ-silicon base wafer.

For our small samples we expect approximately a $1/A_i$ dependence for the J_0, especially with increasing area size up to 1 cm^2. The total recombination current can be approximated as a constant that originates from a much larger area (for surface recombination) or volume (for SRH and Auger):

$$J_0^{S_i}(A_i) = I_0^{Tot}. \tag{3.4}$$

For increasing area size, but with $A_i < 1$ cm^2, J_0 approaches more accurately a value that represents the recombination originating from a 1 cm^2 sample. However, for the measured samples we expect a deviation from the $1/A$ dependency, due to the nature of our samples. As we show in Figure 3.13, we observe electron beam-induced damage in the top 3 nm a-Si:H layer which can mostly be removed with a post fabrication anneal. However, as we discuss below, we are not able to remove all the induced damage. We choose an annealing temperature that is optimized with regard to the V_{oc}, but we cannot prove that this maximum V_{oc} is completely unaffected by the damage. As a result, we expect a slightly higher J_0 for the fabricated samples, than a simple $1/A$ dependency would suggest. However, even for those samples the major J_0 contribution will stem from a much larger area than the illuminated one, unrelated to the electron beam-induced degradation.

Because of those reasons, we use a least squares fit method, to fit an equation of the following form to our calculated J_0 values:

$$f(x) = \frac{p}{x + q} \tag{3.5}$$
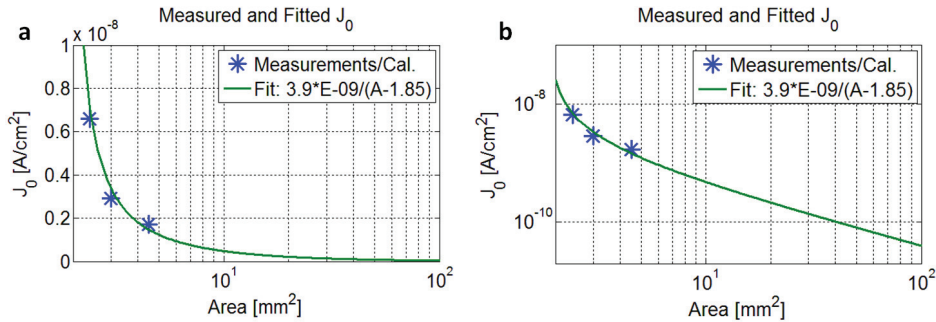
Figure 3.7: Calculated and fitted recombination current densities. Calculated J_0 values for fabricated small area samples (blue markers) as a function of the area size. Due to reasons described in the text, the J_0 dependency on the area size was fitted with the function $3.9 \times 10^{-09}/(A-1.85)$ (green line). The left and the right graph show the same data, however on semi-log and log-log plots.

As shown in Fig. 3.7, we obtain good agreement with $p = 3.90 \times 10^{-09}$ and $q = -1.85$:

$$J_0^{S_x} \sim \frac{3.90 \times 10^{-9}}{A_x - 1.85} A/cm^2 \tag{3.6}$$

Therefore, we can estimate the recombination parameter $J_0^{S_a}$ for a 1 cm^2 large sample:

$$J_0^{S_a} = 3.97 \times 10^{-11} A/cm^2 \tag{3.7}$$

Finally, we can calculate the V_{oc} of the 1 cm^2 sample S$_a$, assuming a short-circuit current density as observed for samples S1 and S3, i.e. ~ 23.2 mA/cm^2. As discussed above, setting the ideality factor to $n = 1$ does not influence our result, as the estimated $J_0^{S_a}$ would have been higher for $2 > n > 1$.

$$V_{oc}^{S_a} \sim n \times 27.8mV \times ln\left(\frac{J_L^{S_a}}{J_0^{S_a}}\right) \tag{3.8}$$

$$\boldsymbol{V_{oc}^{S_a} \sim 562mV}\,(n = 1,\ J_L^{S_a} = J_L^{S_1}) \tag{3.9}$$

**Influence of masking conditions on carrier concentrations**

The second approach makes use of the fact, that the V_{oc} is related to the carrier concentrations:[19]

$$V_{oc}^{imp} = k_B T \times ln\left(\frac{(N_A + \Delta n)\Delta n}{n_i^2}\right) \tag{3.10}$$

N_A is the doping concentration, Δn is the excess and n_i the intrinsic carrier concentration. V_{oc}^{imp} is the implied open-circuit voltage, because it can be seen as the V_{oc} that is implied by the carrier concentrations inside the semiconductor. For the actual V_{oc} the energy levels of the contacts for the charge carrier extraction have to be considered, as well. By comparing measurements under illumination of a masked and an unmasked sample we can show that the carrier concentration for the masked sample is the limiting case. The energy levels of the contacts, determined by the metal WF for the (MIS) hole contact and the a-Si:H n-type doping for the electron contact, allow for a substantially higher V_{oc}.

As shown in Figure 3.8, the lateral diffusive currents lead to a decrease in the carrier concentrations in the small illuminated region. This decrease directly results in a decrease in the quasi-Fermi level splitting, i.e. the V_{oc}^{imp}. In other words, the carrier concentration is reduced compared to a case of complete substrate illumination. For the latter, only gradients in the carrier concentrations due to the surface recombination exist. However, the interpretation of an unmasked measurement for which the complete substrate is illuminated has to be done with caution.

First of all, only a small part of the area that is illuminated is also patterned with the nanowire network. The optical properties of the flat metal nanowire network on top of silicon are very similar to a flat bare silicon substrate, i.e. 36 vs. 33 %
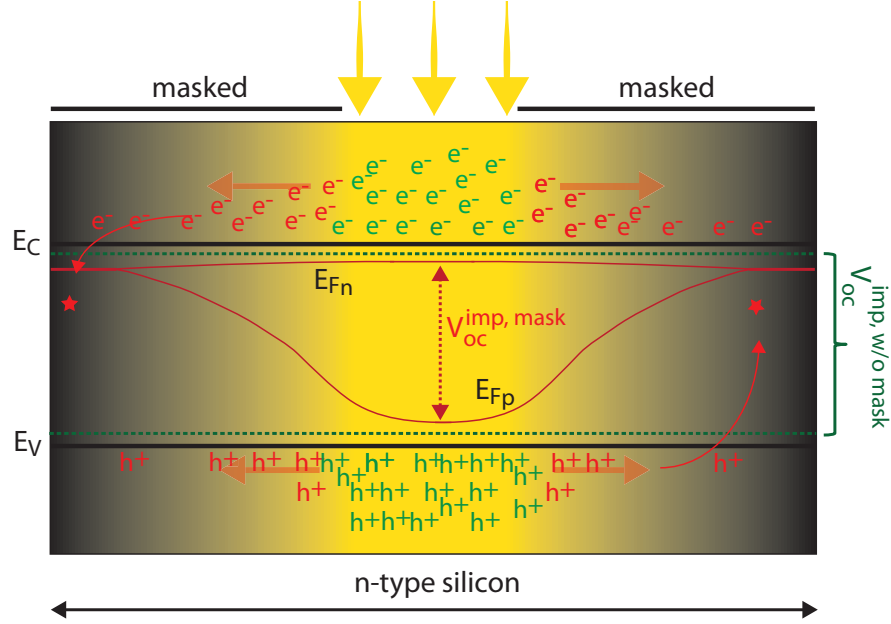
Figure 3.8: Schematic band diagram with lateral diffusion. Differences in carrier concentrations between the illuminated and the dark regions inside the bulk n-type wafer lead to gradients in the quasi-Fermi levels. Those in turn result in diffusive transport (red arrows) away from the illuminated region. The result is a lower implied V_{oc}.

reflection, and 10 % additional absorption, as shown in Figure 3.4. However, because of the logarithmic dependence of the V_{oc} on the I_{sc}, the overestimation can be neglected. Therefore, the V_{oc}-loss due to lateral diffusion, ΔV_{oc}^{diff}, is given by:

$$\Delta V_{oc}^{diff} = V_{oc}^{S_1 nomask} - V_{oc}^{S_1 mask} - V_{oc}^{S_1 optical} \sim 100 mV \qquad (3.11)$$

$\Delta V_{oc}^{S_1 optical}$ is the V_{oc}-overestimation due to the lower reflection of the bare silicon surface and the absence of metal absorption. However, as we argued above, $V_{oc}^{S_1 optical} \sim 0\ mV$. V_{oc}^{nomask} and V_{oc}^{mask} are the open-circuit voltages of the unmasked and masked samples, respectively.

Furthermore, the I_{sc} of the unmasked sample is substantially higher than for the masked sample, especially for high purity silicon with its large minority carrier diffusion lengths. However, it does not reach the I_{sc} values predicted for a 1 cm^2 sample, i.e. 23 mA. For our measurement the unmasked I_{sc} is about 10 times higher than the masked one, i.e. 5.58 mA vs. 0.557 mA, as shown in Table 3.2. Therefore, we can estimate the area to be roughly 10 times larger than the 2.4 mm^2 small sample (neglecting the slightly different optical properties). Furthermore, the recombination current I_0 for a 24 mm^2 area is close to the value for a 100 mm^2 area (see also the extensive discussion above). Hence, we can estimate the additional gain in V_{oc}

Sample	Area [mm^2]	V_{oc} [mV]	I_{sc} [mA]	I $-$ Factor	I_0
S_1^m (*masked*)	2.4	419	0.557	$-$	
S_1^{unm} (*unmasked*)	~ 24 (*unknown*)	519	5.580	1	$I_0^{S_1^{unm}}$
S_{a-2}	100	**559** (*C*)	23.3 (*E*)	4.17	$I_0^{S_{x2}} \sim I_0^{S_1^{unm}}$

Table 3.2: Measured solar cell paramters with and without mask. Measured solar cell parameters of the small area sample S1 with and without a shadow mask. Calculated (C) and estimated (E) parameters for the 1 cm^2 sample S_{a-2}

for a 100 mm^2 sample due to an increase of I_{sc} to 23 mA, with the term ΔV_{oc}^{light}.

$$\Delta V_{oc}^{light} = 27.8mV \times ln(4.17) \approx 40mV \tag{3.12}$$

We note, that this approximation leads to a conservative estimate of the additional V_{oc}-gain because we use an I_0 that stems from a 100 mm^2 sized sample. Another deviation is expected due to the less efficient carrier extraction in the case of the unmasked sample which heavily impacts the resistance and hence fill factor of the unmasked solar cells. The current of 5.58 mA of the unmasked sample is separated and collected with the same inversion layer and metal nanowire network than the 0.557 mA of the masked sample. Nonetheless, we can estimate the V_{oc} for a 1 cm^2 sample:

$$\Delta V_{oc}^{S_{x2}} = V_{oc}^{S_1^m} + \Delta V_{oc}^{light} \left(I_0^{S_{x2}} \sim I_0^{S_1^{unm}} \right) + \Delta V_{oc}^{diff} = 559mV \tag{3.13}$$

Comparing the scaling behavior of the J_0 and the variation of the V_{oc} for different masking conditions shows close agreement for the V_{oc} of a 1 cm^2 sample:

$$V_{oc}^{S_{a-1}} = 559mV \sim V_{oc}^{S_{a-2}} = 562mV \tag{3.14}$$

3.5.5 Band diagram simulations

Influence of work function

Figure 3.9 shows the results of band diagram simulations, which are performed to investigate the influence of different metal work functions (WF) on the inversion of the n-type silicon. For the chosen WFs between 4.6 - 5.6 eV the conduction bands (E_C) and the valence bands (E_V) are plotted. All the Fermi levels (E_F) are set to 0 eV for clarity. The metal next to the adjacent Al$_2$O$_3$ is not shown. As can be seen, the WF of the metal determines the extent of the conduction type inversion in the semiconductor. N-type silicon has a WF of around 4.2 eV, hence employing metals with higher WFs reduces the free electron concentration in the n-type silicon, even leading to strong conduction type inversion in the extreme case. For comparison,
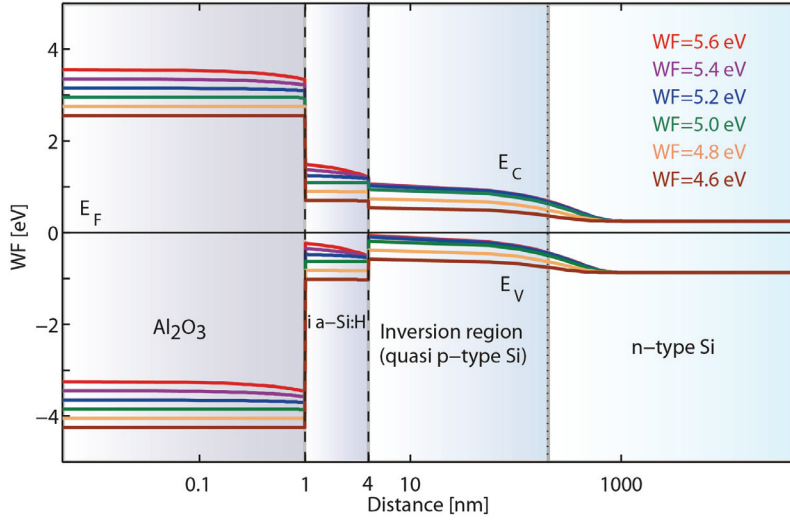
Figure 3.9: Band diagram simulations for the metal work function influence.
Band diagram simulations showing the influence of the metal work function for
the conduction type inversion in silicon. The conduction bands (E_C) are plotted in
the upper half (E>0 eV) and the valence bands (E_V) in the lower half of the figure
(E<0 eV). For a better overview all the Fermi levels (E_F) are set to 0 eV.

silicon that is strongly p-type doped (p^+) has a WF of around 5.3 eV. The simulations
show that for WFs between 4.6 - 5.2 eV, an increase in the WF leads to increased
inversion. Above ~ 5.2 eV on the other hand, the additional inversion with increas-
ing metal WF becomes less pronounced. Besides the logarithmic dependence of
the Fermi level position, part of this decreasing sensitivity of the inversion with
increasing WF can be ascribed to the intrinsic (low conductivity) a-Si:H. Between
5.2 - 5.6 eV the initial energy difference of the conduction bands (red, violet and
blue lines) at the metal - a-Si:H interface falls off over the intrinsic a-Si:H.

In the simulations shown here, no additional fixed charge density (Q_f) of the
Al_2O_3 at the metal - a-Si:H interface is assumed. As shown in Figure 3.10, and
discussed in detail below, only an additional fixed charge density with very high
(negative) Q_f values of around 10^{13} cm^{-2} has a substantial effect for high WF met-
als. For low WF metals (<5 eV) Q_f values above 10^{12} cm^{-2} can already substantially
improve the inversion.

Influence of fixed charged density

Al_2O_3 is known to exhibit a fixed charge density at a Al_2O_3-silicon interface, which
can lead to electrical passivation of the interface, by repelling minority carriers with
the same polarity of the surface charge. This so called field-effect passivation is
being used in solar cells to increase the lifetime of the minority carriers by pre-
venting their diffusion towards recombination active surface/interface sides. For
the tunnel and passivation layer employed in this work, consisting of a 1 nm Al_2O_3
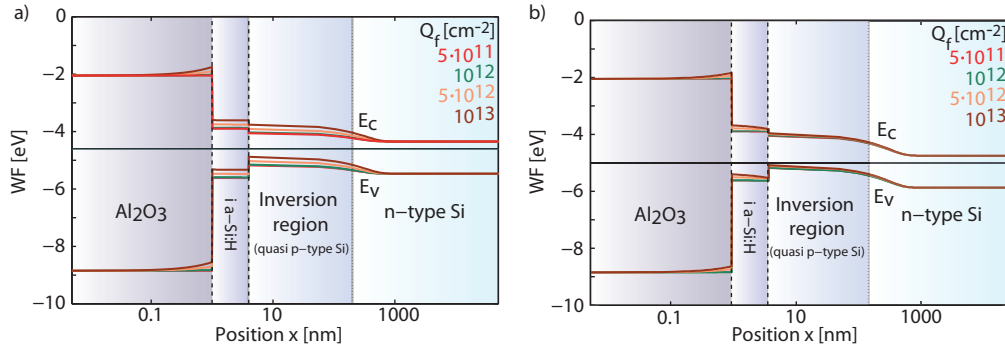
Figure 3.10: Band diagram simulations for the influence of a fixed charged density. Band diagram simulations showing the influence of a fixed charge density in the Al_2O_3 at a given the metal work function (WF) for the conduction type inversion in the silicon. The conduction bands (E_C), the valence bands (E_V) and the Fermi levels (E_F) are indicated, as well as the boundary regions in between the different employed layers. The metal, positioned left to the Al_2O_3, is not shown. (a) Conduction type inversion for a metal work function of 4.6 eV and a fixed charge density Q_f between 0 cm^{-2} - 10^{13} cm^{-2}. (b) The same as in (a), but with a metal work function of 5 eV.

and a 3 nm a-Si:H layer, the occurance of a fixed charge density is being debated at the moment. Therefore, we performed band diagram simulations to investigate the effect of a potential fixed charge density on the magnitude of the inversion layer. In principle, a fixed charge density could lead to a stronger inversion in MIS type solar cells than given by the difference in work function between the metal and the adjacent semiconductor. Figure 3.10 shows the magnitude of the conduction type inversion for a metal work function of 4.6 eV (3.10(a)) and 5 eV (3.10(b)) in dependence of a fixed charge density at the Al_2O_3/ a-Si:H interface. The interface charge density Q_f changes between 0 cm^{-2} and 10^{13} cm^{-2}. As can be seen in Figure 3.10(a), for a metal work function of 4.6 eV the additional fixed charge density can have a very strong effect on the magnitude of the inversion layer. However, as can be seen in Figure 3.10(b) for a higher metal work function of 5 eV, even without a fixed charge density the inversion already reaches the same magnitude than for a work function of 4.6 and a very high fixed charge density of 10^{13} cm^{-2}. Furthermore, any additional fixed charge density only has a relatively smaller effect on the conduction type inversion for a metal work function of 5 eV. This can be understood by the logarithmic dependence of the Fermi level position in the band gap with carrier concentration.

We conclude, that additional (negative) fixed charge density can lead to a stronger conduction type inversion (and hence higher V_{oc}), however the difference between the metal and the semiconductor work function has a more pronounced effect.

Explanation of the low open-circuit voltage

The simulations show that high metal work functions (> 5 eV) can lead to strong conduction type inversion in the underlying silicon, the prerequisite for a high V_{oc}. Conversely, any decrease of the effective metal WF will lead to a decrease in the V_{oc}. When corrected for the small illuminated area of our cells compared to the large substrate, the calculated effective V_{oc} is 560 mV. The WF of high purity Pd is reported to be in the range of 5.2 - 5.6 eV, with the exact value being crystal facet dependent.[128] Given our surface passivation scheme and the high purity of the FZ-silicon wafer, even a slightly lower work function of Pd due to trace amounts of impurities seems insufficient to explain our results (see Figure 3.9).

A cause for the relatively low V_{oc} , when compared to state-of-the-art silicon solar cells (>700 mV), can be the lowering of the Pd vacuum work function due to the presence of the dielectric Al_2O_3.[113] From developments in the field of complementary-metal-oxide-semiconductor (CMOS) transistors, it is known that Fermi level pinning to a charge neutrality level (CNL) in the dielectric can lower the effective work function of the metal.[113–115] As a result, the effective WF of Pd is lowered to the range of 4.6 - 4.9 eV by the dielectric Al_2O_3, which is well below the reference WF of highly doped p-type silicon (~ 5.2 eV). Therefore, other dielectrics, e.g. SiO_2, that cause much weaker Fermi level pinning to the CNL should be employed in future devices. However, when searching for alternatives the stability and passivation properties for ultrathin layers of 1-2 nm have to be kept in mind.

We note that a strong inversion in the underlying silicon is not the only factor to consider for high open-circuit voltages in MIS silicon solar cells. To exclude fabrication induced material degradation as a major cause for the low V_{oc}, lifetime measurements after each fabrication step would be highly desirable. Unfortunately, the specific process sequence (e.g. the initial fabrication of the metalized backside) does not allow to track the lifetime with the Sinton lifetime tester. Besides the observed electron beam-induced damage of the a-Si:H (Figure 3.13), other steps known to negatively impact the passivation were avoided.

Furthermore, the selectivity of the contacts will fundamentally determine the degree to which the implied open-circuit voltage (V_{oc}^{imp}) can be translated to the measured V_{oc}.[19, 90, 129, 130] While it is true that a stronger inversion leads to a higher selectivity, the latter might be limited for conduction type inversion in silicon compared to state-of-the-art diffused junction or SHJ solar cells. However, in the light of the open-circuit voltages obtained in the past for MIS silicon solar cells, which reached values of 655 mV with inferior passivation layers, we expect the main limiting factor for our solar cells to be the ones discussed above.[85, 129]

## 3.5.6 Optical FDTD simulations

Figure 3.11 show the simulated (FDTD) reflection, transmission and absorption values for a metal nanowire network. The network absorbs on average about 10% of the incident light across the visible wavelength range.
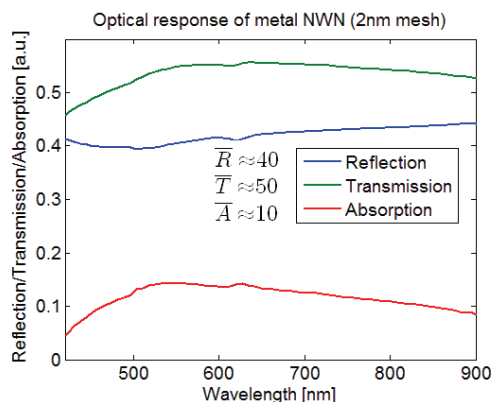
Figure 3.11: Simulated reflection, transmission and absorption. Simulated (FDTD) reflection, transmission and absorption values for metal nanowire network with a thickness of 50 nm (10 nm Pd, 40 nm Au), width of 100 nm, pitch of 1 μm.

3.5.7 Tunnel resistance

The resistance of the interfacial layer is non-linear in nature. For low intensities and insulator thicknesses below 1.5 - 2 nm, the I_{sc} is limited by the semiconductor; all charge carriers are extracted and only an increase in intensity can increase the current further. Tunneling resistance is insignificant in that region, as the rate of tunneling is relatively low. For larger insulator thicknesses or higher intensities, the device characteristics shift from a semiconductor-limited to a tunnel-limited regime.[120] Because we observe a linear increase of the I_{sc} and the efficiency throughout the investigated regime the contact resistance is not tunnel-limited.
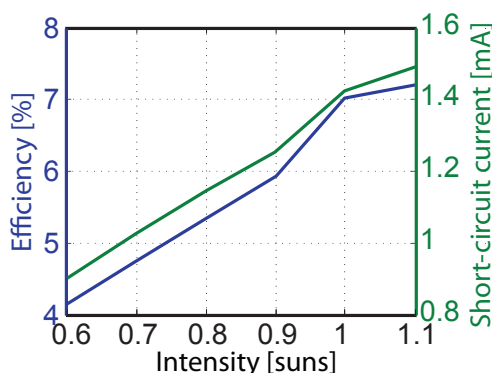
Figure 3.12: Efficiency and short-circuit current vs incident light intensity. The measurements show that the contact is not tunnel-limited under 1 sun illumination conditions.

3.5.8 Annealing behavior

After the fabrication of our samples we encounter s-shaped I-V curves (Fig. 3.13(b)), which indicate charge carrier extraction barriers at the interface. Electron beam exposure of a-Si:H is known to cause the defects in the material.[119] As shown by others, and confirmed with our performed annealing experiments, those defects can mostly be removed by annealing the a-Si:H at around 220 °C for 30 min. In that temperature range the s-shaped I-V curves disappear and the measured I_{sc} and V_{oc} values after each subsequent annealing step (see Figure 3.13(a) and (d)) improve substantially. We reach a maximum for the V_{oc} in the temperature range between 180 - 230 °C and an annealing time of around 30 min. However, the I_{sc} and with it the FF (not shown) do not reach a maximum but are monotonically increasing for the temperature and time range investigated. We choose to optimize the annealing conditions with respect to the V_{oc} to be able to make conclusions with respect to the extent of the inversion layer. We note that, while the I_{sc} and FF of our solar cells could be better, based on the annealing experiments, we cannot exclude the possibility that the V_{oc}-value of our cells is reaching a value that is affected by the electron beam-induced damage in the a-Si:H.
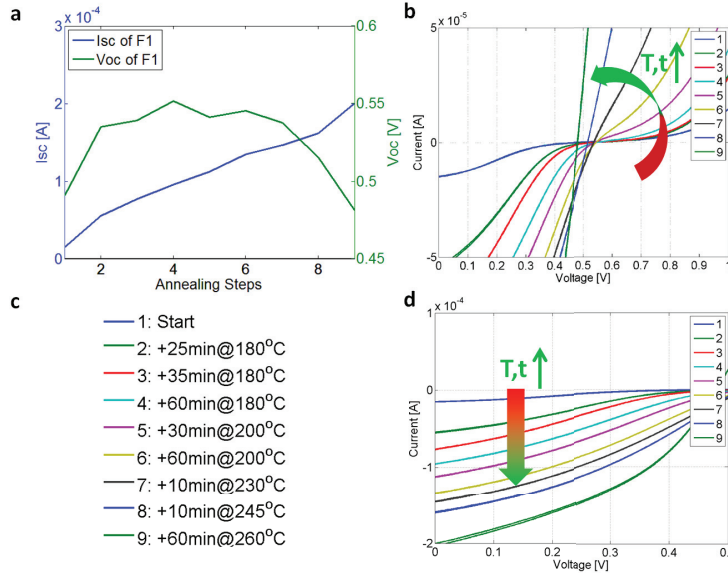
Figure 3.13: Annealing behavior. Influence of post-fabrication annealing steps on the I_{sc}, V_{oc} and charge carrier extraction barrier at the interface. The subsequent annealing steps are listed in (c). (a) The measured I_{sc} (blue) and V_{oc} (green) values as a function of the annealing step. As can be seen, the V_{oc} increases before reaching its maximum for an annealing temperature between 180 - 230 °C, and an annealing time of around 30 min. (b) With increasing annealing temperature and time the s-shaped IV curve disappears. (d) The I_{sc} increases monotonically without reaching a maximum in the range investigated.

4

Quantifying losses and thermodynamic limits in single InP nanowire photovoltaics

Nanowire array solar cells promise record performance by taking advantage of nanophotonic effects. Single nanowire devices facilitate studying these effects, but also render standard definitions of power conversion efficiency and external quantum efficiency meaningless, limiting characterization and understanding. Here we analyze a record InP single nanowire solar cell using intrinsic metrics to place its performance on an absolute thermodynamic scale. Determining these metrics requires novel integrating sphere microscopy, which combines spatially-resolved quantitative absorption, photocurrent, and photoluminescence measurements. We measure a photocurrent collection efficiency of >90% and a record open-circuit voltage (850 mV) that is 73% of the thermodynamic limit (1.16 V). Improving contact selectivity can increase the voltage to 85% of this limit, comparable to record Si and Cu(In,Ga)Se$_2$ planar solar cells.
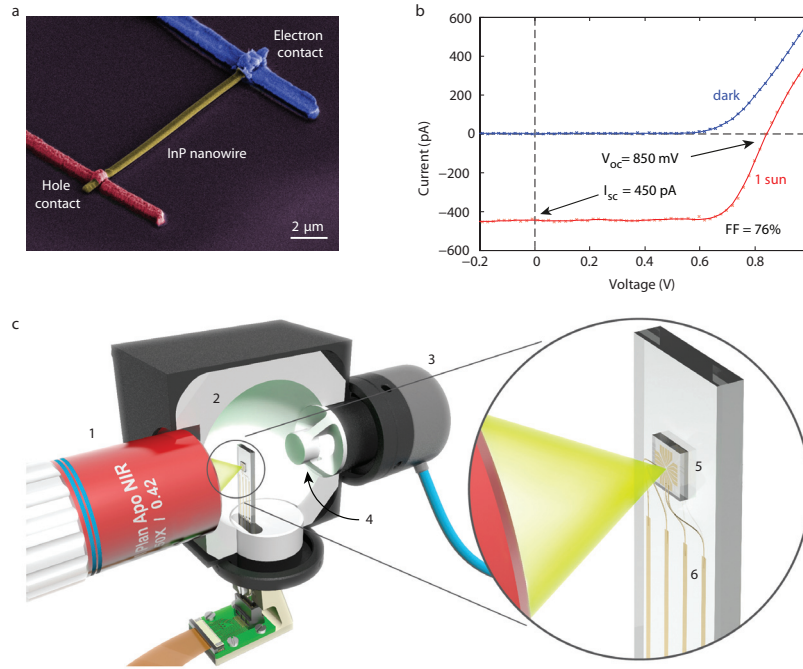
Figure 4.1: Characterization of a record single nanowire solar cell. (a) False-color SEM image of the InP nanowire device (yellow) with hole contact (red) and electron contact (blue). (b) The nanowire I-V curve in the dark (blue) and under the solar simulator at 1 sun intensity (red). The solid line is a smoothed fit to the data points (shown as small crosses). (c) A schematic depicting the integrating sphere microscopy setup. A microscope objective focuses light from a monochromated supercontinuum laser source on the nanowire solar cell inside the integrating sphere. The sphere collects transmitted as well as scattered light via a photodetector behind a baffle, while the objective directs the reflected light to another photodetector (not shown). Subtracting these calibrated signals from the input gives the local absorptance (fraction of incident light that is absorbed) with diffraction limited resolution. Photocurrent is measured simultaneously to determine the internal quantum efficiency (IQE). With a long-pass filter in front of the detector, photoluminescence can be collected quantitatively to give the photoluminescence quantum yield (PLQY). The sample is mounted on a piezoelectric stage, enabling spatial mapping of all these output parameters.

4.1   Introduction

Nanophotonic engineering holds great promise for photovoltaics: the record conversion efficiencies of nanowire solar cells are increasing rapidly, and the record open-circuit voltage has already surpassed the record planar equivalent.[14, 23] Furthermore, several authors have suggested that nanophotonic effects could help photovoltaics surpass the fundamental efficiency limits of planar solar cells.[131, 132] These effects are particularly pronounced in single nanowire devices, where two out of the three dimensions are subwavelength. They therefore provide an ideal platform to study how nanophotonics affects photovoltaics.[46, 49, 132–137]

However, in isolated nanophotonic systems the standard definition of power conversion efficiency no longer applies, because the device can absorb light from an area much larger than its own size. Additionally, while a thermodynamic bound on the photovoltage still exists, it is *a priori* unknown and may be very different from that of a planar solar cell. This complicates characterization of such nanoscale devices: it is unclear how well they perform with respect to fundamental limits and to other devices, how much can be gained through optimization, and whether the efficiency limits of planar devices can be surpassed by understanding and applying nanophotonics to photovoltaics.

Here, we analyze a record InP single nanowire solar cell using intrinsic metrics to place its performance on an absolute thermodynamic scale. Determining these metrics requires novel integrating sphere microscopy, which combines spatially resolved quantitative absorption, photocurrent, and photoluminescence measurements. We measure a photocurrent collection efficiency of >90% and a record open-circuit voltage (850 mV) that is 73% of the thermodynamic limit (1.16 V).

4.2 Results and discussion

In order to understand the fundamental limits and losses in nanophotonic solar cells and place their performance on an absolute thermodynamic scale, we study a record single nanowire solar cell. The device consists of a 310 nm diameter wurtzite InP nanowire with a 50 nm SiO_2 coating (Fig. 4.1(a)). It has a short-circuit current of I_{sc} = 450 pA, an open-circuit voltage of V_{oc} = 850 mV, and a fill factor of FF = 0.76 under AM1.5 solar spectrum illumination (Fig. 4.1(b)), all of which are excellent compared to previous nanowire devices. Using a novel characterization method, integrating sphere microscopy, we determine the spatially resolved absorptance (fraction of incident light absorbed), internal quantum efficiency (IQE, fraction of absorptance converted to current), and photoluminescence quantum yield (PLQY, fraction of absorptance converted to external photoluminescence) for the first time. Absorptance, IQE and PLQY directly quantify the three fundamental processes in solar energy conversion - charge carrier generation, collection and recombination, respectively - and therefore provide intrinsic performance metrics. We use these quantities to determine the fundamental thermodynamic limits, benchmark the performance against state-of-the-art technology, and pinpoint the remaining loss mechanisms. Although we focus on nanowire photovoltaics, these intrinsic metrics contain valuable information for any other nanophotonic optoelectronic device, and in particular nanoscale light-emitting diodes.

We begin our analysis of the nanowire solar cell by determining the absorptance and IQE. To date the primary experimental challenge in determining intrinsic performance metrics for single nanowire devices has been measuring quantitative absorption during solar cell operation, which is not possible with existing techniques. These methods assume that absorbed power is converted into heat (photothermal
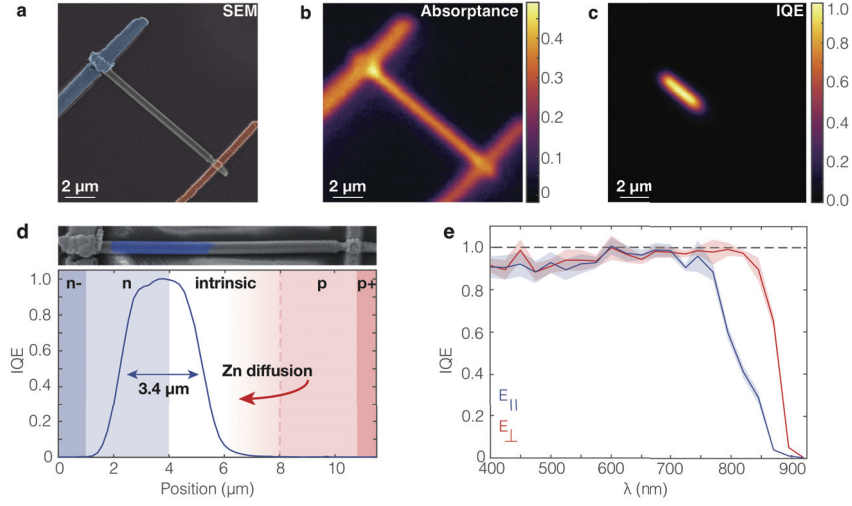
Figure 4.2: Internal quantum efficiency of a single nanowire photovoltaic. (a) False color scanning electron microscopy (SEM) image of the single nanowire device (InP nanowire diameter = 310 nm, length = 12.1 μm, SiO$_2$ shell thickness = 50 nm). The p-i-n doped InP nanowire device is visible in the center with an electron contact (blue) and hole contact (red). (b) and (c) Absorptance and internal quantum efficiency (IQE) as a function of position for the nanowire device. (d) The IQE as a function of position along the nanowire length, convoluted with the focused spot size (beam radius 730 nm). The color shading shows the nanowire doping profile as intended during nanowire growth. The SEM image on top has an electron beam-induced current (EBIC) measurement (blue shade) in good agreement with the IQE profile. (e) The peak IQE as a function of wavelength, which lies between 90% and 100% up to wavelengths close to the band gap, where the anisotropic nature of wurtzite InP becomes apparent. The shading displays the measurement uncertainty, which arises largely due to noise in the photodetectors.

spectroscopy[138–141]), that scattering does not occur (spatial modulation extinction spectroscopy[142–144]), or that the particle is an ideal dipole (scattered field interferometry[145]). Integrating sphere microscopy circumvents these assumptions by combining the standard tool for measuring absorptance of macroscopic samples[146] or ensembles of nanoparticles[147], with a long working distance microscope objective (see Fig. 4.1(c)). A photodetector placed behind a baffle on the integrating sphere collects scattered and transmitted light while the microscope objective collects reflected light (sent to another photodetector). Simply calibrating and subtracting these signals from the input gives the quantitative absorptance (see Section 4.3.6). The sample has current collecting leads and is mounted on a piezoelectric stage, which enables two-dimensional scans of the absorptance and IQE for the first time. The record InP nanowire solar cell used for integrating sphere microscopy characterization is shown in a false-color SEM image in Figure 4.2(a), with the n-type and p-type contacts in blue and red, respectively. Figure 4.2(b) and 4.2(c) show absorptance and IQE maps of the same nanowire device measured at
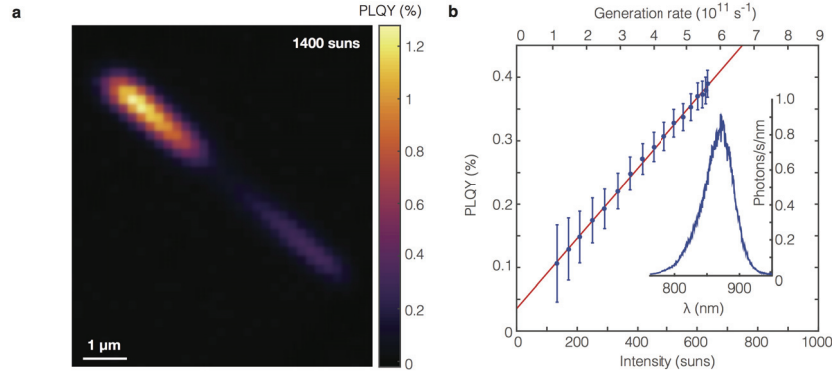
Figure 4.3: Photoluminescence quantum yield, power dependence, and recombination mechanism. (a) The photoluminescence quantum yield (PLQY) as a function of position, indicating that it peaks where IQE is highest (measured at 1400 suns to increase the signal to noise ratio). (b) To determine the PLQY at 1 sun intensity we measured it for a range of intensities lower than in panel (a). The PLQY clearly shows linear behavior with intensity, which indicates that Shockley-Read-Hall recombination dominates. The inset shows the nanowire photoluminescence (PL) spectrum at the brightest position in panel (a), also at 1400 suns. All PLQY measurements were performed with 600 nm excitation light parallel to the nanowire axis.

an excitation wavelength of 600 nm. The IQE reaches a peak value of 100% and is strongly localized to the upper half of the wire, as is more clearly visible in the line profile of the IQE along the nanowire in Fig. 4.2(d). The color shading in Fig. 4.2(d) shows the intended doping profile during growth. It should be noted that the p-type dopant zinc might have diffused further into the nanowire during growth as it is very mobile in InP at high concentrations.[148] Carrier collection is most efficient near the n-type/intrinsic interface, and collection occurs over a length of 3.4 microns. In the p-type region the IQE is essentially zero, indicating short electron diffusion lengths. This is confirmed by an electron beam-induced current (EBIC) measurement shown above the IQE line profile, from which we determine the electron diffusion length in the intrinsic/p-type segment to be 285 nm (see Section 4.3.5). The IQE is nearly independent of polarization and wavelength, with values >90% over the whole wavelength range up to the band gap (Fig. 4.2(e)). The small difference in band gap depending on excitation polarization is caused by the anisotropic nature of wurtzite InP and has previously been observed with photoluminescence excitation spectroscopy.[149]

With integrating sphere microscopy we can probe not only the IQE to understand the current collection efficiency, but also directly measure the PLQY. In absence of non-radiative recombination, PLQY=1 and the open-circuit voltage reaches the thermodynamic limit V_{oc}^{rad}. For a PLQY below 1, the V_{oc} is reduced from the radiative limit to the implied $V_{oc}^{imp} = V_{oc}^{rad} - V_T|ln(PLQY)|$, where V_T is the thermal voltage (25.9 mV). [150–152] Hence, the PLQY plays a crucial role in

understanding the photovoltage. To measure the PLQY, we place a filter in front
of the integrating sphere photodetector, such that only photoluminescence is
detected (see Section 4.3.7). Our spatially-resolved measurements show that the
nanowire PLQY peaks in the same region where the IQE is highest (Fig. 4.3(a)),
with an average PLQY over the active area of 0.9% at an excitation intensity of 1 μW
600 nm light ($\sim 10^3$ suns). To determine the average PLQY at 1 sun intensity, we
measure at a range of lower excitation powers (Fig. 4.3(b)). The PLQY decreases
linearly with excitation intensity, indicating that in this regime Shockley-Read-Hall
recombination dominates (see Section 4.3.7). Assuming linearity down to 1 sun
intensity, the average PLQY is 4×10^{-4} (0.040%). This value corresponds to a V_{oc}-loss
of 210 mV from the thermodynamic limit, and is comparable to what is observed
in world record planar crystalline Si, Cu(In,Ga)Se$_2$, and InP solar cells.[151]

The PLQY can provide the V_{oc}-loss from the thermodynamic bound V_{oc}^{rad}, but
in order to calculate the latter value for our device we must know the recombination
current corresponding to radiative thermal emission, I_0^{rad}. This emission current
together with the I_{sc} determines $V_{oc}^{rad} = V_T ln(I_{sc}/I_0^{rad})$.[150] In a macroscopic so-
lar cell, the I_{sc} and I_0^{rad} can be calculated by integrating the external quantum
efficiency (EQE, fraction of incident photons converted to current) over the solar
and blackbody spectra, respectively.[151] However, for single nanowire solar cells
the standard definition of EQE is not valid, because the absorption cross section
(σ_{abs}) can be much larger than the device area. To solve this important issue, we
define a new quantity called the collection cross section that takes on the same role:

$$\sigma_{EQE}(\lambda, \Omega) = \int IQE(\lambda, z) \, \sigma_{abs}^{1D}(\lambda, \Omega) dz \qquad (4.1)$$

where $IQE(\lambda, z)$ is the spatially resolved internal quantum efficiency (shown in
Fig. 4.2(e)) and $\sigma_{abs}^{1D}(\lambda, \Omega)$ is the effective absorption width of the nanowire (de-
termined from the absorptance, see Section 4.3.10). Fig. 4.4(a) shows σ_{EQE} for
the nanowire device studied here, in both polarizations. Note that σ_{EQE} requires
units of area, while the conventional EQE is a unitless quantum efficiency. This is a
crucial difference, because for macroscopic solar cells the area collecting photons
is independent of the incident wavelength and simply equal to the geometric area.
In contrast, for nanostructures the interaction area with the incident light can be
strongly wavelength dependent, e.g. due to resonances.[153] Additionally, in con-
trast to the IQE and PLQY, σ_{EQE} can be determined directly from the photocurrent
measurement, incident flux, and laser spot size (Section 4.3.10).

Integrating σ_{EQE} over the black body spectrum and all angles we find, which
leads to a maximum open-circuit voltage for our nanowire device (see Section
4.3.11). The difference between the ideal voltage (V_{oc}^{rad}) and the measured V_{oc} (850
mV) is 310 mV: the V_{oc} is 73% of the thermodynamic limit. The measured V_{oc} is
100 mV smaller than the implied open-circuit voltage V_{oc}^{imp} in the semiconductor
nanowire, suggesting that the contact selectivity plays a significant role in the V_{oc}-
loss. The V_{oc}^{rad} for this device is significantly higher than the Shockley-Queisser
V_{oc} for a planar cell with an absorption onset at 890 nm (like our nanowire device,
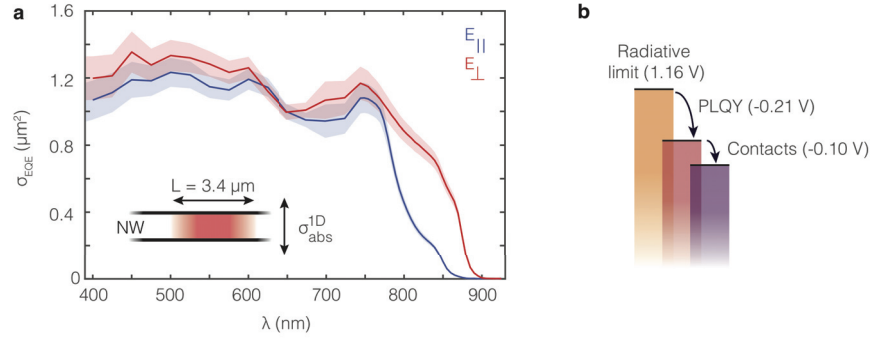
Figure 4.4: Measuring thermodynamic limits and quantifying loss mechanisms in single nanowire solar cells. (a) The collection cross section σ_{EQE} is the nanophotonic equivalent to the standard external quantum efficiency (EQE) for a macroscopic solar cell, but takes into account the effective area over which photons are absorbed. This area is determined by multiplying the absorption width σ_{abs}^{1D} (see Section 4.3.10) by the internal quantum efficiency (IQE) integrated over the nanowire length (see Fig. 4.2(d)). The shading displays the uncertainty, which is largely due to determination of the focused beam waist. (b) Based on σ_{EQE} we estimate the different contributions to the open-circuit voltage. The thermodynamic limit is V_{oc}^{rad} = 1.16 V, which is reduced by 210 mV due to the PLQY (non-radiative recombination in the semiconductor) to V_{oc}^{imp} = 950 mV, and further reduced by 100 mV due to losses at the contacts, to a final V_{oc} = 850 mV.

see Fig. 4.4(a)), which is 1.13 V.[154] The difference arises due to suppressed absorption near the band gap, which thus leads to reduced emission and a lower radiative recombination current.[155] It is important to note that such a voltage enhancement due to suppressed absorption necessarily comes at a cost in current, and can therefore not lead to efficiencies above the Shockley-Queisser limit in macroscopic devices.

Integrating the EQE over the AM1.5 solar spectrum is a common procedure used in macroscopic solar cells to verify the I_{sc} from solar simulator measurements. Here we find that an analogous procedure using σ_{EQE} instead of EQE gives a calculated short-circuit current of 320 pA, which is 29% lower than the value measured under the solar simulator (450 pA). We attribute the difference to light trapping in the glass substrate, which leads to an overestimation of the actual photocurrent of nanowire photovoltaic devices when measured on glass substrates with a solar simulator. This is supported by the fact that covering almost the entire sample, including the nanowire, with opaque foil still results in a short-circuit current of ~100 pA (22% of total, see Section 4.3.3). This suggests that just as with macroscopic solar cells, I_{sc} measurements under the solar simulator require proper masking to avoid artifacts. We therefore used the I_{sc} value based on σ_{EQE} for the calculation of V_{oc}^{rad} (see Section 4.3.11).

In conclusion, the detailed integrating sphere microscopy measurements and analysis allow us to place single nanowire solar cell performance on an absolute

thermodynamic scale, pinpoint loss mechanisms, and direct our efforts to make future nanowire solar cells that can beat record planar cell efficiencies. In terms of photocarrier collection, these nanowires are already close to the limit, reaching IQE values >90% in both polarizations for a 3.4 micron segment of the nanowire. In a vertical nanowire geometry, with the n-type segment facing the sun, this is enough to absorb all incident light and collect the generated carriers. Regarding the photo-voltage, we determined three different values for the V_{oc} that can help us pinpoint remaining loss mechanisms (Fig. 4.4(b)): (1) the thermodynamic limit calculated from wavelength-dependent σ_{EQE} measurements (1.16 V), which only includes radiative recombination; (2) the material limit extracted from local PLQY measurements (950 mV), that includes non-radiative recombination in the nanowire; and (3) the device limit extracted from solar cell operation (850 mV), that also includes losses at the contacts. The 210 mV (18%) loss related to non-radiative recombination in the nanowire could be reduced by lowering the surface recombination velocity (surface passivation) or material defect density (purification).

Improvements in contact selectivity alone could lead to a 100 mV (12%) increase in the V_{oc} compared to our record single nanowire results. Combining both makes >1V for InP nanowire solar cells far above world record planar InP solar cell perfor-mance certainly within reach.

4.3 Supplemental information

4.3.1 Sample fabrication

Nanowires are grown in a low-pressure Aixtron 200/4 Metal-Organic Vapor Phase Epitaxy (MOVPE) reactor, with the Selective Area MOVPE growth method. A 50 nm thick silicon nitride layer is used as Selective Area growth mask, patterned by the Soft Contact Nanoimprint Lithography technique on a (111)A oriented p-doped InP substrate (Zn doping carrier concentration 2×10^{18} cm^{-3} from AXT, USA).[156, 157] Hydrogen (H_2) is used as a carrier gas for precursors, with a total flow of 15 L/min. Growth is performed at 730 °C with a pressure of 100 mbar, using trimethylindium (TMI) and phosphine (PH_3) as precursors with molar fractions x_i (TMI) = 4.7×10^{-5} and x_i (PH3) = 3.9×10^{-3}, resulting in a V/III ratio of 83. The total growth time is 11 minutes with a doping profile p^{++} / p / i / n / n^{--}, with respective segment growth times of 0.5 min / 3 min / 4 min / 3 min / 0.5 min (1 μm / 3 μm / 4 μm / 3 μm / 1 μm). We use diethylzinc (DEZn) as p-dopant, with molar fractions 1.3×10^{-5} in the p^{++} region and 6.4×10^{-6} in the p region. Ditertbutylsilane (DTBSi) is used as n-dopant, with molar fractions 9.5×10^{-6} and 4.9×10^{-7} for n^{--} and n regions, respectively. After the growth, the wires were coated with a conformal 50 nm thick SiO$_2$ shell by plasma enhanced chemical vapor deposition, performed with silane and nitrous oxide as precursors at 300 °C. The nanowire measured in this Chapter had a total diameter of 410 nm (310 nm diameter InP), a length of 12 μm (9.8 μm between the contacts) and SiO$_2$ shell thickness of 50 nm.

4.3.2 Macroscopic electrode pads and contacting

Au electrodes with alignment markers were fabricated on plasma cleaned glass substrates by UV lithography and metal evaporation (see Fig. 4.5). The nanowires are transferred from the arrays ($\sim$200$\times$200 μm^2) via a pipette in ethanol and are randomly dropcast on the substrates. Electron beam lithography and metal evaporation are used to contact the single nanowires to the Au electrodes. It was found that the exact placement of the contact position on the highly doped end-segments of the nanowires is a crucial step to allow good Ohmic contact and prevent extraction barriers. Then, the glass substrates are wire-bonded to glass holders, which have prefabricated metal contact lines (also by UV lithography and metal evaporation). The bottom of the glass holder is connected to a printed-circuit-board socket which also connects to a flat electrical cable extending outside of the integrating sphere (see Fig. 4.1(c)). The metals used to contact the single nanowires were Ti (200 nm) and Au (30 nm) for the electron contact (on the n^{--} doped part) and Cr ($\sim$3 nm), Zn (15 nm), Au (215 nm) for the hole contact (on the p^{++}-doped part). Before the metal was evaporated, the exposed and developed substrates were etched in buffered HF (1:7, HF (49%): NH$_4$F (40%)) for 10 s to remove the protective SiO$_2$ shell ($\sim$50 nm) and the native oxide of the InP under the contact. The latter is known to cause Fermi level pinning under the conduction band, which easily creates ex-
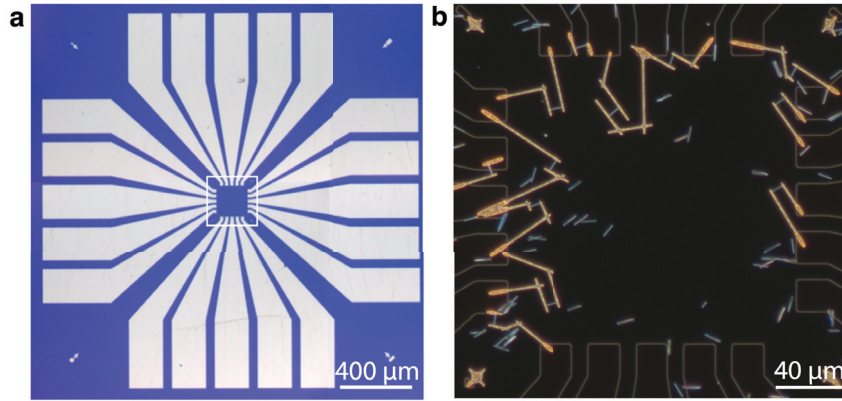
Figure 4.5: Electrode pads. (a) Bright-field microscope image of clean substrate
with Au electrodes. The square in the center marks the region depicted in (b). (b)
Dark-field microscope image showing the center of the substrate after nanowires
(white) have been dropcast and contacted (gold).

traction barriers for the hole-contact.[158] The etched samples were transferred
right away into the evaporation chamber to minimize the regrowth of the native
oxide as much as possible. It is common to use an additional annealing step at
high temperatures to diffuse Zn into the p-type InP nanowire and create a highly p-
doped layer.[137] We found this treatment to be damaging to our nanowires (strong
decrease in photoluminescence efficiency) and therefore omitted this step, as the
in situ doping of our nanowires allowed the formation of Ohmic contacts even
without annealing. Nevertheless, we chose to evaporate Zn for the hole contact
to prevent diffusion of Zn from the nanowire into the contact metal at elevated
temperatures during the evaporation and lift-off steps. For the electron contact,
Ti and Au were evaporated with an electron beam evaporator at a pressure of $(5-10) \times 10^{-7}$ mbar at an evaporation rate of 0.3-2 Å/s and acceleration voltage of 10
keV. For the hole contact Cr, Zn and Au were evaporated with a thermal evaporator
at $\sim 2 \times 10^{-6}$ mbar at a rate of 0.2-1.5 Å/s.

4.3.3 Solar simulator measurements and influence of masking

The I-V trace of the nanowire device is measured with a solar simulator (Oriel
SOL2 94062A (6X6) Class ABA, Newport) with the AM1.5G spectrum at 1 sun
(100 mW/cm^2) illumination intensity at a temperature of ~50 °C. The lamp
intensity of the solar simulator is adjusted with a silicon reference cell. Electrical
probes are used to contact the contact pads on the glass substrate with a source-
measure unit (Agilent B2910). The voltage is scanned with a positive and negative
scan rate between -1V and 1V in 2001 steps while the current is being measured.

Masking of glass substrates

Fig. 4.6(a) shows a top-down view on the electrode glass substrate under the so-lar simulator. The connected nanowire (red, not to scale) is placed in the center and black, fully opaque foil covers a large part of the substrate. Even though the nanowire is fully covered the solar simulator measurement results in a short-circuit current of $I_{sc} \sim 100$ pA ($\pm$ 5 pA).We note, that this amounts approximately to the difference between the short-circuit current determined with the solar simulator (450 pA) and the one determined with the integrating sphere setup (320 pA).

Fig. 4.6(b) shows as a schematic the side view on the setup configuration. The light is scattered into the glass substrate at the glass and Au electrode edges and trapped inside the thin glass slab. As a result the nanowire is not only illuminated from the top, but also partly from the bottom, and hence results in an inaccurate measurement. Given the common usage of glass substrates for single optoelec-tronic nanoscale device measurements, we stress the importance of using appro-priate setups or masking conditions to avoid measurement errors. The 28% higher intensity in the solar simulator measurement may lead to an overestimation of the V_{oc} under 1 sun of up to 8 mV. However, given that the V_{oc} seems limited by contact selectivity, it is not clear by how much exactly it would decrease.
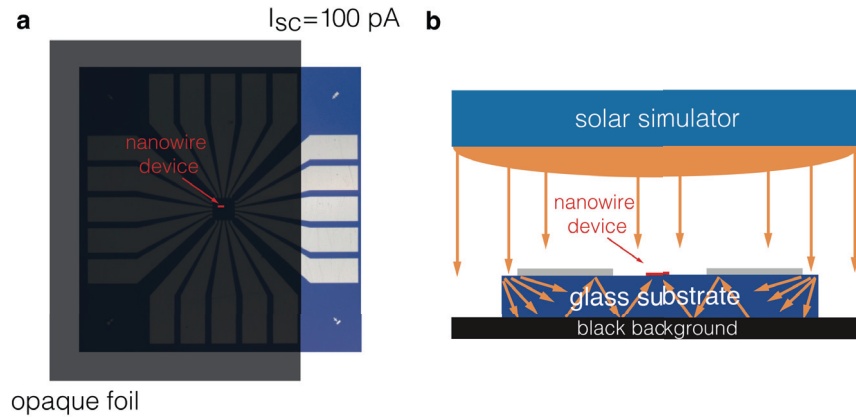
Figure 4.6: Schematic of masking conditions under solar simulator. (a) Schematic of top-down view on electrode glass substrate under solar simulator. The connected nanowire (red, not to scale) is placed in the center and black opaque foil covers a large part of the substrate. Even though the nanowire is fully covered the solar simulator measurement results in a short-circuit current of $I_{sc} = 100$ pA. (b) Schematic of side view, showing the solar simulator and the glass substrate with the single nanowire device. The light is scattered into the glass substrate at the glass and Au electrode edges and trapped inside the thin glass slab. As a result the nanowire is not only illuminated from the top, but also partly from the bottom, which results in inaccurate measurements.

4.3.4 Nanowire device statistics

Table 4.1 shows the statistics of four different nanowire batches, that were grown with a different pitch (p) and doping profile (d). Due to the small number of measured devices the statistical interpretation becomes limited for batch $p2 - d1$. However, it can clearly be seen that not only the maximum V_{oc} = 850 mV and I_{sc} = 609 pA, but also the highest means can be found in that batch. The second and third highest V_{oc}'s in that batch were 820 mV and 800 mV, respectively. Even though the doping profile of batch $p2 - d1$ (described above) was the same as for batch $p1 - d1$ the results show a clear difference in performance. To understand the influence of a different nanowire pitch (density) on the growth conditions, more studies are needed. The low yield of batch $p2 - d1$ can be mainly ascribed to the lower density of nanowires. However, during the contacting process several additional steps are potentially lowering the yield of the devices. Transferring the wires from the array can lead to cleavage of the wires from the substrate in a detrimental way. If the wire breaks not at the bottom, directly above the substrate, the broken end-facet does not correspond to the highly p-type doped part of the wire, that easily facilitates Ohmic contacts. Furthermore, prior to the contacting the orientation of the nanowire doping profile is not known. And finally, even a slight misalignment during the electron beam lithography will lead to metal contacts that are placed onto the lower doped regions of the wire (or are missing the nanowire altogether). In all those cases, the placement of the contacts on a region with a wrong doping type and density will lead to a strong extraction barrier in the final devices. In summary, great care has to be taken to yield any meaningful number of single nanowire devices, even for arrays with a large density of wires, while low densities almost certainly translate into low numbers of single nanowire devices.

$Batch$	$\bar{I}_{sc}$	$\sigma_{I_{sc}}$	I_{sc}^{max}	$\bar{V}_{oc}$	$\sigma_{V_{oc}}$	V_{oc}^{max}	♯
$p1 - d1$	54	22	90	228	117	512	18
$p1 - d2$	61	20	93	285	49	350	8
$p1 - d3$	210	83	398	329	146	640	22
$p2 - d1$	321	175	609	696	105	850	12

Table 4.1: Nanowire device statistics. Statistics of single nanowire devices from different growth batches (I_{sc} in pA and V_{oc} in mV). The nanowires were grown under different growth conditions (array pitch (p) and doping profile (d)). The device shown in this chapter comes from batch $p2 - d1$. While the statistical interpretation of the results is limited due to the small number of total devices for that batch (low density of nanowires), not only the maximum open-circuit voltages and short-circuit currents but also the highest means can be found in that batch. The second and third highest open-circuit voltages from that batch were 800 mV, and 760 mV, respectively.

4.3.5 Electron beam-induced current

The electron beam-induced current (EBIC) measurements are conducted with a beam current of 100 pA and 5 kV acceleration voltage. The integration time per pixel is 10 μs. The position of the electron beam is synchronized with the read-out of the current signal which allows the superposition of the extracted current signal with the SEM image. From the profile of the EBIC intensity along the length of the nanowire we extract an electron diffusion length of in the p-doped part of the wire (Fig. 4.7). As can be clearly seen, only the part next to the electron contact (at 0.5 - 4 μm) is active. By fitting an exponential decay curve to the tail between 4 - 6 μm, a diffusion length of the p-doped part of the wire can be extracted.
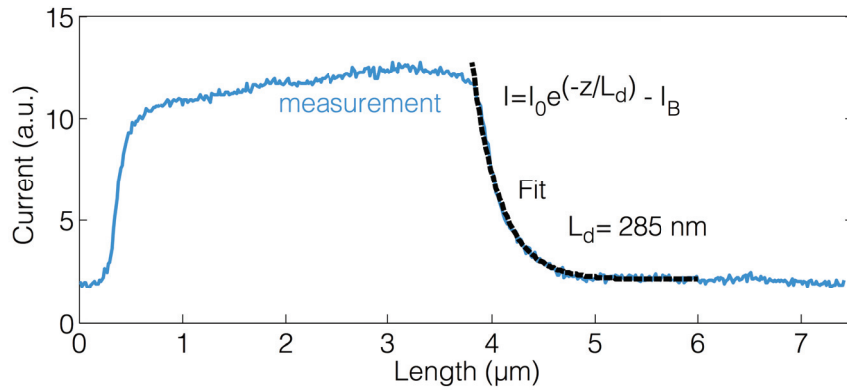
Figure 4.7: EBIC profile. Electron beam-induced current (EBIC) profile along the length of the wire, oriented as shown in Fig. 4.2(d).

4.3.6 Integrating sphere microscopy

We use a supercontinuum laser (Fianium WL-SC-400-4), sent through an acousto-optical tunable filter (AOTF, Crystal Technologies, ~5 nm bandwidth). The long working distance objective required for illuminating the nanowires is a Mitutoyo M Apo Plan NIR 50x NA 0.42 objective with a 17 mm working distance. The integrating sphere is a custom modification to a GPS-020-SL integrating sphere built by LabSphere, modified to accommodate the objective lens. We use low-noise Newport 818-UV calibrated photodiodes, each connected to Stanford Research Systems SR830 lock-in amplifiers. The transmission of the acousto-optic tunable filter was digitally modulated with a 50 percent duty cycle as a source for the lock-in amplifiers. The sample was mounted on a 3D piezoelectric stage (Piezojena Tritor400), which itself was mounted on a Newport mechanical stage for rough alignment. The incident intensity was controlled with ND filters (Thorlabs) and the AOTF RF power. The integrating sphere microscopy setup is shown schematically in Fig. 4.8.
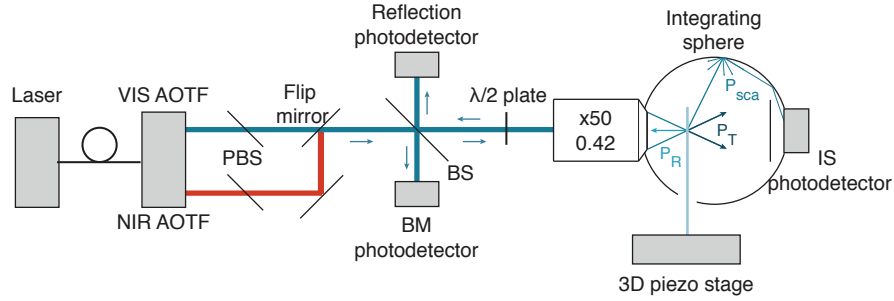
Figure 4.8: Optical setup. A supercontinuum laser (Fianium) is fiber coupled into an acousto-optical tunable filter, which has a visibile output for wavelengths 400-750 nm and a near IR output for wavelengths 700-1100 nm. We use polarizing beam splitters to ensure proper polarization, after which the light is sent through a 50:50 beam splitter to a beam monitor photodetector to measure incident power and towards the integrating sphere. The light going towards the integrating sphere passes through a half-wave plate to control the polarization. The objective focuses the light on the sample inside the integrating sphere, and collects reflected light that goes towards the reflection photodetector. Light inside the integrating sphere is monitored by the integrating sphere photodetector. The sample is moved by a 3D piezo stage (Piezojena Tritor400). The incident intensity was controlled with neutral-density (ND) filters (Thorlabs, not shown in the schematic) and the AOTF RF power.

The general measurement procedure for an absorption measurement is to prepare a sample on a glass substrate (it is crucial that the substrate is non-absorbing). The integrating sphere is positioned on a stage allowing it to be moved up and lowered to accommodate sample loading. The sample itself is positioned on a piezo stage directly underneath the integrating sphere, which in turn is positioned on a mechanical stage. The sample is inserted through a narrow slit in the bottom of the sphere, to minimize exposed open aperture area in the integrating sphere. The photodetector is positioned behind a baffle to prevent direct illumination of the detector, as can be seen in Fig. 4.1(c). The absorptance of a nanostructure is then determined using the simple formula:

$$A = 1 - \frac{R_s}{R_r} - \frac{IS_s}{IS_r} - 0.04 \tag{4.2}$$

where A is the absorptance, R_s and IS_s are the measured reflection and integrating sphere signals respectively on the sample, and R_r and IS_r are reference measurements to account for detection sensitivity. For the reflection monitor this is done by placing a mirror (Thorlabs PF10-03-P01) in the focal plane of the objective, while for the integrating sphere reference measurement the focused beam is a miss of the sample.

Because the samples are on regular microscopy glass slides the reflection from the second interface goes back into the objective, but due to the second interface being out of focus it is not collimated and hence is not detected. As a result 4%

is missing from the power balance, which is accounted for in Eq. 4.2. We have implicitly assumed here that this reflection loss is constant, but in reality it slightly decreases or increases with the amount of forward scattered and transmitted light. Hence, it is a small source of error. For example, if 20% of the incident beam is absorbed by a non-scattering particle, this will lead to a reduction of this reflection loss to 3.2%. Thus, by subtracting a constant offset, a small error in the absorptance is introduced.
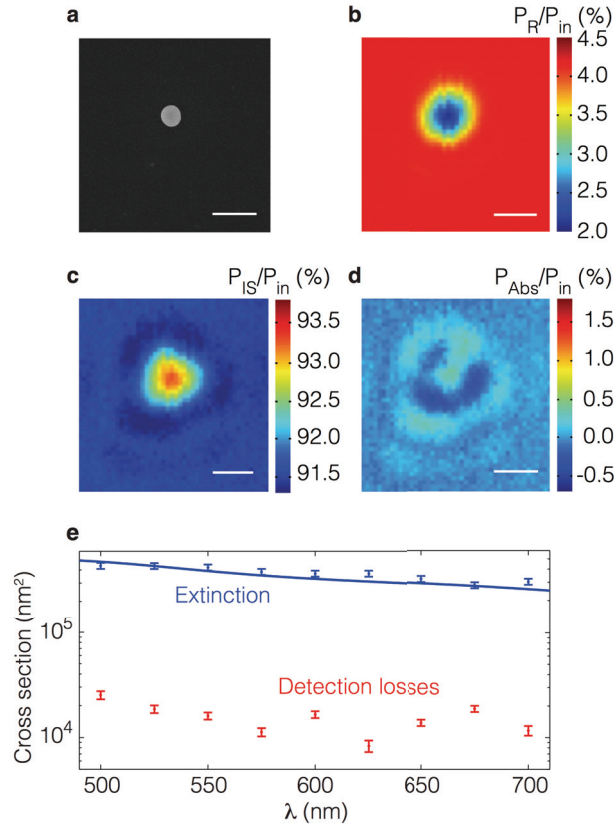
Figure 4.9: Scattering of silica nanosphere. (a) SEM image of a silica nanosphere with a diameter of 460 nm. (b, c) Reflection and integrating sphere signal of the same nanosphere at 600 nm wavelength. (d) Maps in (b) and (c) combined to give the absorptance map, showing that only a small fraction of the scattered power is not detected. The scale bar in (a)-(d) is 1 micrometer. (e) The extinction cross section of the nanosphere (blue dots) together with the Mie theory cross section (blue line). Red dots show the measured detection losses, indicating that 95.2 ± 1.2 % of the scattered light is detected. Errors are due to variance in the measurement and uncertainty in the cross section conversion.

To verify that with integrating sphere microscopy we can indeed measure absorptance accurately, we measured the "absorptance" on silica (SiO_2) nanobeads (Fig. 4.9). Although they do not absorb, they scatter strongly, providing us with a means to determine the collection efficiency of scattered light. Fig. 4.9(a) shows an

SEM image of the silica nanosphere with a diameter of 460 nm and reflection and integrating sphere detector maps of the same nanosphere at 600 nm wavelength. (Fig. 4.9(b) and 4.9(c)) The 2% decrease in reflection is matched by an analogous increase in the integrating sphere signal, but as shown in Fig. 4.9(d) a small difference remains when reflection and integrating sphere signals are combined. The maximum of this detection loss is shown as an effective detection loss cross section for a range of wavelengths in Fig. 4.9(e). This figure also shows the scattering cross section measured on the same nanosphere (blue points, see methods) and the theoretical cross section from Mie theory for a 460 nm silica sphere in vacuum (blue line).
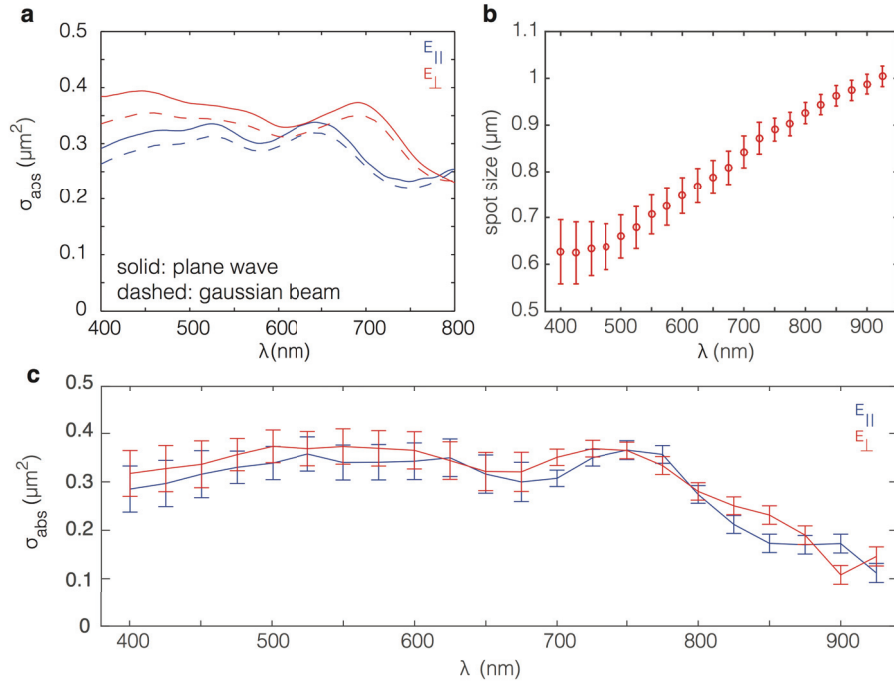
Figure 4.10: Absorption cross section. (a) The absorption cross section of a zincblende InP nanowire (300 nm diameter with 50 nm SiO_2 shell) as a function of wavelength for both polarizations of light calculated with FDTD (Lumerical), compared to the converted absorption cross section from a Gaussian beam simulation (also FDTD) using Eq. 4.8. in Section 4.3.10. There is about a 5% difference between the two. (b) The experimental spot size as determined with a knife-edge measurement. (c) The wurtzite InP nanowire absorption cross section converted from the absorptance measurement using Eq. 4.8. The magnitude of the absorption cross section shows good quantitative agreement with the simulated absorption cross section for zincblende InP, but since the crystal structure is different a direct comparison is not possible. Additionally, the absorption cross section does not appear to vanish near the band gap, which is most likely due to parasitic absorption from scattered light: as absorption in nanowires decreases, scattering increases strongly.

The extinction measurements on the silica beads were performed in the typical extinction measurement setup, with a Nikon T Plan EPI SLWD 50X 0.4 NA objective as the collection objective. The extinction cross section is then retrieved using $\Delta T/T = C_{ext}/\pi w_0^2$, where T is the transmitted power and w_0 is the beam waist. Based on the ratio of detection loss to extinction for the nanosphere we estimate that 95±1.2% of the scattered power is collected.

Although the assumption is made that the wire is infinitely thin, agreement between this approximation and full-wave simulations is good: Fig. 4.10(a) shows a direct comparison between the absorption cross section of a zincblende InP nanowire (300 nm diameter, 50 nm SiO_2 shell) from a plane wave simulation and a Gaussian beam simulation using Eq. 4.8, performed with Lumerical FDTD. The Gaussian beam underestimates the real absorption cross section by about 5%. However, experimentally we did not observe a dependence of the absorption cross section on the spot size, which we checked by underfilling our objective until the spot size was increased by 60%.

The experimental spot size as determined with knife-edge measurements on the gold contact pads is shown in Fig. 4.10(b), where the error bars depict the Gaussian fitting confidence interval (66% confidence). This spot size can be used to convert the absorptance measurements on the InP nanowire to an absorption cross section, as shown in Fig. 4.10(c). Although a direct comparison with theory is not possible, because the refractive index of wurtzite InP is not known, the magnitude of the absorption cross section is in quantitative agreement with the cross section for the zincblende InP nanowire in Fig. 4.10(a). The absorption cross section does not appear to vanish near the band gap, which is most likely due to parasitic absorption from scattered light: as absorption in nanowires decreases, scattering increases strongly. This may also explain why the IQE decreases near the band gap. For measurements on the nanowire solar cell we use very low powers (<< 1 nW) to achieve intensities close to 1 sun. We therefore swapped the photodetectors for integrating sphere and reflection measurements from the PDA100A detectors to the Newport 818 series, which have a much lower noise-equivalent power. The nanowire solar cell is connected to an SR830 lock-in amplifier as well, and incident power is modulated with 195 Hz, below the cut-off frequency of the nanowire device. Calibration of the incident power is done by placing one of the calibrated Newport 818-UV photodiodes in front of the objective.

4.3.7 Photoluminescence measurements

An integrating sphere is also commonly used to measure photoluminescence quantum yield (PLQY) quantitatively, either by connecting a spectrometer to the integrating sphere or by using a combination of long- and shortpass filters. To measure the PLQY on the nanowire we use a longpass filter in front of the integrating sphere detector (Thorlabs FELH0750). The PLQY at low intensities is not high enough to require a shortpass filter for accurate absorption measurement. The photoluminescence collection efficiency of the integrating sphere was
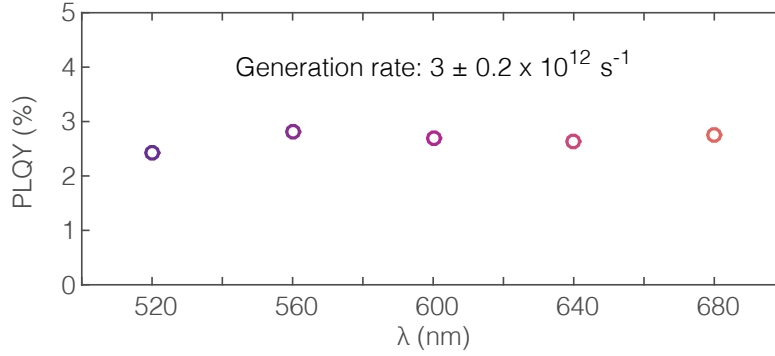
Figure 4.11: Photoluminescence excitation spectroscopy. The PLQY is shown as a
function of the excitation wavelength ranging from 520 to 680 nm for a nanowire
from the same batch as the nanowire under investigation. The PLQY does not
depend significantly on excitation wavelength.

determined by sending monochromatic light over the wavelength range of
photoluminescence into the integrating sphere, but missing the sample. The
total photoluminescence detection efficiency η_{PL} (Coulombs/emitted photon)
can then be calculated using:

$$\eta_{PL} = \frac{\int S(\lambda)\eta(\lambda)d\lambda}{\int S(\lambda)d\lambda} \tag{4.3}$$

Here $S(\lambda)$ is the PL spectrum (shown in the inset in Fig. 4.3(b)), and η is the
wavelength dependent collection efficiency of the integrating sphere (also in
Coulombs/photon). The PLQY is then calculated as the number of emitted
photons divided by the number of absorbed photons.

The error bars shown in the figures indicate the standard deviation, which
largely arises due to noise in the photodetector measurements that is insensitive
to incident laser power. For the cross sections in Fig. 4.4(a) the error bar is actually
dominated by the fitting of the spot size measurement, which can be improved.

4.3.8 Wavelengths independent PLQY

In the main text in Fig. 4.3 we have determined the photoluminescence quan-
tum yield (PLQY) with an excitation wavelength of 600 nm. Here we verify that
the PLQY is wavelength independent, which is expected for semiconductors in the
linear regime (where one photon creates one electron-hole pair). The result of the
excitation spectroscopy is shown in Fig. 4.11, where the PLQY is shown for a range
of excitation wavelengths. While the luminescence rate will depend on wavelength
due to variation in the absorption cross section, this dependence is removed by
correcting for the absorptance and calculating the PLQY. The generation rate is
almost 6 times higher than the highest rate shown in Fig. 4.3 and as a result the
PLQY is also higher.

4.3.9   Slope of the PLQY

In Fig. 4.3(b) we show the slope of the PLQY versus the generation rate, which has a linear slope. This slope can be explained by examining the ABC model for the semiconductor carrier density:

$$G = AN + p_{esc}BN^2 + CN^3 \tag{4.4}$$

Here N is the carrier density (assuming that holes and electrons have the same density, such that we are in the high injection regime), G is the generation rate of carriers, A is Shockley-Read-Hall coefficient, B is the radiative recombination coefficient, and C is the Auger coefficient. p_{esc} is the probability that a photon from a radiative recombination event actually escapes the semiconductor structure and is emitted, instead of reabsorbed. The PLQY can then be written as:

$$PLQY = \frac{p_{esc}BN^2}{AN + p_{esc}BN^2 + CN^3} \tag{4.5}$$

If Shockley-Read-Hall recombination dominates the rate equation simplifies to $G = AN$, indicating that the carrier density now increases linearly with the generation rate. Inserting this into the expression of the PLQY, we find that:

$$PLQY \approx \frac{p_{esc}BN^2}{AN} = \frac{p_{esc}B}{A}N \tag{4.6}$$

Hence the slope of the PLQY is linear with the generation rate.

4.3.10   Determining the collection cross section

For a horizontal single nanowire device we can simplify Eq. 4.1 due to the symmetry along the nanowire length. As a result of this symmetry, the absorption cross section (which is an area, 2D) is typically expressed in absorption cross section per unit length of the nanowire, such that an effective absorption width (1D) is obtained. The total absorption cross section is then effectively obtained by multiplying by the length of the wire. Since we are interested in the collection cross section, the relevant length of the wire is given by the active length shown in Fig. 4.2(d), which leads to the integral in Eq. 4.1:

$$\sigma_{EQE}(\lambda, \Omega) = \int IQE(\lambda, z)\sigma_{abs}^{1D}(\lambda, \Omega)dz \tag{4.7}$$

where σ_{abs}^{1D} is the absorption width of the nanowire (indicated by the superscript 1D). The effective absorption width σ_{abs}^{1D} can be retrieved from the absorptance measurement using a simple formula:

$$\sigma_{abs}^{1D}(\lambda) = Aw_0\sqrt{\pi/2} \tag{4.8}$$

Here A is the absorptance and w_0 is the beam waist (defined formally in the next paragraph). This formula can be found by considering the Gaussian intensity distribution of the focused spot:

$$I(x,z) = I_G e^{-2(\frac{x^2}{w_0^2} + \frac{z^2}{w_0^2})} = \frac{2P_{in}}{w_0^2} e^{-2(\frac{x^2}{w_0^2} + \frac{z^2}{w_0^2})} \tag{4.9}$$

where I_G is the Gaussian peak intensity and P_{in} is the total power carried by the beam. The beam waist w_0 is defined as the radius at which the intensity is I_G/e^2. When the wire is subject to inhomogeneous illumination, as with a Gaussian spot, the total absorbed power is found by integrating the intensity along the nanowire, where we assume that we can ignore the intensity gradient over the width of the nanowire (i.e. the wire is a line):

$$P_{abs} = \int \sigma_{abs}^{1D} I(x=0,z) dz \tag{4.10}$$

where for simplicity we assume that the wire is aligned along the z-axis. Combining Eq. 4.9 and 4.10 we find Eq. 4.8, where $A = P_{abs}/P_{in}$. This formula has been applied before to carbon nanotubes[144]. Although the assumption is made that the wire is infinitely thin, agreement between this approximation and full-wave simulations is good (see below).

Experimentally we did not observe a dependence of the absorption cross section on the spot size, which we checked by underfilling our objective until the spot size was increased by 60%.

It is important to note that σ_{EQE} can also be determined directly from the beam waist, the incident photon flux, and the laser-induced photocurrent: $\sigma_{EQE}(\lambda) = w_0\sqrt{\pi/2}\int (I_L(z)/S_{in})dz$, where I_L is the laser-induced photocurrent, S_{in} is the total incident photon flux, and the integral again is over the nanowire length. With this approach σ_{EQE} can be determined with any laser beam-induced current (LBIC) setup. Additionally, the experimental error will be smaller since both I_L and S_{in} can be determined accurately. For that reason we have determined σ_{EQE} in Fig. 4.4 following this approach.

4.3.11   Collection cross section for current calculations

The highest possible open-circuit voltage is obtained for the lowest possible recombination current I_0^{rad}, which is normally calculated by integrating the EQE over the black-body spectrum. Hence, for a nanostructure we obtain:

$$I_0^{rad} = \int^{4\pi} \int_{300}^{925} \sigma_{EQE}^{unpol}(\lambda)\, \Omega(T,\lambda)\, cos(\theta) d\lambda d\Omega \tag{4.11}$$

Here the integration over the black-body photon flux density $\Omega(T,\lambda)$ (where T is the temperature, 300K) is over all angles (taking into account a factor n^2 for the higher density of states when integrating over the glass hemisphere), and the $cos(\theta)$

is the Lambertian factor. Because thermal radiation is unpolarized, we use the average σ_{EQE} over both polarizations. We assume that between 300 and 400 nm the absorption cross section stays constant, which is a good approximation given the weakly varying nature of σ_{EQE} at shorter wavelengths. Additionally, the fraction of the photon flux in the solar spectrum contained below 400 nm is very small. Assuming that the nanowire absorbs light isotropically, we find a minimum recombination current of $I_0^{rad} = 3.1 \times 10^{-17} pA$, resulting in an open-circuit voltage of V_{oc}^{rad}=1.16V in the radiative limit. To validate the negligable effect of our isotropic absorption cross section assumption, we used Lumerical FDTD to investigate the angle dependent absorption cross section. Because the refractive index of wurtzite InP is not known, we investigated two comparable materials, zincblende InP and GaAs (both also have direct band gap in the same energy range), with the same diameter and coating thickness as the nanowire we investigated. We determined the absorption cross section averaged over both polarizations (σ_{abs}^{unpol}) in a series of single wavelength 2D simulations, using a total-field scattered-field source and perfectly matched layers (PML) as boundary conditions. The results are shown in Fig. 4.12(a) for zincblende InP and in Fig. 4.12(b) for GaAs. These figures show a polar plot of the absorption cross section weighted by the black body spectrum, $\sigma_{abs,w}^{unpol}(\theta)$ where the angle θ of the incident wave vector lies in the plane perpendicular to the nanowire axis:

$$\sigma_{abs,w}^{unpol}(\theta) = \int_{300}^{\lambda_{BG}} \sigma_{abs}^{unpol}(\lambda,\theta)\Theta(T,\lambda)d\lambda \qquad (4.12)$$

The dashed lines show the isotropic $\sigma_{abs,w}^{unpol}(\theta = 0)$ (where the absorption cross section is equal to the absorption cross section under normal incidence for all angles), while the solid lines show the actual $\sigma_{abs,w}^{unpol}(\theta)$. To assess the difference between the isotropic assumption and the actual angle dependence, we calculate the relative difference in recombination rate:

$$\Delta R = \frac{\int_0^{\pi} \sigma_{abs,w}^{unpol}(\theta)n^2(\theta)d\theta}{\sigma_{abs,w}^{unpol}(\theta = 0)\int_0^{\pi} n^2(\theta)d\theta} \qquad (4.13)$$

Here $n^2(\theta)$ is the squared refractive index of the medium (glass or air) to account for the different intensity of black body radiation. Evaluating this factor for zincblende InP and GaAs we find that they are $\Delta R = 0.91$ and $\Delta R = 0.96$ respectively. Interestingly, while the angular distribution of $\sigma_{abs,w}^{unpol}$ is modified by the presence of the glass (in particular near the critical angle, where a peak is visible that is also observed for dipole emission near an interface [159]), the integrated $\sigma_{abs,w}^{unpol}$ does not change significantly. In the other plane of incidence (parallel to the nanowire axis) we observe similar behavior, and $\sigma_{EQE}^{unpol}(\lambda,\theta)$ can therefore be approximated as isotropic. The I_{sc} can also be calculated using Eq. 4.11, but $\Theta(T,\lambda)$ has to be replaced by the AM1.5 spectrum and the integral is not carried out over all angles, but just over normal incidence (or the angle subtended by the sun).
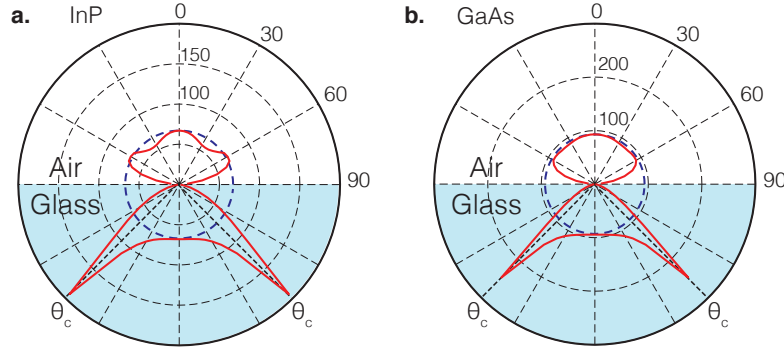
Figure 4.12: Absorption cross section versus angle of incidence. Absorption cross section in nm of a zincblende InP nanowire (a) and GaAs nanowire (b) (300 nm diameter with 50 nm SiO$_2$ shell), averaged over both polarizations and wavelengths, weighted by the blackbody spectrum. The strong lobes in the absorption cross section when incident from the glass side coincide with the critical angle in the glass, which is also observed for dipole emission near an interface [159]. These simulations were performed using Lumerical FDTD.

## 4.3.12 Series resistance and diode ideality factor

Based on a fitting method described in ref. [78] we have determined the diode ideality factor and the series resistance (see Fig. 4.13). The shunt resistance was too high to be able to determine accurately. The ideality factor ($n = 2.08$) and series resistance ($R_s = 0.12 \times 10^9 \Omega$) both reduce the fill factor from its highest possible value, $FF_{max} = 0.895$. The series resistance can possibly be reduced by improving contact resistivity and reducing the length of the intrinsic part of the nanowire.
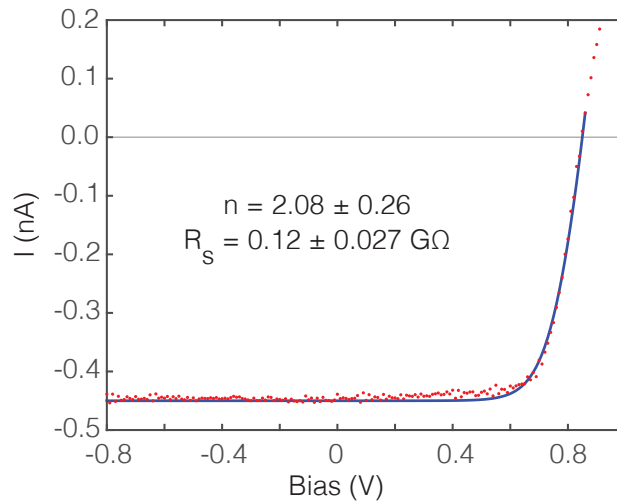
Figure 4.13: Determining the series resistance from the IV curve. By fitting the IV curve we determined the series resistance and diode ideality factor, both of which contribute to the fill factor FF=0.76 being below the maximum FF=0.895. The uncertainty in fitted values gives the 95% confidence interval.

4.3.13 Transmission electron microscopy analysis of the wurtzite InP nanowires

Fig. 4.14 shows transmission electron microscopy (TEM) images taken of nanowires grown with the same method as the nanowire under investigation in this chapter. As mentioned in Section 4.3.1, these nanowires are grown with the selective area metal-organic vapor phase epitaxy (SAMOVPE) method. The nanowires under investigation in Fig. 4.14 are slightly thinner than the nanowire, to facilitate TEM imaging. However, we do not expect the diameter to affect the crystalline structure, as they also appear identical in SEM images. The nanowires have wurtzite crystalline structure, and only at the end segment where very high n-doping is used, do we observe stacking faults. The side facets of the wires have oxidized, resulting in a 1-2 nm thick In_2O_3 layer.
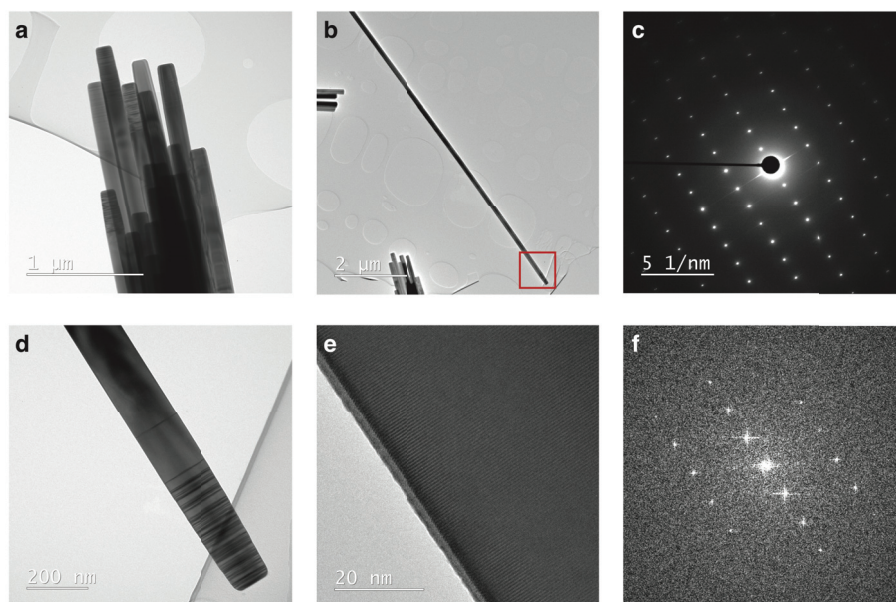
Figure 4.14: Transmission electron microscopy analysis of wurtzite InP nanowires. (a) Overview bright-field TEM image, displaying a group of nanowires, all having a mixed phase top segment of < 0.5 μm. (b) Overview image of a representative nanowire. (c) Selected area electron diffraction (SAED) pattern, acquired from a 1.3 micron long part of the stem, displaying the wurtzite crystal structure. (d) Bright-field TEM image of the top of the wire (boxed area in (b)), displaying a defected top part and a defect-free stem. (e) High resolution TEM image of the stem, again displaying the perfect wurtzite structure. The side facets of the wires have oxidized, resulting in a 1-2 nm thick In_2O_3 layer. (f) The Fourier transform corresponding to (e), highlighting the high and long-range crystallinity of these nanowires.

References

[1] A. E. Becquerel. Recherches sur les effets de la radiation chimique de la lumiere solaire au moyen des courants electriques. *Comptes Rendus de L'Academie des Sciences*, 9:145–149, 1839.

[2] Sara Thompson. http://www.triplepundit.com/2015/08/germany-became-solar-superpower, accessed 2016-05-13, 2015.

[3] Jana Kasperkevic. https://www.theguardian.com/business/2016/jan/12/us-solar-industry-employees-grows-oil-gas, accessed 2016-05-13, 2016.

[4] Giles Parkinson. http://cleantechnica.com/2015/01/14/deutsche-bank-predicts-solar-grid-parity-80-global-market-2017, accessed 2016-05-13, 2015.

[5] Mike Munsell. http://www.greentechmedia.com/articles/read/solar-accounted-for-64-of-new-electric-generating-capacity-in-the-us-in-q1, accessed 2016-06-08, 2016.

[6] UCSUSA. Coal Power: Air Pollution, 2011.

[7] Eric Martinot. Report, Renewables 2015 Global Status. Technical report, 2015.

[8] World Economic Forum. The Future of Electricity in Fast-Growing Economies Attracting Investment to Provide Affordable, Accessible and Sustainable Power. Technical Report January, 2016.

[9] Armin Richter, Martin Hermle, and Stefan W. Glunz. Reassessment of the Limiting Efficiency for Crystalline Silicon Solar Cells. *IEEE Journal of Photovoltaics*, 3(4):1184–1191, 2013.

[10] NEDO. http://www.nedo.go.jp/english/news/AA5en_100109.html, accessed 2016-09-16, 2016.

[11] Alan C. Goodrich, Douglas M. Powell, Ted L. James, Michael Woodhouse, and Tonio Buonassisi. Assessing the drivers of regional trends in solar photovoltaic manufacturing. *Energy & Environmental Science*, 6(10):2811, 2013.

[12] Donald Chung, Carolyn Davidson, Ran Fu, Kristen Ardani, Robert Margolis, Donald Chung, Carolyn Davidson, Ran Fu, Kristen Ardani, and Robert Margolis. U.S. Photovoltaic Prices and Cost Breakdowns : Q1 2015 Benchmarks for Residential, Commercial, and Utility-Scale Systems, NREL. Technical Report September, 2015.

[13] Dick van Dam. *Nanowire photonics for photovoltaics*. PhD thesis, TU Eindhoven, 2016.

[14] Ingvar Aberg, Giuliano Vescovi, Damir Asoli, Umear Naseem, James P Gilboy, Christian Sundvall, Andreas Dahlgren, K. Erik Svensson, Nicklas Anttu, Mikael T. Bjork, and Lars Samuelson. A GaAs Nanowire Array Solar Cell With 15.3% Efficiency at 1 Sun. *IEEE Journal of Photovoltaics*, 6(1):185–190, 2016.

[15] R.S. Ohl. Light-Sensitive Electric Device, Patent no US2402662, 1941.

[16] Varun Sivaram and Shayle Kann. Solar power needs a more ambitious cost target. *Nature Energy*, 1(4):16036, 2016.

[17] Albert Polman, Mark Knight, Erik C. Garnett, Bruno Ehrler, and Wim C. Sinke. Photovoltaic materials: Present efficiencies and future challenges. *Science*, 352(6283):aad4424–aad4424, 2016.

[18] Wolfgang Guter, Jan Schone, Simon P. Philipps, Marc Steiner, Gerald Siefer, Alexander Wekkeli, Elke Welser, Eduard Oliva, Andreas W. Bett, and Frank Dimroth. Current-matched triple-junction solar cell reaching 41.1% conversion efficiency under concentrated sunlight. *Applied Physics Letters*, 94(22):223504, 2009.

[19] P. Wuerfel. *Physics of Solar Cells*. Wiley-VCH Verlag GmbH, Weinheim, Germany, 2 edition, 2009.

[20] Sander A. Mann, Richard R. Grote, Richard M. Osgood, Andrea Alù, and Erik C. Garnett. Opportunities and Limitations for Nanophotonic Structures To Exceed the Shockley-Queisser Limit. *ACS Nano*, AOP, 2016.

[21] Nicklas Anttu. Shockley-Queisser Detailed Balance Efficiency Limit for Nanowire Solar Cells. *ACS Photonics*, 2(3):446–453, 2015.

[22] Erik C. Garnett, Mark L. Brongersma, Yi Cui, and Michael D. McGehee. Nanowire Solar Cells. *Annual Review of Materials Research*, 41(1):269–295, 2011.

[23] Jesper Wallentin, Nicklas Anttu, Damir Asoli, Maria Huffman, Ingvar Aberg, Martin H. Magnusson, Gerald Siefer, Peter Fuss-Kailuweit, Frank Dimroth, Bernd Witzigmann, H. Q. Xu, Lars Samuelson, Knut Deppert, and M. T. Borgstrom. InP Nanowire Array Solar Cells Achieving 13.8% Efficiency by Exceeding the Ray Optics Limit. *Science*, 339(6123):1057–1060, 2013.

[24] Daniel E. Perea, Eric R. Hemesath, Edwin J. Schwalbach, Jessica L. Lensch-Falk, Peter W. Voorhees, and Lincoln J. Lauhon. Direct measurement of dopant distribution in an individual vapour-liquid-solid nanowire. *Nature Nanotechnology*, 4(5):315–319, 2009.

[25] Erik C. Garnett, Yu-Chih Tseng, Devesh R. Khanal, Junqiao Wu, Jeffrey Bokor, and Peidong Yang. Dopant profiling and surface analysis of silicon nanowires using capacitance-voltage measurements. *Nature Nanotechnology*, 4(5):311–314, 2009.

[26] Xingtian Yin, Corsin Battaglia, Yongjing Lin, Kevin Chen, Mark Hettick, Maxwell Zheng, Cheng-Ying Chen, Daisuke Kiriya, and Ali Javey. 19.2% Efficient InP Heterojunction Solar Cell with Electron-Selective TiO 2 Contact. *ACS Photonics*, 1(12):1245–1250, 2014.

[27] Corsin Battaglia, Xingtian Yin, Maxwell Zheng, Ian D. Sharp, Teresa Chen, Stephen McDonnell, Angelica Azcatl, Carlo Carraro, Biwu Ma, Roya Maboudian, Robert M Wallace, and Ali Javey. Hole Selective MoOx Contact for Silicon Solar Cells. *Nano Letters*, 14(2):967–971, 2014.

[28] James Bullock, Mark Hettick, Jonas Geissbühler, Alison J. Ong, Thomas Allen, Carolin M. Sutter-Fella, Teresa Chen, Hiroki Ota, Ethan W. Schaler, Stefaan De Wolf, Christophe Ballif, Andrés Cuevas, and Ali Javey. Efficient silicon solar cells with dopant-free asymmetric heterocontacts. *Nature Energy*, 1(3):15031, 2016.

[29] B. K. Meyer, A. Polity, D. Reppin, M. Becker, P. Hering, P. J. Klar, Th. Sander, C. Reindl, J. Benz, M. Eickhoff, C. Heiliger, M. Heinemann, J. Bläsing, A. Krost, S. Shokovets, C. Müller, and C. Ronning. Binary copper oxide semiconductors: From materials towards devices. *Physica Status Solidi (b)*, 249(8):1487–1509, 2012.

[30] B.P. Rai. Cu_2O solar cells: A review. *Solar Cells*, 25(3):265–272, 1988.

[31] M. Green. Limits on the Open-Circuit Voltage and Efficiency of Silicon Solar Cells

Imposed by Auger Processes. *IEEE Transactions on Electron Devices*, 31(5):671, 1984.

[32] F. Meillaud, A. Shah, C. Droz, E. Vallat-Sauvain, and C. Miazza. Efficiency limits for single-junction and tandem solar cells. *Solar Energy Materials and Solar Cells*, 90(18-19):2952–2959, 2006.

[33] Frank Dimroth, Matthias Grave, Paul Beutel, Ulrich Fiedeler, Christian Karcher, Thomas N. D. Tibbits, Eduard Oliva, Gerald Siefer, Michael Schachtner, Alexander Wekkeli, Andreas W Bett, Rainer Krause, Matteo Piccin, Nicolas Blanc, Charlotte Drazek, Eric Guiot, Bruno Ghyselen, Thierry Salvetat, Aurélie Tauzin, Thomas Signamarcheix, Anja Dobrich, Thomas Hannappel, and Klaus Schwarzburg. Wafer bonded four-junction GaInP/GaAs//GaInAsP/GaInAs concentrator solar cells with 44.7% efficiency. *Progress in Photovoltaics: Research and Applications*, 22(3):277–282, 2014.

[34] Zach M. Beiley and Michael D. McGehee. Modeling low cost hybrid tandem photovoltaics with the potential for efficiencies exceeding 20%. *Energy & Environmental Science*, 5(11):9173, 2012.

[35] Sang Woon Lee, Yun Seog Lee, Jaeyeong Heo, Sin Cheng Siah, Danny Chua, Riley E. Brandt, Sang Bok Kim, Jonathan P. Mailoa, Tonio Buonassisi, and Roy G. Gordon. Improved Cu_2O-Based Solar Cells Using Atomic Layer Deposition to Control the Cu Oxidation State at the p-n Junction. *Advanced Energy Materials*, 4(11):1301916, 2014.

[36] Tadatsugu Minami, Yuki Nishi, and Toshihiro Miyata. High-Efficiency Cu_2O-Based Heterojunction Solar Cells Fabricated Using a Ga_2O_3 Thin Film as N-Type Layer. *Applied Physics Express*, 6:10–13, 2013.

[37] Yun Seog Lee, Jaeyeong Heo, Sin Cheng Siah, Jonathan P. Mailoa, Riley E. Brandt, Sang Bok Kim, Roy G. Gordon, and Tonio Buonassisi. Ultrathin amorphous zinc-tin-oxide buffer layer for enhancing heterojunction interface quality in metal-oxide solar cells. *Energy & Environmental Science*, 6(7):2112, 2013.

[38] Yun Seog Lee, Danny Chua, Riley E. Brandt, Sin Cheng Siah, Jian V. Li, Jonathan P. Mailoa, Sang Woon Lee, Roy G. Gordon, and Tonio Buonassisi. Atomic Layer Deposited Gallium Oxide Buffer Layer Enables 1.2 V Open-Circuit Voltage in Cuprous Oxide Solar Cells. *Advanced Materials*, 26(27):4704–4710, 2014.

[39] Takeo Oku, Tetsuya Yamada, Kazuya Fujimoto, and Tsuyoshi Akiyama. Microstructures and Photovoltaic Properties of Zn(Al)O/Cu_2O-Based Solar Cells Prepared by Spin-Coating and Electrodeposition. *Coatings*, 4(2):203–213, 2014.

[40] Cheng-Chiang Chen, Lung-Chien Chen, and Yi-Hsuan Lee. Fabrication and Optoelectrical Properties of IZO/Cu_2O Heterostructure Solar Cells by Thermal Oxidation. *Advances in Condensed Matter Physics*, 2012:1–5, 2012.

[41] Andrew T. Marin, David Muñoz-Rojas, Diana C. Iza, Talia Gershon, Kevin P. Musselman, and Judith L. MacManus-Driscoll. Novel Atmospheric Growth Technique to Improve Both Light Absorption and Charge Collection in ZnO/Cu_2O Thin Film Solar Cells. *Advanced Functional Materials*, 23(27):3413–3419, 2013.

[42] Talia S. Gershon, Ajaya K. Sigdel, Andrew T. Marin, Maikel F.A.M. van Hest, David S. Ginley, Richard H. Friend, Judith L. MacManus-Driscoll, and Joseph J. Berry. Improved fill factors in solution-processed ZnO/Cu_2O photovoltaics. *Thin Solid Films*, 536:280–285, 2013.

[43] Tadatsugu Minami, Yuki Nishi, Toshihiro Miyata, and Jun-ichi Nomoto. High-Efficiency Oxide Solar Cells with ZnO/Cu_2O Heterojunction Fabricated on Thermally Oxidized Cu_2O Sheets. *Applied Physics Express*, 4(6):062301, 2011.

[44] Zhiyong Fan, Haleh Razavi, Jae-won Do, Aimee Moriwaki, Onur Ergen, Yu-Lun Chueh,

Paul W. Leu, Johnny C. Ho, Toshitake Takahashi, Lothar A. Reichertz, Steven Neale, Kyoungsik Yu, Ming Wu, Joel W. Ager, and Ali Javey. Three-dimensional nanopillar-array photovoltaics on low-cost and flexible substrates. *Nature Materials*, 8(8):648–653, 2009.

[45] Matt Law, Lori E Greene, Justin C Johnson, Richard Saykally, and Peidong Yang. Nanowire dye-sensitized solar cells. *Nature Materials*, 4(6):455–459, 2005.

[46] Bozhi Tian, Xiaolin Zheng, Thomas J. Kempa, Ying Fang, Nanfang Yu, Guihua Yu, Jinlin Huang, and Charles M. Lieber. Coaxial silicon nanowires as solar cells and nanoelectronic power sources. *Nature*, 449(7164):885–9, 2007.

[47] J.M. Spurgeon, H.A. Atwater, and N.S. Lewis. A Comparison Between the Behavior of Nanorod Array and Planar Cd(Se, Te) Photoelectrodes. *Journal of Physical Chemistry C*, 112(15):6186–6193, 2008.

[48] Peter Krogstrup, Henrik Ingerslev Jørgensen, Martin Heiss, Olivier Demichel, Jeppe V. Holm, Martin Aagesen, Jesper Nygard, and Anna Fontcuberta i Morral. Single-nanowire solar cells beyond the Shockley-Queisser limit. *Nature Photonics*, 7(4):306–310, 2013.

[49] Linyou Cao, Justin S. White, Joon-Shik Park, Jon A. Schuller, Bruce M. Clemens, and Mark L. Brongersma. Engineering light absorption in semiconductor nanowire devices. *Nature Materials*, 8(8):643–647, 2009.

[50] Sander A. Mann and Erik C. Garnett. Extreme Light Absorption in Thin Semiconductor Films Wrapped around Metal Nanowires. *Nano Letters*, 13(7):3173–3178, 2013.

[51] Syed Mubeen, Joun Lee, Nirala Singh, Stephan Krämer, Galen D Stucky, and Martin Moskovits. An autonomous photosynthetic device in which all charge carriers derive from surface plasmons. *Nature Nanotechnology*, 8(4):247–251, 2013.

[52] F. Pelayo García de Arquer, Agustín Mihi, Dominik Kufer, and Gerasimos Konstantatos. Photoelectric Energy Conversion of Plasmon-Generated Hot Carriers in Metal-Insulator-Semiconductor Structures. *ACS Nano*, 7(4):3581–3588, 2013.

[53] Yoshiaki Nishijima, Kosei Ueno, Yukie Yokota, Kei Murakoshi, and Hiroaki Misawa. Plasmon-Assisted Photocurrent Generation from Visible to Near-Infrared Wavelength Using a Au-Nanorods/TiO2 Electrode. *The Journal of Physical Chemistry Letters*, 1(13):2031–2036, 2010.

[54] Yukina Takahashi and Tetsu Tatsuma. Solid state photovoltaic cells based on localized surface plasmon-induced charge separation. *Applied Physics Letters*, 99(18):182110, 2011.

[55] Young Keun Lee, Chan Ho Jung, Jonghyurk Park, Hyungtak Seo, Gabor A Somorjai, and Jeong Young Park. Surface Plasmon-Driven Hot Electron Flow Probed with Metal-Semiconductor Nanodiodes. *Nano Letters*, 11(10):4251–4255, 2011.

[56] Philipp Reineck, George P Lee, Delia Brick, Matthias Karg, Paul Mulvaney, and Udo Bach. A Solid-State Plasmonic Solar Cell via Metal Nanoparticle Self-Assembly. *Advanced Materials*, 24(35):4750–4755, 2012.

[57] Syed Mubeen, Joun Lee, Woo-Ram Lee, Nirala Singh, Galen D Stucky, and Martin Moskovits. On the Plasmonic Photovoltaic. *ACS Nano*, 8(6):6066–6073, 2014.

[58] Beniamino Sciacca, Sander A. Mann, Frans D. Tichelaar, Henny W. Zandbergen, Marijn A. van Huis, and Erik C. Garnett. Solution-Phase Epitaxial Growth of Quasi-Monocrystalline Cuprous Oxide on Metal Nanowires. *Nano Letters*, 14(10):5891–5898, 2014.

[59] Benjamin Wiley, Yugang Sun, and Younan Xia. Synthesis of Silver Nanostructures with Controlled Shapes and Properties. *Accounts of Chemical Research*, 40(10):1067–1076,

2007.

[60] Chun-Hong Kuo, Tzu-En Hua, and Michael H Huang. Au nanocrystal-directed growth of Au-Cu$_2$O core-shell heterostructures with precise morphological control. *Journal of the American Chemical Society*, 131(49):17871–8, 2009.

[61] Salih Hacialioglu, Fei Meng, and Song Jin. Facile and mild solution synthesis of Cu$_2$O nanowires and nanotubes driven by screw dislocations. *Chemical Communications*, 48(8):1174–6, 2012.

[62] Sarah Brittman, Youngdong Yoo, Neil P. Dasgupta, Si-In Kim, Bongsoo Kim, and Peidong Yang. Epitaxially Aligned Cuprous Oxide Nanowires for All-Oxide, Single-Wire Solar Cells. *Nano Letters*, 14(8):4665–4670, 2014.

[63] Joon I. Jang. *Cuprous Oxide (Cu$_2$O): A Unique System Hosting Various Excitonic Matter and Exhibiting Large Third-Order Nonlinear Optical Responses*. Number 1991. InTech, Rijeka, 2011.

[64] E. E. Huber. The effect of mercury contamination on the work function of gold. *Applied Physics Letters*, 8(7):169, 1966.

[65] O. Madelung, U. Roessler, and M. Schulz, editors. *Cuprous oxide (Cu$_2$O) crystal structure, lattice parameters*. Springer Berlin Heidelberg, 1998.

[66] M. B. Brodsky. Metallic Interfaces and Property Modification. *J. Phys. Colloques*, 45:C5–349–356, 1984.

[67] Jung-Dae Kwon, Se-Hun Kwon, Tae-Hoon Jung, Kee-Seok Nam, Kwun-Bum Chung, Dong-Ho Kim, and Jin-Seong Park. Controlled growth and properties of p-type cuprous oxide films by plasma-enhanced atomic layer deposition at low temperature. *Applied Surface Science*, 285:373–379, 2013.

[68] David R. Linde, editor. *CRC Handbook of Chemistry and Physics*. New York, 85 edition, 2005.

[69] K. P. Musselman, Y. Ievskaya, and J. L. MacManus-Driscoll. Modelling charge transport lengths in heterojunction solar cells. *Applied Physics Letters*, 101(25):253503, 2012.

[70] Yingchi Liu, Hubert K. Turley, John R. Tumbleston, Edward T. Samulski, and Rene Lopez. Minority carrier transport length of electrodeposited Cu$_2$O in ZnO/Cu$_2$O heterojunction solar cells. *Applied Physics Letters*, 98(16):162105, 2011.

[71] Jiangtian Li, Scott K. Cushing, Peng Zheng, Fanke Meng, Deryn Chu, and Nianqiang Wu. Plasmon-induced photonic and energy-transfer enhancement of solar water splitting by a hematite nanorod array. *Nature Communications*, 4, 2013.

[72] Pengyu Fan, Zongfu Yu, Shanhui Fan, and Mark L. Brongersma. Optical Fano resonance of an individual semiconductor nanostructure. *Nature Materials*, 13(5):471–475, 2014.

[73] Pengyu Fan, Kevin C Y Huang, Linyou Cao, and Mark L. Brongersma. Redesigning Photodetector Electrodes as an Optical Antenna. *Nano Letters*, 13(2):392–396, 2013.

[74] Pengyu Fan, Uday K. Chettiar, Linyou Cao, Farzaneh Afshinmanesh, Nader Engheta, and Mark L. Brongersma. An invisible metal-semiconductor photodetector. *Nature Photonics*, 6(6):380–385, 2012.

[75] Sarah Brittman, Hanwei Gao, Erik C. Garnett, and Peidong Yang. Absorption of Light in a Single-Nanowire Silicon Solar Cell Decorated with an Octahedral Silver Nanocrystal. 11(12):5189–5195, 2011.

[76] Ferid Chaffar Akkari and Mounir Kanzari. Optical, structural, and electrical properties of Cu$_2$O thin films. *Physica Status Solidi (a)*, 207(7):1647–1651, 2010.

[77] A. Wagenpfahl, D. Rauh, M. Binder, C. Deibel, and V. Dyakonov. S-shaped current-voltage characteristics of organic solar devices. *Physical Review B*, 82(11):115306, 2010.

[78] Minlu Zhang, Hui Wang, and C. W. Tang. Hole-transport limited S-shaped I-V curves in planar heterojunction organic photovoltaic cells. *Applied Physics Letters*, 99(21):213506, 2011.

[79] Rebecca Saive, Christian Mueller, Janusz Schinke, Robert Lovrincic, and Wolfgang Kowalsky. Understanding S-shaped current-voltage characteristics of organic solar cells: Direct measurement of potential distributions by scanning Kelvin probe. *Applied Physics Letters*, 103(24):243303, 2013.

[80] Ankit Kumar, Srinivas Sista, and Yang Yang. Dipole induced anomalous S-shape I-V curves in polymer solar cells. *Journal of Applied Physics*, 105(9):094512, 2009.

[81] L. C. Olsen, R. C. Bohara, and M. W. Urie. Explanation for low-efficiency Cu_2O Schottky-barrier solar cells. *Applied Physics Letters*, 34(1):47, 1979.

[82] Seungchan Ryu, Jun Hong Noh, Nam Joong Jeon, Young Chan Kim, Woon Seok Yang, Jangwon Seo, and Sang Il Seok. Voltage output of efficient perovskite solar cells with high open-circuit voltage and fill factor. *Energy & Environmental Science*, 3:2614–2618, 2014.

[83] Alexander W. Hains, Jun Liu, Alex B. F. Martinson, Michael D. Irwin, and Tobin J. Marks. Anode Interfacial Tuning via Electron-Blocking/Hole-Transport Layers and Indium Tin Oxide Surface Treatment in Bulk-Heterojunction Organic Photovoltaic Cells. *Advanced Functional Materials*, 20(4):595–606, 2010.

[84] S. M. Sze and K. K. Ng. *Physics of Semiconductor Devices*. Wiley, New Jersey, 3rd edition, 2007.

[85] R B Godfrey and M A Green. 655 mV open-circuit voltage, 17.6% efficient silicon MIS solar cells. *Appl!ied Physics Letters*, 34(June):790–793, 1979.

[86] Rudolf Hezel. Recent Progress in MIS Solar Cells. *Progress in Photovoltaics: Research and Applications*, 5:109–120, 1997.

[87] M A Green, F D King, and J Shewchun. Minority Carrier MIS Tunnel Diodes and Their Application to Electron - 1. Theory. *Solid-State Electronics*, 17:551–561, 1974.

[88] J Shewchun, M A Green, and F D King. Minority Carrier MIS Tunnel Diodes and Their Application to Electron- and photovoltaic energy conversion - 2. Experiment. *Solid-State Electronics*, 17:563–572, 1974.

[89] F Feldmann, Martin Bivour, Christian Reichel, Martin Hermle, and Stefan W Glunz. A passivated rear contact for high-efficiency n-Type silicon solar cells enabling high Vocs and FF>82%. *28th European Photovoltaic Solar Energy Conference and Exhibition*, pages 988–992, 2013.

[90] F. Feldmann, M. Simon, M. Bivour, C. Reichel, M. Hermle, and S. W. Glunz. Carrier-selective contacts for Si solar cells. *Applied Physics Letters*, 104(18):181105, 2014.

[91] S W Glunz, F Feldmann, A Richter, M Bivour, C Reichel, H Steinkemper, J Benick, and M Hermle. The irresistible charm of a simple current flow pattern- 25% with a solar cell featuring a full-area back contact. *31st European Photovoltaic Solar Energy Conference and Exhibition*, (September), 2015.

[92] Andrew G. Scheuermann, John P. Lawrence, Kyle W. Kemp, T. Ito, Adrian Walsh, Christopher E. D. Chidsey, Paul K. Hurley, and Paul C. McIntyre. Design principles for maximizing photovoltage in metal-oxide-protected water-splitting photoanodes. *Nature Materials*, 15:1–8, 2015.

[93] Yi Wei Chen, Jonathan D Prange, Simon Dühnen, Yohan Park, Marika Gunji, Christopher E D Chidsey, and Paul C McIntyre. Atomic layer-deposited tunnel oxide stabilizes silicon photoanodes for water oxidation. *Nature Materials*, 10(7):539–544, 2011.

[94] Daniel V Esposito, Igor Levin, Thomas P Moffat, and a Alec Talin. H2 evolution at Si-based metal-insulator-semiconductor photoelectrodes enhanced by inversion channel charge collection and H spillover. *Nature Materials*, 12(6):562–568, 2013.

[95] James C. Hill, Alan T. Landers, and Jay A. Switzer. An electrodeposited inhomogeneous metal-insulator-semiconductor junction for efficient photoelectrochemical water oxidation. *Nature Materials*, 14:6751–6755, 2015.

[96] R. Hezel, R. Meyer, and A. Metz. New generation of crystalline silicon solar cells: simple processing and record efficiencies for industrial-size devices. *Solar Energy Materials and Solar Cells*, 65(1):311–316, 2001.

[97] Jorik Van De Groep, Pierpaolo Spinelli, and Albert Polman. Transparent conducting silver nanowire networks. *Nano Letters*, 12(6):3138–3144, 2012.

[98] Peter B. Catrysse and Shanhui Fan. Nanopatterned Metallic Films for Use As Transparent Conductive Electrodes in Optoelectronic Devices. *Nano Letters*, 10(8):2944–2949, 2010.

[99] Ping Kuang, Joong-Mok Park, Wai Leung, Rakesh C. Mahadevapuram, Kanwar S. Nalwa, Tae-Geun Kim, Sumit Chaudhary, Kai-Ming Ho, and Kristen Constant. A New Architecture for Transparent Electrodes: Relieving the Trade-Off Between Electrical Conductivity and Optical Transmittance. *Advanced Materials*, 23(21):2469–2473, 2011.

[100] S. De, T. M. Higgins, P. E. Lyons, E. M. Doherty, P. N. Nirmalraj, W. J. Blau, J. J. Boland, and J. N. Coleman. Silver Nanowire Networks as Flexible, Transparent, Conducting Films: Extremely High DC to Optical Conductivity Ratios. *ACS Nano*, 3(7):1767–1774, 2009.

[101] Aaron R Rathmell, Minh Nguyen, Miaofang Chi, and Benjamin J Wiley. Synthesis of Oxidation-Resistant Cupronickel Nanowires for Transparent Conducting Nanowire Networks. *Nano Letters*, 12(6):3193–3199, 2012.

[102] Tze-Bin Song, You Seung Rim, Fengmin Liu, Brion Bob, Shenglin Ye, Yao-Tsung Hsieh, and Yang Yang. Highly Robust Silver Nanowire Network for Transparent Highly Robust Silver Nanowire Network for Transparent Electrode. *ACS Applied Materials and Interfaces*, 7:24601–24607, 2015.

[103] Liqiang Yang, Tim Zhang, Huaxing Zhou, Samuel C Price, Benjamin J Wiley, and Wei You. Solution-Processed Flexible Polymer Solar Cells with Silver Nanowire Electrodes. *ACS Applied Materials & Interfaces*, 3(10):4075–4084, 2011.

[104] Whitney Gaynor, Jung-yong Lee, and Peter Peumans. Fully Solution-Processed Inverted Polymer Solar Cells with Laminated Nanowire Electrodes. *ACS Nano*, 4(1):1–5, 2010.

[105] Jung Yong Lee, Stephen T. Connor, Yi Cui, and Peter Peumans. Solution-processed metal nanowire mesh transparent electrodes. *Nano Letters*, 8(2):689–692, 2008.

[106] Jorik van de Groep, Dhritiman Gupta, Marc a. Verschuuren, Martijn M. Wienk, Rene a. J. Janssen, and Albert Polman. Large-area soft-imprinted nanowire networks as light trapping transparent conductors. *Scientific Reports*, 5:11414, 2015.

[107] S. Smit, D. Garcia-Alonso, S. Bordihn, M.S. Hanssen, and W.M.M. Kessels. Metal-oxide-based hole-selective tunneling contacts for crystalline silicon solar cells. *Solar Energy Materials and Solar Cells*, 120:376–382, 2014.

[108] G. Dingemans, R. Seguin, P. Engelhart, M. C. M. van de Sanden, and W. M. M. Kessels. Silicon surface passivation by ultrathin Al 2 O 3 films synthesized by thermal and plasma atomic layer deposition. *physica status solidi (RRL) - Rapid Research Letters*, 4(1-2):10–12, 2010.

[109] B. Hoex, J. Schmidt, M.C.M. van de Sanden, and W.M.M. Kessels. CRYSTALLINE

SILICON SURFACE PASSIVATION BY THE NEGATIVE-CHARGE- DIELECTRIC Al2O3. *33rd IEEE Photovolatic Specialists Conference*, pages 1–4, 2008.

[110] Jan Benick, Bram Hoex, M. C. M. van de Sanden, W. M. M. Kessels, Oliver Schultz, and Stefan W. Glunz. High efficiency n-type Si solar cells on Al2O3-passivated boron emitters. *Applied Physics Letters*, 92(25):253504, 2008.

[111] G Dingemans and W M M Kessels. Status and prospects of Al2O3 -based surface passivation schemes for silicon solar cells. *J. Vac. Sci. Technol. A*, 30(4):1–27, 2012.

[112] Sarah Brittman, Gede W. P. Adhyaksa, and Erik C. Garnett. The expanding world of hybrid perovskites: materials properties and emerging applications. *MRS Communications*, 5(1):1–20, 2015.

[113] Yee Chia Yeo, Tsu Jae King, and Chenming Hu. Metal-dielectric band alignment and its implications for metal gate complementary metal-oxide-semiconductor technology. *Journal of Applied Physics*, 92(12):7266–7271, 2002.

[114] J. Tersoff. Schottky Barrier Heights and the Continuum of Gap States. *Physical Review Letters*, 52(6):465–468, 1984.

[115] Stefano Prada, Umberto Martinez, and Gianfranco Pacchioni. Work function changes induced by deposition of ultrathin dielectric films on metals: A theoretical analysis. *Physical Review B*, 78(23):1–8, 2008.

[116] Corsin Battaglia, Silvia Martín de Nicolás, Stefaan De Wolf, Xingtian Yin, Maxwell Zheng, Christophe Ballif, and Ali Javey. Silicon heterojunction solar cell with passivated hole selective MoOx contact. *Applied Physics Letters*, 104(11):113902, 2014.

[117] Jonas Geissbühler, Jérémie Werner, Silvia Martin de Nicolas, Loris Barraud, Aïcha Hessler-Wyser, Matthieu Despeisse, Sylvain Nicolay, Andrea Tomasi, Bjoern Niesen, Stefan De Wolf, and Christophe Ballif. 22.5% Efficient Silicon Heterojunction Solar Cell With Molybdenum Oxide Hole Collector. *Applied Physics Letters*, 107(8):081601, 2015.

[118] Takahiro Mishima, Mikio Taguchi, Hitoshi Sakata, and Eiji Maruyama. Development status of high-efficiency HIT solar cells. *Solar Energy Materials and Solar Cells*, 95(1):18–21, 2011.

[119] H. Schade and J. Pankove. Hydrogenated Amorphous Silicon Damage. *Journal de Physique Colloques*, 42 (C4):327–330, 1981.

[120] R Singh, M A Green, and K Rajkanan. Review of conductor - insulator - semiconductor (cis) solar cells. *Solar Cells*, 3:95–148, 1981.

[121] Zachary C Holman, Antoine Descoeudres, Loris Barraud, Fernando Zicarelli Fernandez, Johannes P Seif, Stefaan De Wolf, and Christophe Ballif. Heterojunction Solar Cells. *IEEE Journal of Photovoltaics*, 2(1):7–15, 2012.

[122] Anastassios Mavrokefalos, Sang Eon Han, Selcuk Yerci, Matthew S. Branham, and Gang Chen. Efficient Light Trapping in Inverted Nanopyramid Thin Crystalline Silicon Membranes for Solar Cell Applications. *Nano Letters*, 12(6):2792–2796, 2012.

[123] Sang Eon Han and Gang Chen. Toward the lambertian limit of light trapping in thin nanostructured silicon solar cells. *Nano Letters*, 10(11):4692–4696, 2010.

[124] Kang Mook Lim, Shilpi Gupta, Chad Ropp, and Edo Waks. Development of metal etch mask by single layer lift-off for silicon nitride photonic crystals. *Microelectronic Engineering*, 88(6):994–998, 2011.

[125] S. Franssila. *Introduction to Microfabrication*. Wiley, Chichester, 2 edition, 2010.

[126] R. Varache, C. Leendertz, M. E. Gueunier-Farret, J. Haschke, D. Muñoz, and L. Korte. Investigation of Selective Junctions Using a Newly Developed Tunnel Current Model for Solar Cell Applications. *Solar Energy Materials and Solar Cells*, 141:14–23, 2015.

[127] Andres Cuevas. The Recombination Parameter J0. *Energy Procedia*, 55:53–62, 2014.

[128] Nicholas E. Singh-Miller and Nicola Marzari. Surface energies, work functions, and surface relaxations of low-index metallic surfaces from first principles. *Physical Review B*, 80(23):235407, 2009.

[129] Andres Cuevas, Thomas Allen, and James Bullock. Skin care for healthy silicon solar cells. *2015 IEEE 42nd Photovoltaic Specialist Conference (PVSC)*, (1):1–6, 2015.

[130] Priyaranga Koswatta, Mathieu Boccard, and Zachary Holman. Carrier-Selective Contacts in Silicon Solar Cells. *Photovoltaic Specialist Conference (PVSC), 2015 IEEE 42nd*, (2):1–4, 2015.

[131] Albert Polman and Harry a Atwater. Photonic design principles for ultrahigh-efficiency photovoltaics. *Nature Materials*, 11(3):174–177, 2012.

[132] Peter Krogstrup, Henrik Ingerslev Jørgensen, Martin Heiss, Olivier Demichel, Jeppe V Holm, Martin Aagesen, Jesper Nygard, and Anna Fontcuberta i Morral. Single-nanowire solar cells beyond the Shockley-Queisser limit. *Nature Photonics*, 7(4):306–310, 2013.

[133] Michael D. Kelzenberg, Daniel B. Turner-Evans, Brendan M. Kayes, Michael A. Filler, Morgan C. Putnam, Nathan S. Lewis, and Harry A. Atwater. Photovoltaic Measurements in Single-Nanowire Silicon Solar Cells. *Nano Letters*, 8(2):710–714, 2008.

[134] Jinyao Tang, Ziyang Huo, Sarah Brittman, Hanwei Gao, and Peidong Yang. Solution-processed core-shell nanowires for efficient photovoltaic cells. *Nature Nanotechnology*, 6(9):568–572, 2011.

[135] Jeppe V. Holm, Henrik I. Jørgensen, Peter Krogstrup, Jesper Nygård, Huiyun Liu, and Martin Aagesen. Surface-passivated GaAsP single-nanowire solar cells exceeding 10% efficiency grown on silicon. *Nature Communications*, 4:1498, 2013.

[136] Jonathan E. Allen, Eric R. Hemesath, Daniel E. Perea, Jessica L. Lensch-Falk, Z.Y. Li, Feng Yin, Mhairi H. Gass, Peng Wang, Andrew L. Bleloch, Richard E. Palmer, and Lincoln J. Lauhon. High-resolution detection of Au catalyst atoms in Si nanowires. *Nature Nanotechnology*, 3(3):168–173, 2008.

[137] Ali Nowzari, Magnus Heurlin, Vishal Jain, Kristian Storm, Ali Hosseinnia, Nicklas Anttu, Magnus T. Borgström, Håkan Pettersson, and Lars Samuelson. A Comparative Study of Absorption in Vertically and Laterally Oriented InP Core-Shell Nanowire Photovoltaic Devices. *Nano Letters*, 15(3):1809–1814, 2015.

[138] Mustafa Yorulmaz, Sara Nizzero, Anneli Hoggard, Lin-Yung Wang, Yi-Yu Cai, Man-Nung Su, Wei-Shun Chang, and Stephan Link. Single-Particle Absorption Spectroscopy by Photothermal Contrast. *Nano Letters*, 15(5):3041–3047, 2015.

[139] A. Gaiduk, M. Yorulmaz, P. V. Ruijgrok, and M. Orrit. Room-Temperature Detection of a Single Molecule's Absorption by Photothermal Contrast. *Science*, 330(6002):353–356, 2010.

[140] Guillaume Baffou, Pierre Bon, Julien Savatier, Julien Polleux, Min Zhu, Marine Merlin, Hervé Rigneault, and Serge Monneret. Thermal Imaging of Nanostructures by Quantitative Optical Phase Analysis. *ACS Nano*, 6(3):2452–2458, 2012.

[141] Pascal Berto, Esteban Bermúdez Ureña, Pierre Bon, Romain Quidant, Hervé Rigneault, and Guillaume Baffou. Quantitative absorption spectroscopy of nano-objects. *Physical Review B*, 86(16):165417, 2012.

[142] A. Arbouet, D. Christofilos, N. Del Fatti, F. Vallée, J. R. Huntzinger, L. Arnaud, P. Billaud, and M. Broyer. Direct measurement of the single-metal-cluster optical absorption. *Physical Review Letters*, 93(12):10–14, 2004.

[143] Otto L. Muskens, Guillaume Bachelier, Natalia Del Fatti, Fabrice Vallée, Arnaud Brioude, Xuchuan Jiang, and Marie-Paule Pileni. Quantitative Absorption Spectroscopy of a Single Gold Nanorod. *The Journal of Physical Chemistry C*, 112(24):8917–8921, 2008.

[144] Jean-Christophe Blancon, Matthieu Paillet, Huy Nam Tran, Xuan Tinh Than, Samuel Aberra Guebrou, Anthony Ayari, Alfonso San Miguel, Ngoc-Minh Phan, Ahmed-azmi Zahab, Jean-louis Sauvajol, Natalia Del Fatti, and Fabrice Vallée. Direct measurement of the absolute absorption spectrum of individual semiconducting single-wall carbon nanotubes. *Nature Communications*, 4, 2013.

[145] Martin Husnik, Stefan Linden, Richard Diehl, Jens Niegemann, Kurt Busch, and Martin Wegener. Quantitative Experimental Determination of Scattering and Absorption Cross-Section Spectra of Individual Optical Metallic Nanoantennas. *Physical Review Letters*, 109(23):233902, 2012.

[146] George F. Burkhard, Eric T. Hoke, and Michael D. McGehee. Accounting for Interference, Scattering, and Electrode Absorption to Make Accurate Internal Quantum Efficiency Measurements in Organic and Other Thin Solar Cells. *Advanced Materials*, 22(30):3293–3297, 2010.

[147] Daniel J. Gargas, Hanwei Gao, Hungta Wang, and Peidong Yang. High Quantum Efficiency of Band-Edge Emission from ZnO Nanowires. *Nano Letters*, 11(9):3792–3796, 2011.

[148] S. N. G. Chu, R. A. Logan, M. Geva, and N.T. Ha. Concentration dependent Zn diffusion in InP during metalorganic vapor phase epitaxy. *Journal of Applied Physics*, (78):3001, 1995.

[149] Marta De Luca, Attilio Zilli, H. Aruni Fonseka, Sudha Mokkapati, Antonio Miriametro, Hark Hoe Tan, Leigh Morris Smith, Chennupati Jagadish, Mario Capizzi, and Antonio Polimeni. Polarized Light Absorption in Wurtzite InP Nanowire Ensembles. *Nano Letters*, 15(2):998–1005, 2015.

[150] Uwe Rau. Reciprocity relation between photovoltaic quantum efficiency and electroluminescent emission of solar cells. *Physical Review B*, 76(8):085303, 2007.

[151] Martin A Green. Radiative efficiency of state-of-the-art photovoltaic cells. *Progress in Photovoltaics: Research and Applications*, 20(4):472–476, 2012.

[152] John K. Katahara and Hugh W. Hillhouse. Quasi-Fermi level splitting and sub-bandgap absorptivity from semiconductor photoluminescence. *Journal of Applied Physics*, 116(17):173504, 2014.

[153] C. E. Bohren and D. R. Huffman. *Absorption and Scattering of Light by Small Particles*. Wiley, New York, 1984.

[154] W. Shockley and H. J. Queisser. Detailed Balance Limit of Efficiency of p-n Junction Solar Cells. *Journal of Applied Physics*, 32(3):510–519, 1961.

[155] Sunil Sandhu, Zongfu Yu, and Shanhui Fan. Detailed Balance Analysis and Enhancement of Open-Circuit Voltage in Single-Nanowire Solar Cells. *Nano Letters*, 1015(2), 2014.

[156] Thomas Mårtensson, Patrick Carlberg, Magnus Borgström, Lars Montelius, Werner Seifert, and Lars Samuelson. Nanowire Arrays Defined by Nanoimprint Lithography. *Nano Letters*, 4(4):699–702, 2004.

[157] Aurélie Pierret, Moïra Hocevar, Silke L. Diedenhofen, Rienk E. Algra, E. Vlieg, Eugene C. Timmering, Marc A. Verschuuren, George W. G. Immink, Marcel A. Verheijen, and Erik P. A. M. Bakkers. Generic nano-imprint process for fabrication of nanowire arrays. *Nanotechnology*, 21(6):065305, 2010.

[158] M. H. M. van Weert, O. Wunnicke, A. L. Roest, T. J. Eijkemans, A. Yu Silov, J. E. M. Haverkort, G. W. 't Hooft, and E. P. A. M. Bakkers. Large redshift in photoluminescence of p-doped InP nanowires induced by Fermi-level pinning. *Applied Physics Letters*, 88(4):043109, 2006.

[159] W. Lukosz. Light emission by magnetic and electric dipoles close to a plane dielectric interface. III. Radiation patterns of dipoles with arbitrary orientation. *Journal of the Optical Society of America*, 69:1495, 1979.

[160] Fan Wang, Qian Gao, Kun Peng, Zhe Li, Ziyuan Li, Yanan Guo, Lan Fu, Leigh Morris Smith, Hark Hoe Tan, and Chennupati Jagadish. Spatially resolved doping concentration and nonradiative lifetime profiles in single Si-doped InP nanowires using photoluminescence mapping. *Nano Letters*, 15:3017–3023, 2015.

[161] Gerben L. Tuin, Magnus T. Borgström, Johanna Trägårdh, Martin Ek, L. Reine Wallenberg, Lars Samuelson, and Mats-Erik Pistol. Valence band splitting in wurtzite InP nanowires observed by photoluminescence and photoluminescence excitation spectroscopy. *Nano Research*, 4(2):159–163, 2011.

[162] Howard E. Jackson, S. Perera, K. Pemasiri, L. M. Smith, J. Yarrison-Rice, J. H. Kang, Q. Gao, H. H. Tan, C. Jagadish, Y. Guo, J. Zou, Jisoon Ihm, and Hyeonsik Cheong. Probing the valence band structure of wurtzite InP nanowires by photoluminescence excitation spectroscopy. In *AIP Conference Proceeding*, volume 1399, pages 481–482, 2011.

[163] Seokhun Yun, Young Hun Paik, Sung Jin Kim, Doo Gun Kim, Taeksoo Ji, and Jae Cheol Shin. High efficiency AZO-InP nanopillar-based heterojunction solar cells. *Current Applied Physics*, 16(7):726–730, 2016.

[164] R. Iyer, R. R. Chang, and D. L. Lile. Sulfur as a surface passivation for InP. *Applied Physics Letters*, 53(2):134–136, 1988.

[165] Shanshan Tian, Zhipeng Wei, Yongfeng Li, Haifeng Zhao, Xuan Fang, Jilong Tang, Dan Fang, Lijuan Sun, Guojun Liu, Bin Yao, and Xiaohui Ma. Surface state and optical property of sulfur passivated InP. *Materials Science in Semiconductor Processing*, 17:33–37, 2014.

[166] N Tajik, C M Haapamaki, and R R LaPierre. Photoluminescence model of sulfur passivated p-InP nanowires. *Nanotechnology*, 23(31):315703, 2012.

[167] Daniel Cuypers, Dennis H. Van Dorp, Massimo Tallarida, Simone Brizzi, Leonard Rodriguez, Thierry Conard, Sophia Arnauts, Dieter Schmeisser, Christoph Adelmann, and Stefan De Gendt. Study of InP Surfaces after Wet Chemical Treatments. *ECS Transactions*, 58(6):297–303, 2013.

[168] A.C. Ferraz and G.P. Srivastava. Atomic geometry and electronic structure of S/InP(001). *Surface Science*, 6028(96):377–380, 1997.

[169] Palani Arudra, Gregory M. Marshall, Neng Liu, and Jan J. Dubowski. Enhanced photonic stability of GaAs in aqueous electrolyte using alkanethiol self-assembled monolayers and postprocessing with ammonium sulfide. *Journal of Physical Chemistry C*, 116(4):2891–2895, 2012.

[170] Nan Guan, Xing Dai, Agnès Messanvi, Hezhi Zhang, Jianchang Yan, Eric Gautier, Catherine Bougerol, François H. Julien, Christophe Durand, Joël Eymery, and Maria Tchernycheva. Flexible White Light Emitting Diodes Based on Nitride Nanowires and Nanophosphors. *ACS Photonics*, 3(4):597–603, 2016.

[171] Xing Dai, Agnes Messanvi, Hezhi Zhang, Christophe Durand, Joël Eymery, Catherine Bougerol, François H Julien, and Maria Tchernycheva. Flexible Light-Emitting Diodes Based on Vertical Nitride Nanowires. *Nano Letters*, 15(10):6958–6964, 2015.

[172] Katherine E. Plass, Michael A. Filler, Joshua M. Spurgeon, Brendan M. Kayes, Stephen Maldonado, Bruce S. Brunschwig, Harry A. Atwater, and Nathan S. Lewis. Flexible Polymer-Embedded Si Wire Arrays. *Advanced Materials*, 21(3):325–328, 2009.

[173] Hanna Dickèr. *Nanowire Peel-Off for Tandem Solar Cell Applications*. PhD thesis, Lund University, 2016.

[174] Adele C. Tamboli, Christopher T. Chen, Emily L. Warren, Daniel B. Turner-Evans, Michael D. Kelzenberg, Nathan S. Lewis, and Harry A. Atwater. Wafer-scale growth of silicon microwire arrays for photovoltaics and solar fuel generation. *IEEE Journal of Photovoltaics*, 2(3):294–297, 2012.

[175] Michael Woodhouse, Alan Goodrich, Ted L. James, Todd Deutsch, Myles Steiner, Daniel Friedman, and Alfred Hicks. A Manufacturing Cost Analysis Relevant to Single- and Dual-Junction Photovoltaic Cells Fabricated with III-Vs and III-Vs Grown on Czochralski Silicon. Technical report.

[176] Alta Devices. http://www.altadevices.com/technology-overview, accessed 2016-08-07, 2016.

[177] Younan Xia and George M Whitesides. Soft Lithography. *Annual Review of Material Science*, 28:153–84, 1998.

[178] Marc A Verschuuren. *Substrate Conformal Imprint Lithography for Nanophotonics*. PhD thesis, 2010.

[179] Oxford-Instruments. https://www.oxford-instruments.com/products/etching-deposition-and-growth/processes/etching-processes/compound-semiconductors/inp-etching, accessed 2016-08-28, 2016.

[180] Pierre Colson, Catherine Henrist, and Rudi Cloots. Nanosphere Lithography: A Powerful Method for the Controlled Manufacturing of Nanomaterials. *Journal of Nanomaterials*, 2013:1–19, 2013.

[181] Erik C. Garnett, Mark L. Brongersma, Yi Cui, and Michael D. McGehee. Nanowire Solar Cells. *Annual Review of Materials Research*, 41(1):269–295, 2011.

[182] M. Ã. Jurisch, F. Bo, T. Bu, S. Eichler, T. Flade, U. Kretzer, A. Ko, J. Stenzenberger, and B. Weinert. LEC- and VGF-growth of SI GaAs single crystals recent developments and current issues. *Journal of Crystal Growth*, 275:283–291, 2005.

[183] Andrew J. Ritenour, Jason W. Boucher, Robert DeLancey, Ann L. Greenaway, Shaul Aloni, and Shannon W. Boettcher. Doping and electronic properties of GaAs grown by close-spaced vapor transport from powder sources for scalable III-V photovoltaics. *Energy Environ. Sci.*, 8(1):278–285, 2015.

[184] Ann L. Greenaway, Meredith C. Sharps, Jason W. Boucher, Lyndi E. Strange, Matthew G. Kast, Shaul Aloni, and Shannon W. Boettcher. Selective Area Epitaxy of GaAs Microstructures by Close-Spaced Vapor Transport for Solar Energy Conversion Applications. *ACS Energy Letters*, 1, 2016.

[185] Jason W. Boucher, Andrew J. Ritenour, Ann L. Greenaway, Shaul Aloni, and Shannon W. Boettcher. Homojunction GaAs Solar Cells Grown by Close Space Vapor Transport. *Photovoltaic Specialist Conference (PVSC), 2014 IEEE 40th*, pages 460–464, 2014.

[186] Katsuhiro Tomioka, Keitaro Ikejiri, Tomotaka Tanaka, Junichi Motohisa, Shinjiroh Hara, Kenji Hiruma, and Takashi Fukui. Selective-area growth of III-V nanowires and their applications. *Journal of Materials Research*, 26(17):2127–2141, 2011.

[187] U. Rau and J. H. Werner. Radiative efficiency limits of solar cells with lateral band-gap fluctuations. *Applied Physics Letters*, 84(19):3735, 2004.

[188] Erik Bakkers, Magnus Borgstrom, Wim van den Einden, Maarten van Weert, Ana Helman, Verheijen, and Marcel. Epitaxial III-V Nanowires on Silicon for Vertical

Devices. *ECS Trans.*, 3(2):415–423, 2006.

[189] Waferworld. Waferworld: https://www.waferworld.com/product-search/, 2016.

[190] Didier Marsan. Email correspondence with Didier Marsan, CTO of InPact. 2016.

[191] Jayasad Arumughan, Thomas Pernau, Alexander Hauser, and Ihor Melnyk. Simplified edge isolation of buried contact solar cells. *Solar Energy Materials and Solar Cells*, 87(1-4):705–714, 2005.

[192] F. H. Nicoll. The Use of Close Spacing in Chemical-Transport Systems for Growing Epitaxial Layers of Semiconductors. *Journal of the Electrochemical Society*, 110(11):1165–1167, 1963.

[193] Andrew J. Ritenour, Jason W. Boucher, Robert DeLancey, Ann L. Greenaway, Shaul Aloni, and Shannon W. Boettcher. Doping and electronic properties of GaAs grown by close-spaced vapor transport from powder sources for scalable III-V photovoltaics. *Energy Environ. Sci.*, 8(1):278–285, 2015.

[194] Rebecca Jones-Albertus, David Feldman, Ran Fu, Kelsey Horowitz, and Michael Woodhouse. Technology advances needed for photovoltaics to achieve widespread grid price parity. *Progress in Photovoltaics: Research and Applications*, 24(9):1272–1283, 2016.

[195] Bluebird-Electric. Solar Assisted Vehicles: http://www.bluebird-electric.net/blueplanet_ecostar, accessed 2016-08-25, 2016.

[196] Wikipedia. The Internet of Things, Wikipedia, accessed 2016-08-26, 2016.

[197] Bernadette Walker and Justin McLean. http://www.bloomberg.com/features/2016-ev-oil-crisis/ accessed 2016-08-16. 2016.

[198] H. P. Mahabaduge, W. L. Rance, J. M. Burst, M. O. Reese, D. M. Meysing, C. A. Wolden, J. Li, J. D. Beach, T. A. Gessert, W. K. Metzger, S. Garner, and T. M. Barnes. High-efficiency, flexible CdTe solar cells on ultra-thin glass substrates. *Applied Physics Letters*, 106(13):133501, 2015.

[199] ZSW Stuttgart. Press release. Technical report, Stuttgart, 2016.

[200] Eric Johlin, Lucas K. Wagner, Tonio Buonassisi, and Jeffrey C. Grossman. Origins of structural hole traps in hydrogenated amorphous silicon. *Physical Review Letters*, 110(14):1–5, 2013.

[201] Jesper B. Sorensen and Toby E. Stuart. Aging , Obsolescence , and Organizational Innovation. *Administrative Science Quarterly*, 45(1):81–112, 2011.

[202] Joseph Kalowekamo and Erin Baker. Estimating the manufacturing cost of purely organic solar cells. *Solar Energy*, 83(8):1224–1231, 2009.

Summary

This thesis deals with material interfaces in nanoscale photovoltaics. Interfaces between the absorbing semiconductor and the ambient, a dielectric, metal, metal oxide or another semiconductor are all of utmost importance for an efficient solar cell. While the optical properties are largely unaffected by a few nanometer thin layer, the electronic properties can change tremendously: electrical passivation of surface defects or establishing contact selectivity can turn a piece of black rock with two metal leads into a highly efficient solar cell.

When moving from macro- to nanoscale semiconductors, highly useful properties emerge compared to wafer-based or even thin-film semiconductors. Most importantly, not only directly incident but also adjacent light can be absorbed by the single nanoscale constituents. As a result, the same amount of light can be absorbed with an array of single nanoscale structures with much empty space in between, as with a continuous thin-film. This effect leads to largely reduced material consumption and, depending on the growth methods, even to a faster growth process for a fully absorbing layer. The empty space in between the nanoscale elements can be filled with a flexible glass or polymer layer, that allows to mechanically peel off the structures from their growth template. Additionally, the nanostructured semiconductor elements do not need any additional anti-reflection coating, as do wafer-based or thin-film solar cells. While those properties are enormously beneficial for photovoltaics, another feature creates a tremendous challenge: by nanostructuring semiconductors, the surface-to-volume ratio becomes much larger compared to thin-film or wafer-based solar cells. As a result, the influence of surface and interface properties on the overall performance of the nanoscale photovoltaic elements increases substantially. In this thesis, nanowires are therefore chosen as a highly sensitive platform to study the impact of those interface properties on the overall photovoltaic performance. Based on our findings we to propose device designs for more efficient practical nanowire array solar cells.

In **Chapter 2**, we study the photovoltaic performance of metal-semiconductor core-shell nanowires. This type of nanowire has theoretically been predicted to

provide outstanding optical absorption in the semiconductor shell and a short required minority carrier diffusion length, with the added benefit of direct carrier extraction via the metal core, potentially reducing the series resistance of the device as compared to core-shell geometries that only consist of semiconductor nanowires. We show, that even though the semiconductor shell grows epitaxially of the metal core, that is the interface is highly ordered, charge carrier extraction barriers and enhanced interfacial recombination can be observed.

In **Chapter 3**, we study a metal-insulator-semiconductor solar cell, that mitigates the direct and detrimental contact between a metal and a semiconductor by utilizing a thin passivating and insulating interlayer. We show highly homogenous charge carrier extraction and are able to fabricate devices with a power conversion efficiency of 11% (after correction, V_{oc} = 560 mV, J_{sc} = 33 mA/cm^2). For a metal-insulator-semiconductor solar cell, the V_{oc} depends strongly on the work function difference between the metal and the semiconductor. We argue that the presence of a charge-neutrality-level at the metal-dielectric interface is likely to lower the metal work function from its vacuum value and hence negatively impacts the measured V_{oc}. Furthermore, we introduce a novel structure, nanopyramids integrated in between the metal nanowire network, that allow to substantially reduce reflection and potentially increase the short-circuit current densities.

In **Chapter 4** we turn our focus on single InP nanowires. Those nanoscale structures have a higher optical than geometrical absorption cross section and while this property can be of great use, as outlined above, it complicates the characterization of single nanoscale devices. A priori the absorption cross section is unknown and additionally changing with wavelength, hence it is unclear how much of the incident light directly interacts with the single nanoscale device. This prevents quantification of the different conversion steps and hence loss mechanisms, but also the quantification of the absolute radiative limit V_{oc}^{rad}. For this thesis it is of great importance to quantify non-radiative recombination and non-ideal contacts. To that end, we introduce a new measurement technique, integrating sphere microscopy, to accurately quantify the remaining loss mechanisms. We measure the internal quantum efficiency (IQE), the photoluminescence quantum yield (PLQY) and the nanoscale equivalent of the EQE (external quantum efficiency) of a single record nanowire device for the first time. With those measurements we are able to quantify the impact of non-ideal contacts and non-radiative recombination and understand how much can be gained by reducing those loss mechanisms.

In **Chapter 5** we focus on the interface properties of those InP nanowires. We study the device performance of contacted and masked single nanowire devices before and after HF, MoO$_x$ and sulfur treatment. We show improved surface passivation and improved carrier selectivity for the different treatments and in particular pay attention to the effect of Fermi-level pinning on those properties. By introducing the interfacial layer MoO$_x$ to nanowire solar cells, we can increase the open-circuit voltage by up to 335 mV, from 500 mV to 835 mV.

In **Chapter 6**, we explore valorization opportunities that emerge from our insights of the preceding chapters. In the previous chapters we have shown how to

contact single p-type InP nanowires and how to increase their contact selectivity to make highly performing devices, which has been an unsolved issue in the past. Translating those insights to array solar cells allows us to propose a manufacturing line which exploits the intrinsic advantages that emerge from the nanowire geometry compared to thin-films; faster growth speeds, reduced material consumption, fast mechanical peel-off and intrinsic anti-reflection properties. We perform a techno-economic analysis on our proposed fabrication process by comparing the technology to already existing and very similar manufacturing lines for thin-film GaAs solar cells. Furthermore, we underline the highly flexibility of the process line which is not limited to one growth method, let alone semiconductor. We argue that this can have a substantial impact on the rate of innovation in a hypothetical company invested into this process.

So far nanowire solar cells are limited to efficiencies < 20%. Improvements in the past have mainly been achieved by improving the optics, that is the absorption has been enhanced due to an optimized array design (width, length, tapering and array pitch), and because of improved nanowire fabrication methods (crystal growth, etching). This thesis turns the attention towards the electronics, in particular novel selective contacts and passivation layers. With those two major contributions nanowire solar cells have the chance to finally close the gap between their practical and thermodynamic efficiency limits and to finally become a technological and economical reality.

Samenvatting

Dit proefschrift betreft grensvlakken tussen materialen in zonnecellen op nano-schaal. Grensvlakken tussen de absorberende halfgeleider en bijvoorbeeld lucht, een diëlektricum, een metaal, een metaaloxide, of een andere halfgeleider, zijn van groot belang voor efficiënte zonnecellen. Hoewel de optische eigenschappen van een zonnecel nauwelijks veranderen door een laag van een paar nanometer, kunnen de elektronische eigenschappen juist sterk beïnvloed worden. Het passiveren van oppervlaktedefecten of het creëren van selectieve contacten maakt het verschil: wat in feite een zwarte steen met metalen contacten was, verandert zo in een erg efficiënte zonnecel.

In halfgeleiders op nanoschaal zijn er zeer bruikbare optische fenomenen, die in macroscopische halfgeleiders niet voorkomen. Het meest bijzondere voorbeeld is dat nanostructuren meer licht kunnen absorberen dan dat wat ze direct raakt. Als een direct gevolg kan een periodieke structuur van nanodeeltjes, met veel lege ruimte daartussenin, evenveel licht absorberen als een continue laag. Daardoor kunnen zonnecellen gefabriceerd worden van veel minder halfgeleider, en, afhankelijk van de methode, ook sneller. De lege ruimte tussen de nanodeeltjes kan gevuld worden met een flexibele glassoort of een polymeer, waarmee de laag met nanodeeltjes van het originele substraat gepeld kan worden. Daarnaast is voor zonnecellen gebaseerd op dit soort nanodeeltjes geen extra antireflectieve laag nodig, in tegenstelling tot voor normale zonnecellen. Nanostructuren bieden dus enorme voordelen voor zonnecellen, maar er zijn ook grote uitdagingen. De verhouding van oppervlakte tot volume is met name veel groter dan in vergelijkbare zonnecellen gemaakt van dunne films of wafers, en als gevolg spelen oppervlaktes en grensvlakken dus een veel grotere rol. In dit proefschrift gebruiken wij nanodraden als een hoogst sensitief platform om de rol van oppervlaktes en grensvlakken in zonnecellen op nanoschaal te onderzoeken. Op basis van onze vondsten stellen wij ook ontwerpen voor die kunnen leiden tot nanodraadzonnecellen met hogere efficiëntie.

In **hoofdstuk 2** onderzoeken we de fotovoltaische eigenschappen van nan-odraden met een kern van metaal en een schil van halfgeleider. Het is eerder theoretisch aangetoond dat deze metaal-halfgeleider nanodraden licht zeer

sterk kunnen absorberen in een heel dunne schil van halfgeleider. Doordat de metalen kern ook als elektrode kan fungeren, is daardoor maar een hele korte diffusielengte nodig, en kan ook de serieweerstand stukken lager zijn dan in nanodraden die helemaal van halfgeleider zijn gemaakt. We laten zien dat, hoewel de halfgeleiderschil zich als een epitaxiale laag op de metalen kern, er toch extractiebarrières voor de ladingsdragers zijn. Er vindt daardoor verhoogde recombinatie plaats.

In **hoofdstuk 3** onderzoeken we een metaal-isolator-halfgeleider zonnecel, waarin het nadelige directe contact tussen het metaal en de halfgeleider vermeden wordt door een dunne isolerende en passiverende laag tussen beiden te plaatsen. Als contactgeometrie gebruiken wij een netwerk van metalen nanodraden. We demonstreren een zeer homogene extractie van ladingsdragers, en hebben een zonnecel gemaakt met een efficientie van 11%. Na correctie had deze zonnecel een $V_{oc} = 560$ mV en een $J_{sc} = 33$ mA/cm^2.

In metaal-isolator-halfgeleider zonnecellen hangt de V_{oc} sterk af van het verschil in uittreearbeid tussen het metaal en de halfgeleider. Hoewel het directe contact tussen het metaal en de halfgeleider nu vermeden is, ondervinden wij dat de V_{oc} nu negatief beïnvloed wordt door een ladingsneutraliteitsniveau. Daarnaast laten wij zijn dat ons nanodraadnetwerk gecombineerd kan worden geinverteerde pyramides tussen de contactvingers, wat leidt tot sterk gereduceerde reflectie en daarom mogelijk tot hogere stroomdichtheden.

In **hoofdstuk 4** richten we ons op individuele InP nanodraadzonnecellen. Deze nanodraden kunnen een grotere absorptiedoorsnede hebben dan hun geometrische doorsneden, zoals hierboven al genoemd. Hoewel deze eigenschap dus erg nuttig kan zijn, maakt het karakterisatie van zulke zonnecellen een stuk gecompliceerder. *A priori* is de absorptiedoorsnede onbekend en afhankelijk van de golflengte van het licht, en het is dus onduidelijk hoeveel van het inkomende licht direct reageert met de nanodraad zonnecel. Dit maakt het kwantificeren van de efficiëntie van de verschillende stappen in het conversieproces onmogelijk, en dus ook van de verliesmechanismes. Daarnaast kan de ultieme thermodynamische limiet voor het voltage, V_{oc}^{rad}, niet bepaald worden, en in deze dissertatie spelen al deze factoren juist een zeer belangrijke rol. Daartoe introduceren wij een nieuwe meettechniek, integrerende bol microscopie, waarmee we de verschillende verliesmechanismes in kaart kunnen brengen. We meten de interne kwantum efficientie en fotoluminescentie kwantum efficientie voor de eerste keer, en definiëren en bepalen een equivalent voor de externe kwantum efficientie op nanoschaal. Met behulp van deze metingen kunnen we kwantificeren wat het effect is van de contactkwaliteit en niet-stralende recombinatie, en krijgen we inzicht in hoeveel deze nanodraadzonnecel verbeterd kan worden door deze verliesmechanismes te elimineren.

In **hoofdstuk 5** onderzoeken we de grensvlakeigenschappen van deze InP nanodraden nader. We bestuderen het gedrag van deze zonnecellen voor en na behandeling met HF, MoO$_x$ en zwavel. We demonstreren verbeterde grensvlakpassivatie en ladingsdragerselectiviteit door deze verschillende behandelingen, en letten in

het bijzonder op hoe deze behandelingen het Fermi-niveau vastleggen, en hoe dat de eigenschappen van de zonnecel beinvloedt. Door een grensvlaklaag van MoO_x toe te voegen kunnen we de V_{oc} met 335 mV verhogen, van 500 mV naar 835 mV.

In **hoofdstuk 6** verkennen wij valorisatiekansen die voortkomen uit inzichten verkregen op basis van de voorgaande hoofdstukken. In die hoofdstukken hebben wij laten zien hoe elektrodes gevormd kunnen worden op individuele positief gedoteerde InP nanodraden, en hoe de selectiviteit van die elektrodes verbeterd kan worden. Dit was een onopgelost probleem, en als gevolg kunnen nu hoogefficiënte nanodraad zonnecellen gemaakt worden. Door deze nieuwe inzichten te vertalen naar periodieke roosters van nanodraadzonnecellen, kunnen we een nieuwe fabricageproces voorstellen. Dit proces benut de intrinsieke voordelen die de nanodraadgeometrie met zich meebrengt ten opzichte van dunne films: kortere depositietijden, verminderde materiaalconsumptie, snel mechanisch afpellen van de laag met nanodraden en bijna ideale antireflectie-eigenschappen. We ondernemen een techno-economische analyse van ons fabricageproces door de methode te vergelijken met bestaande en vergelijkbare technieken voor GaAs zonnecellen. We benadrukken de flexibiliteit van de methode, die niet tot een enkele depositiemethode gelimiteerd is, laat staan tot één halfgeleider. Onze voorgestelde methode kan grote invloed hebben op bedrijven in deze sector.

Tot dusver zijn efficiënties van nanodraadzonnecellen gelimiteerd tot <20%. Verbeteringen in het verleden hebben vooral te maken gehad met optica, door bijvoorbeeld verbeterde absorptie van licht, of door verbeteringen in fabricagemethoden (zoals kristallisatie en etsen). In dit proefschrift richten wij ons op de elektronische eigenschappen, met nadruk op vernieuwende selectieve elektrodes en passiverende lagen. Door deze twee belangrijke bijdragen hebben nanodraadzonnecellen de kans om het gat te dichten tussen de praktische en limiterende efficiënties, en om eindelijk een technologische en economische realiteit te worden.

List of publications

This thesis is based on the following publications:

- *Au-Cu$_2$O core-shell nanowire photovoltaics*
  S.Z. Oener, S.A. Mann, B. Sciacca, C. Sfiligoj, J. Hoang, E.C. Garnett,
  Appl. Phys. Lett. **106**, 023501 (2015). **(Chapter 2)**

- *Metal-insulator-semiconductor nanowire network solar cells*
  S.Z. Oener, J. van de Groep, B. Macco, P.C.P. Bronsveld, W.M.M. Kessels,
  A. Polman, E.C. Garnett, Nano Lett. 2016, **16**, 3689 (2016). **(Chapter 3)**

- *Quantifying losses and thermodynamic limits in nanophotonic solar cells*
  S.A. Mann,* S.Z. Oener,* A. Cavalli, J.E.M. Haverkort, E.P.A.M. Bakkers, E.C.
  Garnett, Nature Nanotech., 10.1038/nnano.2016.162, (2016) (accepted),
  *equal contribution. **(Chapter 4)**

- *Carrier selective contacts for nanowire solar cells*
  S.Z. Oener, A. Cavalli, J.E.M. Haverkort, E.P.A.M. Bakkers, E.C. Garnett, (in
  preparation). **(Chapter 5)**

- *A techno-economic case study for nanowire solar cells*
  S.Z. Oener and E.C. Garnett, (in preparation). **(Chapter 6)**

Other publications by the author:

- *Infrared birefringence imaging of residual stress and bulk defects in multicrystalline silicon*
  V. Ganapati, S. Schoenfelder, S. Castellanos, S. Oener, R. Koepge, A. Sampson,
  M.A. Marcus, B. Lai, H. Morhenn, G. Hahn, J. Bagdahn, T. Buonassisi,
  J. Appl. Phys. **108**, 063528 (2010).

Acknowledgements

First of all I would like to thank my supervisor Erik Garnett. The last four years have been an outstanding professional and personal learning experience for me. Not only did I profit and learn tremendously from your broad scientific knowledge and technical skills, but also your creative, cheerful and outgoing personality. Your ability to continuously explore new research directions and collaborations and to openly discuss research ideas and insights with the research community sets an inspiring example. By joining your group right from the first day, I had furthermore the privilege to see you grow into a successful group leader. Through this experience I have gained much knowledge about setting up a lab, managing, interviewing and teaching new group members and writing grant applications. Also, thank you for being forgiving for my sometimes direct and harsh communication!

This research was part of the LMPV program at AMOLF and as such would have not been possible without the full commitment and guidance of Albert Polman. I would like to thank you for pulling together this great center of photovoltaics research which, I am certain, will continue it's successful path. Thank you for always being such a great source of advice!

I would like to thank all the members of the Nanoscale Solar Cells group and in particular Annemarie Berkhout, Beniamino Sciacca, Cristina Sfiligoj, Eric Johlin, Forrest Bradbury, Haralds Abolins, Jenny Kontoleta, John Hoang, Marc Duursma,

About the author

Sebastian was born on the 1st of November, 1985, in Berlin, Germany. After finishing his high school degree as valedictorian and his community service in a Kindergarten, he moved to the south of the country, to the beautiful city of Konstanz. There, during his physics studies, Sebastian developed his strong interest in renewable energy technologies. This led him to join the photovoltaics community early on as a student researcher and to pursue a 6 month research internship with Prof. Dr. Tonio Buonassisi at MIT, USA. In 2012, he graduated with a 1.0 (A+) from the University of Konstanz under the supervison of Prof. Dr. Giso Hahn and Prof. Dr. Thomas Dekorsy with a thesis on defect characterization in multi-crystalline silicon solar cells.

In the same year, he joined the LMPV team, lead by Prof. Dr. Albert Polman, at AMOLF, Amsterdam. Supervised by Dr. Erik Garnett he conducted his research in the Nanoscale Solar Cells group. The results of this four year period are presented in this thesis.

After defending his thesis, Sebastian will work on sustainable long-term energy storage as a postdoctoral researcher.